

Warsaw University of Technology

Faculty of Physics

# Doctoral Thesis

M.Sc. Eng. Buğra TÜZEMEN

**Spin-polarized impurities in ultracold Fermi gas**

Supervisor:  
Prof. Piotr MAGIERSKI,  
Ph.D, D.Sc.

Warsaw 2021



*“πάντα ῥεῖ”*

Heraclitus of Ephesus



# Acknowledgements

First of all, I would like to express my sincere gratitude to my supervisor, Prof. Dr. Piotr Magierski. From him, I have not only learned physics but also how to approach problems. It is always a pleasure for me to listen to his clear and complete interpretations and always great fun to discuss physical matters. Apart from physics, one of the most important things that I learned from him is that there are no stupid questions, and it is a lesson that I will carry on. I feel lucky to be his Ph.D. student because of his teaching abilities and his patience and support.

Moreover, I would like to thank the Nuclear Theory Group in Faculty of Physics of Warsaw University of Technology. Especially to Prof. Dr. Gabriel Wlazłowski. His help with my research was indispensable. Plus, over the years, I had the chance to observe him developing a sophisticated and extensive numerical toolkit—a process which I found an example from his discipline and perseverance.

Of course, my research would have been impossible without the aid and support of my parents. Although I could not get to see them as much as I wanted to due to complicated bureaucracy and the global pandemic, knowing that they always support me in every aspect of my life has been a significant boost.

Last but not least, I appreciate all of my friends who supported me in this (initially) foreign country and sharing my adventures. The ones who make me feel like I am not a foreigner and the others who make me feel like I am not away from home never let me feel alone.

Also, I would like to acknowledge the Polish National Science Center (NCN) supporting my research under Contracts No. UMO-2016/23/B/ST2/01789.



# Abstract

M.Sc Eng. Buğra TÜZEMEN

*Spin-polarized impurities in ultracold Fermi gas*

The many-body physics has witnessed continuous cooperation between the theory and the experiment over the ages. The immense development in the theory of the *classical* gas during the 19th century has sparked such experiments that, in return, needed further theory. In ultracold temperatures, a gas, either bosonic or fermionic, displays a macroscopic quantum coherence that shows itself as superconductivity in charged particles and as superfluidity in neutral particles. This new state of matter has been studied thoroughly, both in theory and in experiments, during the 20th century. The advancements paved the way to discover a plethora of exotic states of matter.

This study focuses on the theoretical discovery of a particular exotic configuration in spin-imbalanced ultracold Fermi gas, dubbed as *ferron*. Although the phase diagram for spin-polarized ultracold Fermi gas is incomplete, it is possible to create meta-stable excited states that harbor low polarization values. The ferron results from the modulation of the pairing field in the presence of a chemical potential difference between the spin components. This mechanism is essentially similar to the one behind the Josephson- $\pi$  junction in superconductor-ferromagnet-superconductor junctions or the Fulde-Ferrel-Larkin-Ovchinnikov phase. Therefore, the enhanced stability of the ferron and its inner structure and internal properties may shed light on this long-sought phase which has not been experimentally observed yet.

The thesis includes a brief introduction to the polarized ultracold Fermi gas and the BCS-BEC crossover with rough examples of the experimental techniques. The second chapter revisits the BCS theory of superconductivity to establish insight into the Bogoliubov-de Gennes (BdG) method, the Andreev states, and finite temperature behavior of the pairing field. In the next chapter, the technical framework in order to simulate many-body systems is presented. An extension of the density functional theory

to the superfluid systems has been described. The framework called time-dependent asymmetric superfluid local density approximation (TDASLDA) allows simulating the spin-polarized unitary Fermi gas dynamics. It has been confirmed with numerous results over the years.

The second half of the thesis is dedicated to the ferron. In the fourth chapter, the dynamic creation of the ferron is presented. The conditions to create the ferron and its remarkable stability are studied and explained. Moreover, (even more) exotic configurations of the ferron, such as deformation and concentric ferrons along with ferron collisions, are presented. The comparison between BdG and TDASLDA and between the weak and strong coupling regimes are also part of Chapter 4.

In the fifth chapter, the ferron is studied internally in static, two-dimensional systems. The behavior of the Andreev states which constitute the ferron is presented. The ferrons obtain a specific size in relation to the spin-imbalance it has. Also, it is shown they can be obtained in finite temperatures well within experimental reach if the object's size is large enough. The dynamic properties of the ferron are addressed in the sixth chapter. It has shown that each ferron is associated with a critical velocity beyond which it can not be accelerated further and eventually destroyed. This critical velocity is attributed to the size and the strength of the superfluid background. Furthermore, ferron's response to the superflow is studied in terms of its inertia. The studies show that the effective mass depends trivially on the size of the ferron. However, an extra contribution as a result of the strength of the superfluid background is also presented. The final chapter includes a summary and future aspects.

Below, the list of scientific publications on which this thesis is based is presented:

- P. Magierski, B. Tüzemen, G. Wlazłowski, "Spin-polarized droplets in the unitary fermi gas", *Phys. Rev. A* **100**, 3 (2019).
- B. Tüzemen and P. Kukliński and P. Magierski and G. Wlazłowski, "Properties of spin-polarized impurities - ferrons, in the unitary fermi gas", *Acta Physica Polonia B*, vol **51** (2020).
- P. Magierski, B. Tüzemen, G. Wlazłowski, "Dynamics of spin-polarized impurity in ultracold Fermi gas", *Phys. Rev. A* **104**, 3 (2021).

*Keywords: spin-polarized ultracold Fermi gas, FFLO phase, Andreev bound states, non-equilibrium superfluidity*

# Streszczenie

M.Sc Eng. Buğra TÜZEMEN

*Spinowo spolaryzowane domieszki w ultrazimnym gazie fermiego*

Fizyka wielu ciał była świadkiem ciągłej współpracy na przestrzeni wieków między teorią a eksperymentem. Ogromny rozwój teorii gazu klasycznego w XIX wieku dał początek doświadczeniom, które z kolei wymagały dalszego rozwoju teorii. W ultraniskich temperaturach gaz, bozonowy lub fermionowy, wykazuje makroskopową spójność kwantową, która objawia się jako nadprzewodnictwo dla cząstek naładowanych, a jako nadciekłość w przypadku cząstek neutralnych. Ten nowy stan materii został dokładnie zbadany, zarówno teoretycznie, jak i eksperymentalnie, w XX wieku. Postępy w tej dziedzinie uitorowały drogę do odkrycia mnóstwa egzotycznych stanów materii.

Niniejsze badanie koncentruje się na teoretycznym odkryciu szczególnej egzotycznej konfiguracji, określanej mianem ferronu, w niezerównoważonym spinowo ultrazimnym gazie Fermiego. Pomimo że diagram fazowy dla ultrazimnego gazu Fermiego z polaryzacją spinową jest niekompletny, możliwe jest stworzenie metastabilnych stanów wzbudzonych, charakteryzujących się niskimi wartościami polaryzacji. Ferron powstaje w wyniku modulacji pola parowania, w obecności różnicy potencjałów chemicznych między składowymi spinowymi. Mechanizm ten jest zasadniczo podobny do tego, który stoi za złączem Josephsona- $\pi$  w złączach nadprzewodnik-ferromagnetyk-nadprzewodnik lub fazą Fulde-Ferrel-Larkin-Ovchinnikov. Dlatego badania zwiększonej stabilności ferronu oraz jego wewnętrznej struktury oraz właściwości mogą rzucić światło na tę długo poszukiwaną fazę, której jeszcze nie zaobserwowano doświadczalnie.

Praca ta zawiera krótkie wprowadzenie do tematyki spolaryzowanego ultrazimnego gazu Fermiego i skrzyżowania (ang. crossover) BCS-BEC z zarysem technik

eksperymentalnych. Drugi rozdział jest poświęcony teorii nadprzewodnictwa BCS, która jest ważna do zrozumienia metody Bogoliubowa-de Gennesa (BdG), twierdzenia Andreeva i zachowania pola parowania w skończonej temperaturze. W następnym rozdziale przedstawiono ramy techniczne symulacji układów wielociałowych. Opisano rozszerzenie teorii funkcjonału gęstości na układy nadciekłe. Model zwany asymetrycznym, przybliżeniem nadciekłej gęstości lokalnej (ang. time-dependent asymmetric superfluid local density approximation: TDASLDA) umożliwia symulację dynamiki gazu Fermiego spolaryzowanego spinowo. Zostało to zweryfikowane w licznych symulacjach na przestrzeni wielu lat.

Druga połowa pracy poświęcona jest ferronowi. W rozdziale czwartym przedstawiono sposób dynamicznego wytwarzania ferronu. Zbadano i wyjaśniono warunki do powstania ferronu oraz jego niezwykle stabilność. Ponadto zaprezentowano (jeszcze bardziej) egzotyczne konfiguracje ferronu, takie jak deformacje i koncentryczne ferrony oraz zderzenia ferronów. Rozdział czwarty zawiera także porównanie między BdG i TDASLDA oraz między słabym oraz silnym reżimem sprzężenia w układzie.

W rozdziale piątym ferron jest badany w statycznych, dwuwymiarowych układach. Przedstawiono zachowanie stanów Andreeva, które tworzą ferron. Ferrony uzyskują określoną wielkość w stosunku do występującej w układzie nierównowagi spinowej. Wykazano również, że można je uzyskać w skończonych temperaturach, które są w zasięgu eksperymentalnym, jeśli rozmiar obiektu jest wystarczająco duży. W szóstym rozdziale omówiono dynamiczne właściwości ferronu. Okazuje się, że istnieje prędkość krytyczna dla każdego ferronu, powyżej której nie może być on przyspieszany, ponieważ będzie się to wiązać z jego zniszczeniem. Krytyczna prędkość zależy od rozmiaru ferronu oraz amplitudy pola parowania. Ponadto badana jest reakcja ferronu na superprzepływ pod kątem jego bezwładności. Z przeprowadzonych badań wynika, że masa efektywna zależy w prosty sposób od wielkości ferronu. Przedstawiono jednak dodatkowy wkład pochodzący od amplitudy pola parowania. Ostatni rozdział zawiera podsumowanie i przyszłe aspekty.

Poniżej przedstawiono wykaz publikacji naukowych, na których oparta jest ta rozprawa:

- P. Magierski, B. Tüzemen, G. Wlazłowski, "Spin-polarized droplets in the unitary fermi gas", *Phys. Rev. A* **100**, 3 (2019).
- B. Tüzemen and P. Kukliński and P. Magierski and G. Wlazłowski, "Properties of spin-polarized impurities - ferrons, in the unitary fermi gas", *Acta Physica*

Polonia B, vol **51** (2020).

- P. Magierski, B. Tüzemen, G. Wlazłowski, "Dynamics of spin-polarized impurity in ultracold Fermi gas", Phys. Rev. A **104**, 3 (2021).

*Słowa kluczowe: ultrazimny gaz Fermiego z polaryzacją spinową, faza FFLO, stany związane Andreeva, nadciekłość nierównowagowa*



# Contents

<b>Acknowledgements</b>	<b>v</b>
<b>Abstract</b>	<b>vii</b>
<b>Streszczenie</b>	<b>ix</b>
<b>1 Introduction</b>	<b>1</b>
1.1 BCS–BEC crossover . . . . .	2
1.2 Spin–imbalanced ultracold Fermi gas . . . . .	5
1.3 Experimental techniques . . . . .	8
<b>2 BCS superconductivity</b>	<b>11</b>
2.1 The BCS model . . . . .	12
2.2 Mean–field Hamiltonian . . . . .	15
The BCS ground state . . . . .	19
2.3 The Bogoliubov transformation . . . . .	22
2.3.1 The BCS critical temperature . . . . .	23
2.3.2 HFB equations in coordinate space . . . . .	26
2.4 Andreev bound states . . . . .	27
<b>3 Modeling method and the numerical framework</b>	<b>33</b>
3.1 Density functional theory . . . . .	33
The Kohn–Sham equations . . . . .	34
3.2 Superfluid Local Density Approximation . . . . .	36
3.2.1 Spin–symmetric case . . . . .	37
Regularization . . . . .	38
3.2.2 Polarized case . . . . .	39
3.2.3 Time–dependent ASLDA . . . . .	42
3.3 Numerical details . . . . .	44

<b>4</b>	<b>Dynamic creation of spin-polarized impurity</b>	<b>49</b>
4.1	Stability of the ferron . . . . .	55
4.2	Basic dynamic properties of ferron . . . . .	62
4.2.1	Deformed ferron . . . . .	62
4.2.2	Concentric ferrons . . . . .	62
4.2.3	Collision of two ferrons . . . . .	63
4.3	Robustness of the phenomenon . . . . .	65
4.3.1	TDASLDA vs TDBdG . . . . .	65
4.3.2	UFG vs BCS . . . . .	66
<b>5</b>	<b>The internal structure of the ferron</b>	<b>69</b>
5.1	Andreev states inside the ferron . . . . .	69
5.2	The size of the ferron . . . . .	73
5.3	Semi-classical analysis of ferron . . . . .	77
5.4	Ferron at finite temperature . . . . .	82
<b>6</b>	<b>Dynamic properties of the ferron</b>	<b>85</b>
6.1	The critical velocity of the ferron . . . . .	85
	The ferron in the vicinity of vortex . . . . .	90
6.2	Effective mass of the ferron . . . . .	91
<b>7</b>	<b>Conclusions and outlook</b>	<b>99</b>
	<b>Bibliography</b>	<b>103</b>

# List of Figures

- 1.1 The qualitative phase diagram of the BCS–BEC crossover as a function of the dimensionless temperature  $T/\varepsilon_F$  and the dimensionless interaction parameter  $(a_s k_F)^{-1}$ . It can be seen that the spectrum can be roughly divided in three parts. 1) The BCS limit where  $(a_s k_F)^{-1} \rightarrow -\infty$ . 2) The BEC limit where  $(a_s k_F)^{-1} \rightarrow \infty$ . 3) The unitary limit where,  $(a_s k_F)^{-1} \rightarrow 0$ . The figure is taken from Ref. [16]. . . . . 4
- 1.2 The quasi–particle excitation spectra of the fully–paired BCS superfluid (a) and Sarma phase (b). The upper branches show the spectra for the spin–down particles and the lower branches show the spectra for spin–up particles. The BCS case shows the excitation gap whereas the Sarma case admits gapless excitations. The figure is taken from Ref. [24]. . . . . 6
- 1.3 The figure on the left–hand side shows the Fermi surfaces of non–interacting two–component polarized Fermi gas. It is clearly shown that the majority component has a larger Fermi surface. The figure on the right–hand side shows the Fermi surfaces of a paired system, where the Cooper pairs have a finite center of mass momentum  $q$ . This is compensated by the acquisition of finite momentum on the opposite side by the unpaired majority population. The figure is taken from Ref. [39]. . . . . 7
- 1.4 A sketch of the grand–canonical phase diagram at  $T = 0$  for the Fermi gas. On the horizontal axis, the scattering length and on the vertical axis the chemical potential difference is presented. As it can be seen, the picture is not complete even qualitatively. The figure is taken from Ref. [43]. . . . . 9
- 1.5 A basic model for Feshbach resonances. The scattering event that occurs with the energy  $E$  can be coupled to a bound state in a closed channel with the energy of  $E_c$ . The figure is taken from Ref. [12]. . . . . 10

2.1	The interaction considered in the Cooper problem. The particles with momenta and spins $\{\mathbf{k}, \uparrow\}$ and $\{-\mathbf{k}, \downarrow\}$ are scattered to $\{\mathbf{k}', \uparrow\}$ and $\{-\mathbf{k}', \downarrow\}$ as a result of an attractive interaction. . . . .	13
2.2	The occupations of energy levels according to BCS model. It can be seen that for $\Delta = 0$ , the levels below the Fermi level are completely occupied by particles ( $ v_k ^2$ ) whereas the levels above the Fermi level are completely occupied by holes ( $ u_k ^2$ ). When $\Delta \neq 0$ , the particle and hole states mix. . . . .	21
2.3	The behaviour of the magnitude of the pairing field as a function of temperature. The estimation of the BCS theory is compared with experimental results obtained by different superconductors. The figure is taken from Ref. [63]. . . . .	25
2.4	The SNS junction. The regions 1 and 3 are superconductors and the region 2 is the normal part in between. The particle with the energy $E$ reflects as a hole having the energy $-E$ (relative to the Fermi level). As a result a Cooper pair nucleates inside the superconductor. . . . .	29
3.1	A schematic representation of equivalence between a real fermionic system under a harmonic potential (left) and Kohn–Sham framework (right). A set of interacting particles under a trivial external potential $V_{\text{ext}}$ can be mapped to a set of non–interacting particles under the influence of a more complicating external potential. . . . .	35
3.2	The extraction of the effective mass parameter $\alpha$ from three cases $p = -1$ , $p = 0$ , and $p = 1$ indicated by green ticks. Resulting fit is given in Eq. (3.23a). The figure is taken from Ref. [68]. . . . .	40
3.3	The comparison between the Superfluid Local Density Approximation (SLDA) and the <i>ab initio</i> fixed–node diffusion Monte Carlo (FNDMC) calculations performed for a harmonically trapped unitary Fermi gas at zero temperature. The figure is taken from Ref. [68]. . . . .	41
3.4	The comparison between block, cyclic and block–cyclic (bc) methods. Bc method is a compromise between the other methods. For more details see Ref. [83]. . . . .	45
3.5	Profiling of TDSLDA code executed on 512 GPUs (Piz Daint). For more details see Ref. [83]. . . . .	47

- 4.1 The schematic of the spin-selective external potential (left subfigure) and an example of time evolution of the total energy of the system (right subfigure). Both images are taken from Ref. [46]. . . . . 51
- 4.2 **Left subfigure:** The behavior of the pairing field within a SFS junction. The phase of the pairing field is shifted by  $\pi$  across the junction. **Right subfigure:** The structure of the polarized shell in 3D. On the left-hand side of the figure the local spin polarization,  $p(\mathbf{r})$  and on the right-hand side the local pairing strength,  $|\Delta(\mathbf{r})|$  is shown. . . . . 52
- 4.3 Two snapshots of the dynamical creation of the ferron is presented. The upper subfigure is a snapshot while the potential is applied, and the lower subfigure is after the potential is turned off. The potential is turned off at  $t\varepsilon_F = 150$ . In both figures, on the left half-box, the magnitude of the pairing field is presented, while on the right half-box, the phase of the pairing field is given. The right image in both figures is the local spin-polarization. . . . . 53
- 4.4 The effect of the periodic box size on the creation of a stable droplet. The polarization and the phase difference are calculated at the center of the box as a reference to the bulk values. **Upper subfigure:** Panel a) shows the time evolution of the relative local polarization for different box sizes. Panel b) shows the time evolution of the phase difference. The vertical dashed lines represent when the external potential is completely turned off ( $t\varepsilon_F = 150$ ). The horizontal dashed line in the panel b) is a guide to the eye, showing  $\delta\varphi = \pi$ . **Lower subfigure:** This figure demonstrates the relative phase difference and the polarization. The bulk values are taken from the edge of the box. . . . . 54

- 4.5 The time evolution of the ferron is presented. The box size is  $L = 31.42\zeta$ . **Upper subfigure:** Small, medium, and large potential widths are compared. In panel a), the local polarization from the center of the box is presented. In panel b), the phase difference between the center of the box and the bulk is shown. It can be seen if the potential is too narrow ( $\sigma = 2.36\zeta$ ), the nodal shell does not survive. In the case of wide potential ( $\sigma = 7.07\zeta$ ), the given system parameters, such as the amplitude of the potential or the application duration, are not enough to break enough Cooper pairs to create a phase shift. **Upper subfigure:** The stability of the ferron in intermediate potential sizes are shown. The presentation of the results is the same as the above subfigure. . . . . 56
- 4.6 **Upper subfigure:** The effect of the duration of the application of the external potential is presented. The amplitude of the potential is  $A_0 = 2\varepsilon_F$  and the width is  $\sigma = 7.07\zeta$ . It can be seen that for wide potentials, increased duration of the application helps to break enough Cooper pairs to create the necessary shift in the phase between the core and the bulk. The vertical dashed lines represent the time where the external potential is completely turned off for different cases. The horizontal dashed line is a guide to the eye, showing  $\delta\varphi = \pi$ . **Lower subfigure:** The effect of the amplitude of the external potential. The box size is  $L = 37.7\zeta$ , and the width is  $\sigma = 4.71\zeta$ . Panel a) shows the local relative polarization, and panel b) shows the phase difference from the center of the box to the bulk value. Among three selected amplitudes, only  $A_0 = 2\varepsilon_F$  produces a stable ferron. The vertical dashed line represents when the external potential is completely turned off ( $t\varepsilon_F = 150$ ). . . . . 57
- 4.7 The creation of ferron with different switching on/off rates,  $t_{switch}$ . Panel a) shows the local polarization in the core of the potential with respect to the bulk. Panel b) shows the phase difference. In panel c) the effect of different switching on/off rates is presented. It can be seen that in all cases, a stable ferron is successively produced. The vertical dashed lines represent the time where the external potential is completely turned off ( $t\varepsilon_F = 150$ ), and the horizontal dashed line is a guide to the eye, showing  $\delta\varphi = \pi$ . . . . . 58

- 4.8 The snapshots of time-dependent 1D calculations. The left-hand side shows the strength of the pairing field relative to the Fermi energy. The right-hand side shows the phase of the pairing field in units of  $\pi$ . The parameters used in Eq. (4.4) are  $k_F\sigma = 4.441$ ,  $T = T_1 = 29.55\varepsilon_F^{-1}$ , and  $T_2 = 49.25\varepsilon_F^{-1}$ . The external potential is completely turned off at  $t\varepsilon_F = 78.8$ . Both snapshots are taken after the external potential is turned off. . . . . 60
- 4.9 The energy of the 1D system with the presence of two nodal points. On the x-axis, the distance between two nodal lines in units of coherence length is presented. Y-axis shows the total energy of different configurations with respect to the free Fermi gas. It can be seen that the energy decreases as the distance between the nodal points increases. . . . . 61
- 4.10 **Left subfigure:** Two snapshots on dynamic creation of a deformed ferron. The box size is  $L = 47.12\zeta$ . The amplitude of the Gaussian potential is  $A_0 = 2\varepsilon_F$  with the width of  $\sigma = 4.71\zeta$ . The spherical shape is deformed by the parameters  $\varepsilon_y = 0.44$ , and  $\varepsilon_z = 0.64$  used in Eq. (4.1). The top and bottom rows show the cross sections of the pairing field along three perpendicular planes. The top row shows the configuration just before the external potential is turned off. The bottom row shows the initially deformed impurity rearranges itself to a spherical form. The black dashes are guide to the eye. **Right subfigure:** Snapshot of the attempt on creating concentric ferrons. The images are taken at  $t\varepsilon_F = 392$  which is approximately  $220t\varepsilon_F$  after the potential is turned off. The box size is  $L = 50.26\zeta$ . The amplitude the width of the potential are  $A_0 = 3.5\varepsilon_F$  and  $\sigma = 11.78\zeta$  respectively. Both figures are taken from Ref. [46]. . . . . 63
- 4.11 Four scenarios of ferron collision. In all cases, the box size is approximately  $50 \times 31 \times 31 \zeta^3$ . The width of the polarizing potentials is  $\sigma = 3.14\zeta$  with the amplitude  $A_0 = 2\varepsilon_F$ . The external potentials move towards each other with the velocity  $v = 0.45v_F$ . The potentials are completely removed at  $t\varepsilon_F = 150$ . On left-hand side the configurations right after the potentials are removed are presented. On the right-hand side the configurations at  $t\varepsilon_F = 766$  can be seen. The first row shows the head-on collision of two identical ferrons. The second row shows the peripheral collision of identical ferrons. The third row consists head-on collision of ferrons of opposite polarization. Finally the fourth row shows the peripheral collision of ferrons of opposite polarization. . . . . 64

- 4.12 **Left subfigure:** The ferrons existence and stability under the BdG approach is shown. The box size is  $L = 31.42\zeta$ . The maximum strength of the potential is  $A_0 = 1.5\varepsilon_F$  and the width of the Gaussian potential is  $\sigma = 4.71\zeta$ . The potential is applied from the beginning until  $t\varepsilon_F = 150$ . The total excitation energy ( $E_{ex} = E(t) - E(0)$ ) and the phase difference between the bulk and the core  $\delta\varphi/\pi$  are shown as functions of time. The inset shows the internal structure at the time indicated by the dashed line,  $t\varepsilon_F \approx 225$ . **Right subfigure:** In 1D calculations the energy cost to keep two nodal lines stable in a polarized system are shown by the red solid line. The dashed lines indicate the pairing energy for the same polarized configuration. The dotted lines show the pairing energy for uniform configuration. Both figures are taken from Ref. [46]. . . . . 66
- 5.1 **Right subfigure:** A 2D schematic of ferron. The Andreev states are localized at the vicinity of the nodal line (red area), where the phase of the pairing field shifts by  $\pi$ . The image is taken from Ref. [88]. **Left subfigure:** A 2D schematic demonstrating two different semi-classical trajectories for particles occupying Andreev states. . . . . 70
- 5.2 The solutions for Eq. (5.9) (left subfigure) and Eq. (5.10) (right subfigure). It can be seen that there always exist a solution for both equations. Insets in both figures shows the behavior of the dimensionless parameter,  $\alpha$  as a function of the angular momentum,  $L$ . . . . . 72
- 5.3 The ground state configuration of the ferron. From left to right, the local polarization, the strength of the pairing field, and the phase of the pairing field are shown. The figure is taken from Ref. [88]. . . . . 74
- 5.4 A 1D cross-section of the simulation box. Panel a) and b) show the local polarization and magnitude of the pairing field for different global polarization values. Panel c) shows the radius of the nodal circle for different global polarization values. The blue dots are the radii extracted from the system. The dashed red line shows the linear equation,  $2k_F R + 1$  where  $R = R_c + \zeta$ . . . . . 75
- 5.5 The angular momentum states inside the ferron ( $m$ ). The energy is shifted by  $\delta\mu/(2|\Delta|)$ . The vertical lines show the values of  $-\delta\mu/(2|\Delta|)$  and  $\delta\mu/(2|\Delta|)$ . The box size is  $70k_F^{-1} \times 70k_F^{-1}$ . The spin-imbalance is  $\delta N = 31$ . The strength of the pairing field is  $|\Delta|/\varepsilon_F \approx 0.44$ . . . . . 76

- 5.6 The positive branch of angular momenta and energies are shown for different sizes of ferron. The dotted values represent the solutions obtained from numerical calculations. The dashed lines show the analytical estimations obtained from the Andreev approximation. The vertical lines show the values of corresponding chemical potentials. The system settings are the same as Fig. 5.5. **Upper subfigure:** The analytical solutions show discrepancy for small ferron sizes. **Lower subfigure:** The discrepancy is treated by considering the tunneling events through the ferron interior. . . . . 78
- 5.7 A schematic of potential wells.  $d$  is the length of the junction where the magnitude of the pairing field drops to zero.  $w$  is the width of the ferron interior where the phase of the pairing field is shifted by  $\pi$ . . . . . 79
- 5.8 The effect of the finite temperature in 2D static calculations. As the temperature increases, the ferron gets smaller. Eventually, the nodal structure is destroyed. Insets show the structure of the pairing field with a color code same as Fig. 5.3. The spin-imbalance is  $\delta N = 31$ . . . . . 82
- 5.9 The 3D dynamic creation of ferron under finite temperature. Panel a) shows the time evolution of local polarization in the center of the object. Panel b) shows the pairing phase difference. The box size is  $L \approx 41$ . The amplitude of the potential was fixed at  $A_0 = 2\varepsilon_F$ . The width of the spin polarizing potential is  $\sigma = 4.71\zeta$ . The vertical dashed line shows the time where the external potential is turned off. The horizontal dashed line is a guide to the eye pointing to the value of  $\delta\varphi = \pi$ . Inset shows the time-averaged polarization in the center of ferron for various temperatures. The dashed blue line is a guide to the eye. . . . . 83

- 6.1 **Upper subfigure:** The position of the moving ferron inside a box corresponding to lattice size  $68 \times 40 \times 40$  which corresponds to  $53\zeta \times 31\zeta \times 31\zeta$ . The width of the polarizing potential is  $\sigma k_F = 6$  and its amplitude is  $A_0 = 2\varepsilon_F$ . The potential is switched on at  $t\varepsilon_F = 50$  and completely removed at  $t\varepsilon_F = 150$ . Different data sets correspond to different dragging velocities. **Lower subfigure:** Velocity of the ferron in the final state as a function of the dragging velocity. The time-dependent spin-selective potential is dragged along the  $x$ -axis during its application. The horizontal dashed lines shows the "plateau" of the final velocity for various sizes of ferrons corresponding to:  $\sigma k_F = 8$ ,  $\sigma k_F = 6$ ,  $\sigma k_F = 4$  from top to bottom, where  $\sigma$  is the width of the Gaussian potential. Inset shows the absolute value of the pairing field in the left column, while in the right column, the phase of the pairing field is shown. The images are taken after the external potential is turned off while the ferron is moving. All three configurations correspond to  $v_{\text{drag}}/v_F = 0.06$ . The figure is taken from Ref. [89]. . . . . 86
- 6.2 Structure of the spectrum of Andreev states exposed to different strengths of superflow. **Left subfigure:** Magnetic quantum numbers  $m$  corresponding to Andreev states are shown for two velocities of the superflow:  $q/v_F = 0.01$  (filled circles) and  $q/v_F = 0.05$  (empty diamonds), where  $v_F$  denotes Fermi velocity. **Right subfigure:** The expectation value of the momentum operator component, parallel to the direction of the superflow is shown for Andreev states. The quasiparticle energies have been shifted by  $\frac{1}{2}\delta\mu$  and therefore the plots on both subfigures possess symmetry with respect to  $E = 0$ . The shifted energy values corresponding to  $\pm\frac{1}{2}\delta\mu$  have been denoted by vertical dashed lines. The spin imbalance corresponds to  $\delta N = 31$  ( $R \approx 6.2\zeta$ ) and the strength of the pairing field  $|\Delta|/\varepsilon_F = 0.44$ . The figure is taken from Ref. [89]. . . . . 88
- 6.3 The expectation value of the momentum operator for different sizes of the ferron. All three sizes are subjected to the superflow  $q = 0.03v_F$ . The figure is taken from [89]. . . . . 90
- 6.4 The ferron critical velocity as a function of the magnitude of the pairing field  $|\Delta|/\varepsilon_F$  and the spin imbalance  $\delta N$ . Inset shows an example of two different sizes of ferron having the same critical velocity where the smaller ferron is deformed. The figure is taken from Ref. [89]. . . . . 91

- 6.5 Snapshots showing the attempt to create a stable ferron solution in the presence of the vortex. The time-dependent potential to generate the ferron is turned off at  $t\varepsilon_F = 150$ . The vortex, with the core located in the center, creates currents rotating counter-clockwise. It is visible that ferron is destroyed because of these currents. The polarization inside the ferron is pushed to the boundary of the system. The figure is taken from Ref. [89]. . . . . 92
- 6.6 The response function in Eq. (6.8) as a function of the superflow velocity  $q$ . Symbols correspond to numerical calculations. Lines are obtained as a result of interpolation. The value of effective mass is extracted in the limit of  $q \rightarrow 0$  and denoted by symbols. The results for two values of the pairing field are shown:  $\Delta/\varepsilon_F = 0.365$  (panel a) and for  $\Delta/\varepsilon_F = 0.552$  (panel b). The lattice size is  $(70k_F^{-1})^2$  where  $k_F \approx 1$ . The figure is taken from Ref. [89]. . . . . 95
- 6.7 **Left subfigure:** The effective mass  $M_{\text{eff}}$  as a function of the magnitude of the pairing field  $|\Delta|/\varepsilon_F$  and the spin imbalance  $\delta$ . In all cases the total number of particles in the simulation box is  $N = N_\uparrow + N_\downarrow = 770$  and the Fermi momentum  $k_F = \sqrt{2\varepsilon_F} \approx 1$ . The values of  $\delta N = 21, 41$  correspond to the ferron radii  $R \approx 4.0\zeta$  and  $R \approx 8.3\zeta$ , respectively, where  $\zeta = \frac{1}{k_F} \frac{\varepsilon_F}{|\Delta|}$ . **Right subfigure:** The excitation energy of the system  $E_{\text{ex}}(q)$  as a function of velocity  $q$  obtained in BdG calculations (lines). The kinetic energy of the ferron  $E_f(q)$  obtained using the extracted effective mass (points). Both energies are shown in units of non-interacting Fermi gas  $E_{\text{ffg}}$ . The spin-imbalance in the system is  $\delta N = 41$ . The lattice size is  $(70k_F^{-1})^2$  where  $k_F \approx 1$ . The figure is taken from Ref. [89]. . . . . 97



To my grandmother...



# Chapter 1

## Introduction

The description of the Fermi gas has come a long way since its first conceptualization. The empirical attempts to describe the behavior of the classical non-interacting (ideal) gas during the 18th and 19th centuries eventually yielded to an equation of state known as *ideal gas law*. This understanding has brought up the thermodynamic cycles allowing to build heat engines and coolers. The first decade of the 20th century was when Kamerlingh Onnes utilized the Hampson–Linde cycle to cool down the helium to its liquid state. He then continued his low-temperature studies to observe the effects of temperature on electrical conductivity. He expected to find a linear relationship between the electrical resistance and the temperature. Since the third law of thermodynamics states that to reach absolute zero is impossible, a linear relationship that can be extrapolated to absolute zero would confirm the hypothesis. However, this was not the case. In 1911, Onnes' experiments on mercury showed a sharp decrease in the resistance at  $T = 4.2\text{K}$ ; it has vanished [1]. He named this new state of matter as *superconducting state*.

Following the discovery of superconductivity, there has been extensive research on low-temperature physics. Phenomenological studies showed the repulsion of the external magnetic field from the superconductor, known as the *Meissner effect* [2]. Later on, superfluidity was discovered in an isotope of helium  $^4\text{He}$ , where the fluid flow shows no viscosity when it is cooled under a certain temperature [3].

Simultaneous advances in formulating quantum mechanics have made it possible to provide a microscopic description for both Fermi and Bose gases. Contrary to the classical gas described by Maxwell–Boltzmann distribution, the quantum gases are described by Fermi–Dirac distribution for particles with half-integer spins (fermions) and by Bose–Einstein distribution for particles with integer spins (bosons). The main difference between fermions and bosons originates from the Pauli principle. Multiple bosons are allowed to occupy the same quantum state, whereas, for fermions, only one

particle is allowed to occupy a quantum state. As predicted by Bose [4] and Einstein [5] and showed experimentally by Cornell, Wieman, and Ketterle [6, 7], in temperatures close to absolute zero, multiple identical bosons occupy the same quantum state with the lowest energy. Macroscopic occupation of a single quantum state causes a phase transition resulting in a new state of matter called Bose–Einstein condensate (BEC). For this reason, the superconductivity in metals composed of Fermi gas and superfluidity of bosonic  $^4\text{He}$  atoms are initially thought to be originated from different sources. Today, we know that this statement is incomplete. In fact, another helium isotope,  $^3\text{He}$ , even though it obeys Fermi–Dirac statistics, when it is cooled down, it also becomes superfluid [8, 9]. In 1941, Landau showed in his phenomenological model that the superconductivity in metals can be actually understood in terms of superflow of charged particles in the macroscopic sense [10]. Milestone of the microscopic description of superconductivity was established in 1957. Bardeen, Cooper, and Schrieffer (BCS) showed that in low temperatures, an attractive interaction between electrons of any kind and any strength results in the pairing of electrons of opposite spins occupying the same quantum state near the Fermi surface [11]. With the formation of the Cooper pairs, the Fermi surface becomes unstable, and a pairing gap opens. The magnitude of the pairing gap sets the minimum energy required to obtain a single-particle excitation. Hence, any perturbation, such as friction or electrical resistance, below the pairing strength would fail to break the Cooper pairs.

In practice, one of the possible sources of this attractive interaction between electrons in a metal is mediated by the lattice vibrations, phonons. In ultracold gases, the mechanism of Cooper pair creation is possible by using an external magnetic field to tune the interactions between the particles by Feshbach resonances resulting in a superfluid phase in a neutral charged Fermi gas [12].

## 1.1 BCS–BEC crossover

Initially, it was thought that the BEC of diatomic molecules and BCS-type superconductivity in metals are originated from different sources. In the metallic superconductivity, two length scales are essential; the inter-particle distance  $k_F^{-1}$  and the size of a Cooper pair  $\xi$  (also known as the coherence length). In the weak-coupling regime, where the pairing correlations are weak compared to the Fermi energy  $\varepsilon_F$ , the size of a Cooper pair is considerably longer than the inter-particle distance. Therefore, in a

weakly paired BCS superfluid, the Cooper pairs overlap. In contrast to the BCS, the BEC is formed by bosonic bound states of tightly packed fermions.

The idea to consider the BCS and the BEC regimes as two extremes of the same phenomenon sprouted with the work done by Eagles in 1969. He studied superconductivity at low densities, where the interaction strength is comparable with the Fermi energy [13]. In the '80s, with two seminal papers by Leggett [14], and Nozières and Schmitt–Rink [15], the idea of the transition from BCS to BEC or vice versa as a function of the s–wave scattering length  $a_s$  have settled. The scattering length sets the strength of the interaction between the particles. It is negative in the case of weak attraction between the particles as in BCS superfluidity and positive when the bosonic bound state is formed by two fermions that have intrinsic repulsive interaction due to the Pauli principle. A schematic of this crossover is shown in Fig. 1.1.

The interesting phenomenon happens when the scattering length is much larger than the inter–particle distance,  $|a_s k_F| \gg 1$ , in a dilute system where the effective range of interaction  $r_e$  is much smaller than the inter–particle distance,  $r_e k_F \ll 1$ . In other words, this limit is reached when the dimensionless parameter goes to zero,  $(a_s k_F)^{-1} \rightarrow 0$ . Then, the interaction range drops out, and only a meaningful parameter becomes the Fermi momentum, hence the particle density  $n = k_F^3/3\pi^2$ .

The limit where  $(a_s k_F)^{-1} \rightarrow -\infty$  is the BCS limit, and the limit where  $(a_s k_F)^{-1} \rightarrow \infty$  is the BEC limit. The crossover from large Cooper pairs to point like bosons is a smooth one, and the regime in the middle of this crossover, where  $(a_s k_F)^{-1} \rightarrow 0$  is called the *unitary Fermi gas*. In this regime, all the system properties, such as the ground state energy and thermodynamic response functions, can be expressed in particle density. In particular, George Bertsch argued that the relation between the ground state energy of a non–interacting Fermi gas and the unitary Fermi gas [17]:

$$E_{\text{unitary}} = \zeta_B E_{\text{FFG}} = \frac{3}{5} \varepsilon_F N \zeta_B. \quad (1.1)$$

The dimensionless parameter  $\zeta_B$  is called the Bertsch parameter. In finite temperatures, it is a function of the temperature and the Fermi energy,  $\zeta_B(T/\varepsilon_F)$ . An important remark is that the case where the scattering length is infinitely larger than the effective range of interaction is a rare one. The relation  $a_s \gg r_e$  approximately holds in the crust of neutron stars composed by the dilute neutron matter [18] or, it can be generated in a laboratory by Feshbach resonances [12].

A remarkable property of the unitary Fermi gas is its exceptionally strong pairing

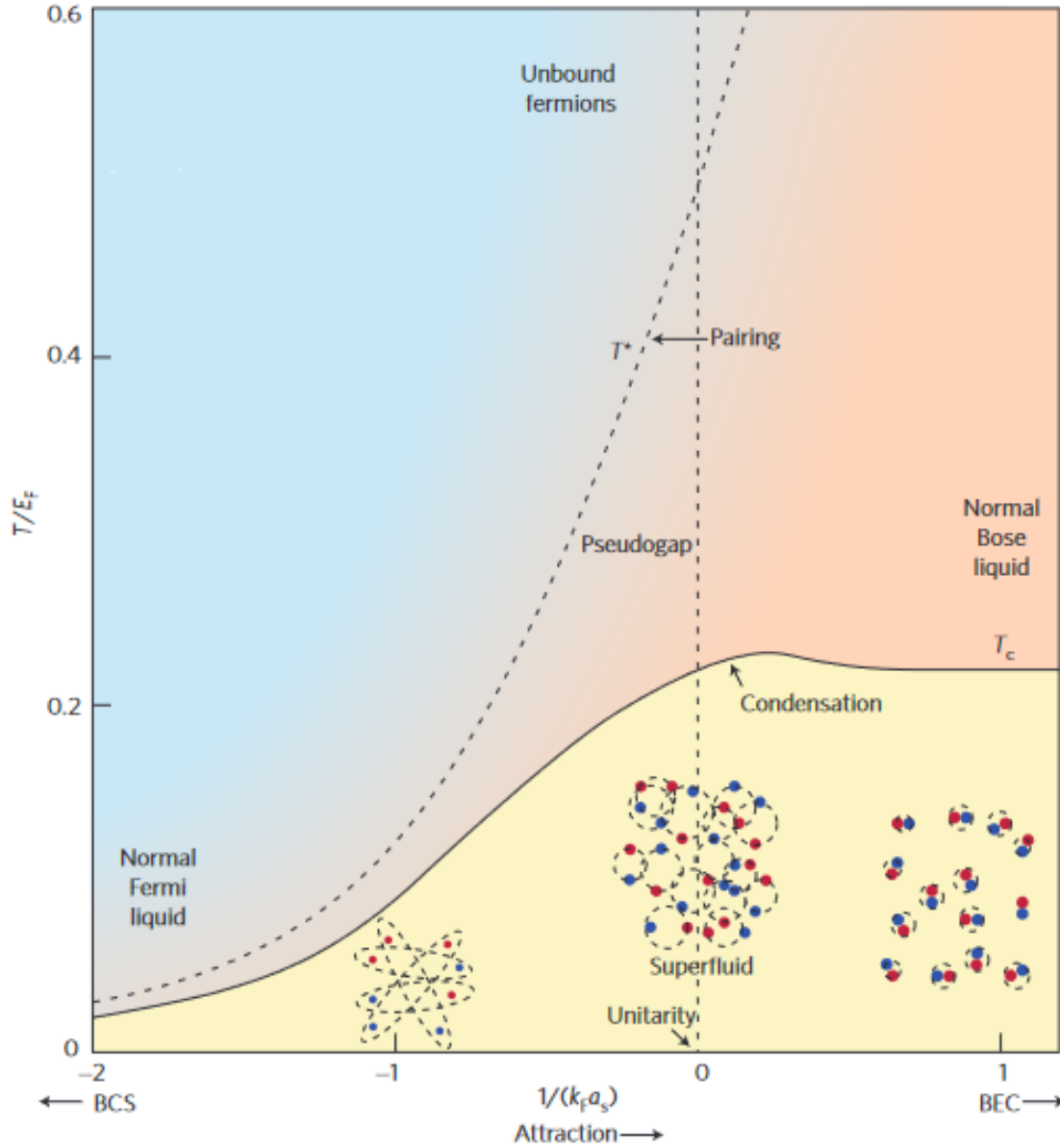


FIGURE 1.1: The qualitative phase diagram of the BCS–BEC crossover as a function of the dimensionless temperature  $T/\epsilon_F$  and the dimensionless interaction parameter  $(a_s k_F)^{-1}$ . It can be seen that the spectrum can be roughly divided in three parts. 1) The BCS limit where  $(a_s k_F)^{-1} \rightarrow -\infty$ . 2) The BEC limit where  $(a_s k_F)^{-1} \rightarrow \infty$ . 3) The unitary limit where,  $(a_s k_F)^{-1} \rightarrow 0$ . The figure is taken from Ref. [16].

field. As the scattering length diverges, the loose Cooper pairs become tighter, and the strength of the pairing field increases. Unitary Fermi gas corresponds to the strongest pairing field where the strength of the pairing field  $\Delta$  becomes comparable with the Fermi energy,  $|\Delta| \approx 0.5\varepsilon_F$  [19–21], and the size of a Cooper pair decreases to the order of the inter–particle distance. This strong pairing interaction means the unitary Fermi gas is more robust to perturbations such as pair–breaking or thermal excitations than the BCS superfluid.

## 1.2 Spin–imbalanced ultracold Fermi gas

The ground state of a fermionic superfluid is composed of Cooper pairs. The pairing interaction may occur between different types of pairs. The most common and the simplest type of interaction is the s–wave pairing which couples fermions of the opposite spins and momenta. Therefore, the ground state configuration of an s–wave superfluid is composed of an equal spin population,  $N_\uparrow = N_\downarrow$ .

When a spin–flipping process occurs by a polarizing external potential such as a magnetic field, the fermions composing the Cooper pairs start to align according to this external potential; a Cooper pair made of fermions with opposite spins gets broken, and both fermions obtain the same spin. The number of broken Cooper pairs is related to work performed by the external potential. A decrease in the number of Cooper pairs lowers the magnitude of the pairing field. Chandrasekhar [22], and Clogston [23] showed that the spin–imbalance (or spin–polarization) is related with the strength of an external magnetic field  $B$  as the following:

$$\tilde{\mu} = \frac{\mu_\uparrow - \mu_\downarrow}{2} = \frac{\gamma B}{2}, \quad (1.2)$$

where  $\tilde{\mu}$  is the chemical potential difference caused by the spin–imbalance, and  $\gamma$  is the gyromagnetic ratio. Moreover, they showed that when the chemical potential difference reaches a critical value, a first–order phase transition happens where the superfluidity is destroyed altogether, leaving a normal spin–polarized Fermi gas behind. The critical chemical potential difference is:

$$\tilde{\mu}_c = \frac{|\Delta_0|}{\sqrt{2}}, \quad (1.3)$$

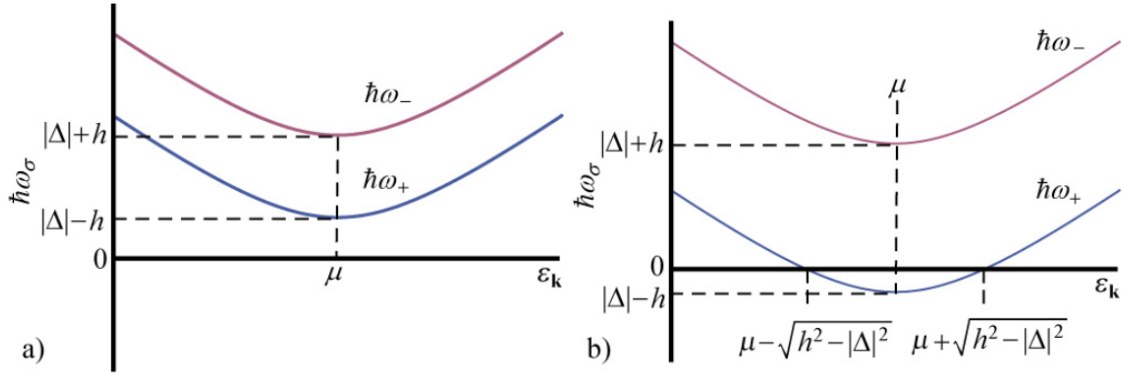


FIGURE 1.2: The quasi-particle excitation spectra of the fully-paired BCS superfluid (a) and Sarma phase (b). The upper branches show the spectra for the spin-down particles and the lower branches show the spectra for spin-up particles. The BCS case shows the excitation gap whereas the Sarma case admits gapless excitations. The figure is taken from Ref. [24].

where  $|\Delta_0|$  is the magnitude of the pairing field at  $\tilde{\mu} = 0$ . Therefore, there is a limiting value for the spin-imbalance in a system that persists superfluidity, and this critical value is directly related to the strength of the initial pairing field.

Later on, it was shown by Sarma [25] that there is an exotic phase for the imbalanced case where the superfluid and the normal state coexists. In Fig. 1.2(a) the excitation spectrum for BCS is shown. It can be seen that for a quasi-particle excitation in both spin species, there is an energy cost (gap), meaning the expulsion of the unpaired quasi-particle from the superfluid. In the Sarma phase, presented in Fig. 1.2(b), both gapped and gapless excitations are possible. The gapless excitations provide a spin-polarization around the average chemical potential  $\mu$ . This creates a phase separation in the momentum space. Namely, the spin-polarized quasi-particles occupy a limited number states around the momentum  $|\mathbf{k}| = (2m\mu)^{1/2}/\hbar$ . For the high and low momenta, the excitation spectrum is gapped, so these states are described within the BCS theory. Therefore, the Sarma phase allows the coexistence of normal and superfluid phases. Although the Sarma phase has gathered a lot of attention from the community [26–28], it turned out to be an unstable phase and has not been confirmed experimentally yet.

Approximately 40 years after the proposal of the Sarma phase, Liu and Wilczek extended the spin-imbalance case to both spin and mass imbalances [29]. The addition of the mass-imbalance is motivated by the superfluidity in dense quark matter, where six different quark flavors have unique masses. It was shown that in the zero-temperature

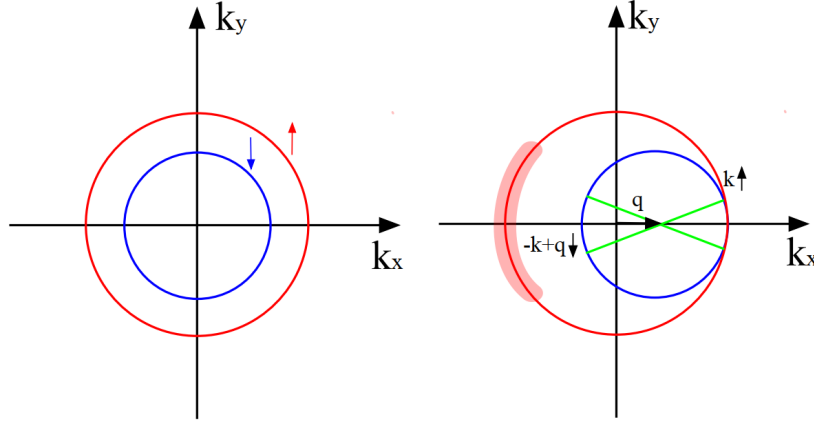


FIGURE 1.3: The figure on the left-hand side shows the Fermi surfaces of non-interacting two-component polarized Fermi gas. It is clearly shown that the majority component has a larger Fermi surface. The figure on the right-hand side shows the Fermi surfaces of a paired system, where the Cooper pairs have a finite center of mass momentum  $q$ . This is compensated by the acquisition of finite momentum on the opposite side by the unpaired majority population. The figure is taken from Ref. [39].

limit, this so-called "breached pair" phase is stable [30, 31].

The Sarma and breached pair phases are not the only scenarios that admit polarized particles into a superfluid system. There are various other phenomena such as polarized vortex cores [32–34], liquid crystals [35], or supersolids [36] where the unpaired particles can coexist with the superfluid. However, in relation to this study, one idea which was proposed by Fulde–Ferrel (FF) [37], and Larkin–Ovchinnikov (LO) [38] stands out.

The idea behind the FFLO (or LOFF) state is to attribute a finite momentum to the Cooper pairs due to the shift in the Fermi surfaces (see Fig. 1.3). In an ordinary  $s$ -wave superfluid, the Cooper pairs are composed of fermions having the opposite momenta and spins  $\{k, \uparrow\}$  and  $\{-k, \downarrow\}$ . In the FFLO picture, the Cooper pairs obtain a center of mass momentum  $q$  related to the spin–imbalance. Therefore, the pairing occurs between the pairs  $\{k + q/2, \uparrow\}$  and  $\{-k + q/2, \downarrow\}$ . This induces a spatial modulation in the pairing field with the period of  $2\pi/q$  [40]. Historically, FF proposed a modulation that has the form  $\Delta(\mathbf{r}) \sim |\Delta|e^{i\mathbf{q}\cdot\mathbf{r}}$  and LO proposed a form of  $\Delta(\mathbf{r}) \sim |\Delta| \cos \mathbf{q} \cdot \mathbf{r}$ . However, these are just the basic forms for the pairing field, and in reality, the spatial modulation of the pairing field may have a more complicated structure, such as different superpositions of FF and LO type of pairings. Although the FFLO phase has been

studied extensively [39–41], the experimental confirmation is still lacking.

A qualitative phase diagram of ultracold Fermi gas as a function of the scattering length and temperature is given at Fig. 1.1. There have been numerous attempts to obtain another phase diagram where the chemical potential difference (or polarization) enters as a degree of freedom [19, 42–45]. While there is no solid consensus on a phase diagram of polarized ultracold Fermi gas (see Fig. 1.4), it is instructive to consider excited meta-stable structures where the polarization can be stored locally in a superfluid environment. This thesis aims to show that there is indeed such a structure in the form of a spin-polarized droplet with remarkable stability. This excited meta-stable configuration is dubbed as *ferron* [46]. During the study of this thesis, stable spin-polarized solutions of Ginzburg–Landau approach are reported [47]. Although these objects are described as soliton sacks, their structure coincides with the ferron.

Two subsequent chapters of this thesis deal with the theoretical background where the BCS problem is studied in detail and the numerical framework considered to study the ultracold Fermi gas. In Chapter 4, a time-dependent scenario for the creation of the ferron is shown. Moreover, this chapter discusses the stability of the droplet and presents some more exotic configurations such as deformations or concentric ferrons. Chapter 5 discusses the minimum-energy configuration of the ferron in static calculations. The inner structure of the ferron and some fundamental relations are studied in this chapter. Finally, Chapter 6 puts the ferron in a superflow and studies the parameters that govern the motion of the ferron, such as its critical velocity and inertia.

### 1.3 Experimental techniques

The theory of ultracold quantum gases, both bosonic and fermionic, has been extensively studied from the beginning of the 20th century. However, the macroscopic quantum coherence was first realized at the turn of the century, in 1995, using bosonic alkali atoms of Rubidium [6] and Sodium [7]. To obtain such a system, the bosonic gas has to be cooled down to microkelvins, where it undergoes a phase transition to BEC state. In order to achieve that, a rather sophisticated approach has been used [48]. Initially, the atoms were cooled down to a degree by laser cooling technique. The main idea behind laser cooling is to slow down the high-temperature  $^{87}\text{Rb}$  atoms using a laser beam applied in the opposite direction. The atoms absorb the laser beam, and as a result of the radiation, the atoms slow down. In particular, the atoms in motion do not have a fixed direction. The direction of the laser beam, however, is fixed. As a result of the Doppler

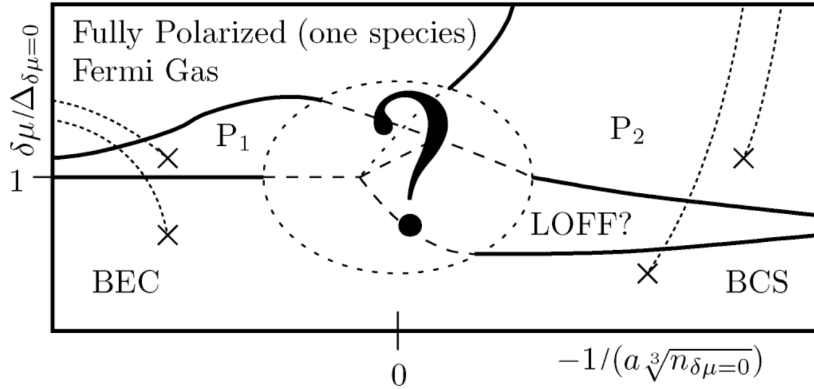


FIGURE 1.4: A sketch of the grand-canonical phase diagram at  $T = 0$  for the Fermi gas. On the horizontal axis, the scattering length and on the vertical axis the chemical potential difference is presented. As it can be seen, the picture is not complete even qualitatively. The figure is taken from Ref. [43].

effect, the atoms moving in the same direction as the laser have a reduced rate of absorption. The atoms moving in the opposite direction than the laser have an increased rate of absorption. The technique called "optical molasses" employs the Doppler effect by utilizing multiple laser beams. Having multiple laser beams oriented in different directions creates a viscous environment for the atoms allowing the experimentalists to slow down the atoms more efficiently [49].

When the atoms are slow enough, they can be captured by magnetic and optical traps for further manipulation. The final step is to expel the high-energy particles from the system, i.e., by applying a microwave with a specific frequency to excite the high-energy particles outside the trap. After that, the system is left to thermalize to a colder temperature. This process, called evaporative cooling, has been crucial to realizing the ultra-low temperatures necessary to obtain a BEC.

After the realization of BEC, it took the experimentalists only four years to achieve an ultracold Fermi gas using alkali atoms of  $40$  K. In 1999, a quantum degenerate Fermi gas was obtained [50]. It has been followed by the fermionic condensation [51], the observation of the pairing gap [52], and finally, the superfluid properties of the ultracold Fermi gas were completely proven with the observation of the vortices [53].

The interaction between the particles is characterized by the  $s$ -wave scattering length  $a_s$ . Feshbach resonances can tune both the magnitude and sign of the scattering length [12, 54], which in practice means the application of an external magnetic field. The basic idea is the following: During an elastic two-body scattering, the particles

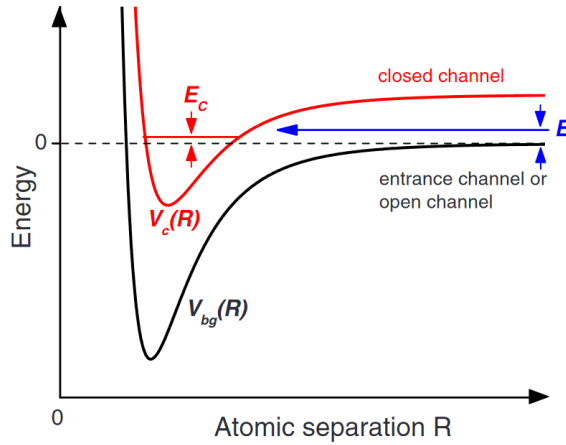


FIGURE 1.5: A basic model for Feshbach resonances. The scattering event that occurs with the energy  $E$  can be coupled to a bound state in a closed channel with the energy of  $E_c$ . The figure is taken from Ref. [12].

enter in a potential well  $V_{bg}$  also referred to as "open channel." Another channel, which is not allowed for the scattering, is referred to as a "closed channel." This channel is coupled to the open channel. Using a magnetic (or optical) external potential  $B$ , the bound state in the closed channel can be brought near the zero-energy level where the scattering events usually occur in ultracold temperatures. Then, the channels enter resonance even when they are weakly coupled. This results in an altered scattering length:

$$a_s = a_0 \left( 1 - \frac{w}{B - B_0} \right), \quad (1.4)$$

where  $a_0$  is the non-resonant scattering length,  $w$  is the width of the resonance, and  $B_0$  is the resonant magnetic field. By varying  $B$  or  $w$ , one may change not only the strength of the interaction but also whether if the interaction is attractive ( $a_s < 0$ ) or repulsive ( $a_s > 0$ ). The qualitative BCS-BEC crossover spectrum in Fig. 1.1 is realized by utilizing the Feshbach resonances.

## Chapter 2

# BCS superconductivity

The key aspect for the superconductivity is the existence of the pairing gap  $\Delta$ . Below the critical temperature, an attractive interaction between particles causes them to form correlated pairs known as Cooper pairs. No matter how weak the attraction is, this pairing creates a gap in the density of states around the Fermi energy leading to a condensed state of matter.

In a free Fermi gas, the particles occupy the energy levels according to their statistics described by the Fermi–Dirac distribution  $f_k = \frac{1}{1+e^{(\varepsilon_k-\mu)/k_B T}}$ , where  $\mu$  is the chemical potential,  $T$  is the temperature,  $k_B$  is the Boltzmann constant, and  $\varepsilon_k$  is the single-particle energy. Since fermions are forbidden to occupy the same quantum state, they fill the momentum space up to a certain level related to the total density of the gas called the Fermi level. In zero temperature, the maximum energy that a particle can have in a ground state is the Fermi energy  $\varepsilon_F = \frac{\hbar^2}{2m}k_F^2$  where  $k_F = (3\pi^2 n)^{\frac{1}{3}}$  is the Fermi wave vector in 3D and  $n$  is the particle density of the system.

The source of the attractive interaction between particles depends on the system. However, for conventional superconductivity, the electron–phonon interaction is the most common natural source. In 1950, Frölich showed that the interaction between two electrons mediated by the lattice phonons could be effectively attractive [55]. Later in 1956, Cooper revealed that this interaction might indeed lead to a formation of electron pairs near the Fermi level [56]. More precisely, the attractive interaction is restricted to the electrons in the range of  $|\varepsilon_{\mathbf{k}} - \varepsilon_F| < \hbar\omega_D$  where  $\omega_D$  is the Debye frequency which is a characteristic frequency of phonons. Subsequently, in 1957, Bardeen, Cooper, and Schrieffer (BCS) presented the microscopic theory of superconductivity [11]. This chapter contains a summary of the BCS model and its one particular outcome called the Andreev states, which are essential to follow the original discussions of this thesis. Detailed derivations and pedagogical discussions on the BCS superconductivity can be found in Refs. [57–59].

## 2.1 The BCS model

Let us consider the case where there are two electrons above the Fermi level with the coordinates  $\{\mathbf{r}_1, \sigma_1\}$  and  $\{\mathbf{r}_2, \sigma_2\}$  where  $\mathbf{r}$  is the spatial coordinate and  $\sigma$  is the spin alignment of an electron. The fermionic many-body wave function consisting of identical particles is anti-symmetric as a result of the Pauli principle:

$$\Psi(\mathbf{r}_1, \sigma_1, \mathbf{r}_2, \sigma_2) = -\Psi(\mathbf{r}_2, \sigma_2, \mathbf{r}_1, \sigma_1). \quad (2.1)$$

The conventional choice for the spin wave function is the singlet form for practical reasons (*s*-wave pairing). Since both the spin-singlet wave function and the complete wave function are odd functions, the spatial wave function must be an even function which can be expanded in terms of plane waves:

$$\Psi(\mathbf{r}_1 - \mathbf{r}_2) = \sum_{\mathbf{k}} \phi_{\mathbf{k}} e^{i\mathbf{k} \cdot (\mathbf{r}_1 - \mathbf{r}_2)}, \quad (2.2)$$

where  $\phi_{\mathbf{k}}$  is the probability amplitude to find two particles with the wave vectors  $\mathbf{k}$  and  $-\mathbf{k}$  with opposite spin alignments since the spin properties are initially selected as singlet (see Fig. 2.1). Eq. (2.2) can be inserted into the two-particle time-independent Schrödinger equation:

$$-\frac{\hbar^2}{2m}(\nabla_1^2 + \nabla_2^2)\Psi(\mathbf{r}_1 - \mathbf{r}_2) + V(\mathbf{r}_1, \mathbf{r}_2)\Psi(\mathbf{r}_1 - \mathbf{r}_2) = (E + 2\varepsilon_F)\Psi(\mathbf{r}_1 - \mathbf{r}_2). \quad (2.3)$$

The solution of above equation yields to [57-59]:

$$E = -2\hbar\omega_D e^{\frac{-2}{D(0)V}}. \quad (2.4)$$

Therefore, in the presence of an attractive interaction of any strength, it is favorable for those two electrons to become correlated since this correlation reduces their energy below the Fermi level. In this particular case, the attractive interaction mediated by phonons is meaningful for the thin shell centered around the Fermi energy with the thickness of  $2\hbar\omega_D$ . All the electrons within this shell form Cooper pairs. The formation of pairs results in a gap in the single-particle density of states around the Fermi energy. Thus, provided an attractive interaction between the particles, a free Fermi gas in its normal state is unstable against the formation of Cooper pairs.

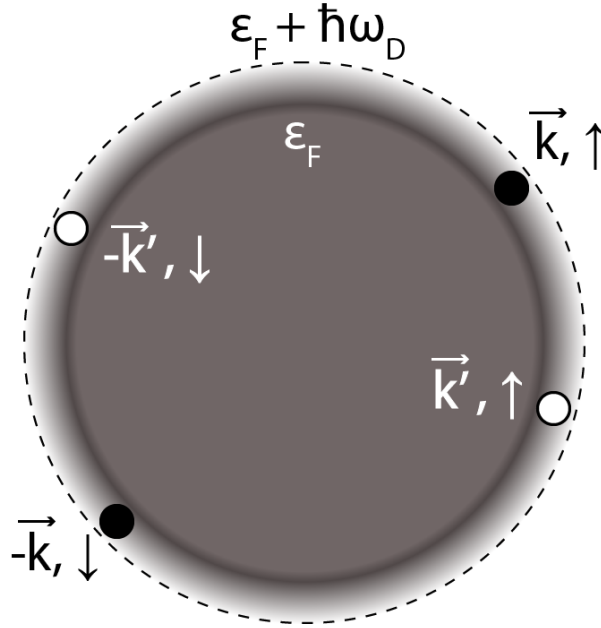


FIGURE 2.1: The interaction considered in the Cooper problem. The particles with momenta and spins  $\{\mathbf{k}, \uparrow\}$  and  $\{-\mathbf{k}, \downarrow\}$  are scattered to  $\{\mathbf{k}', \uparrow\}$  and  $\{-\mathbf{k}', \downarrow\}$  as a result of an attractive interaction.

To consider  $N$  electrons, we treat them in pairs and construct the following many-body wave function:

$$\Psi_N(\mathbf{r}_1, \mathbf{r}_2, \dots, \mathbf{r}_N) = \Psi(\mathbf{r}_1 - \mathbf{r}_2)\Psi(\mathbf{r}_3 - \mathbf{r}_4)\dots\Psi(\mathbf{r}_{N-1} - \mathbf{r}_N). \quad (2.5)$$

An initial remark would be the necessity of having an even number of particles  $N$  to group the electrons in pairs. In the case of having odd  $N$ , the effect of the additional electron is suppressed in the limit of  $N \rightarrow 10^{23}$ . However, in the cases where the  $N$  is relatively small, such as the atomic nuclei, having an odd or even  $N$  plays a vital role [57, 60].

Eq. (2.5) is missing the spin-singlet configuration and anti-symmetric structure. Therefore, it is modified as:

$$\Psi_N(\mathbf{r}_1\sigma_1, \dots, \mathbf{r}_N\sigma_N) = \frac{1}{\sqrt{N!}} \sum_p (-1)^p \Psi(\mathbf{r}_1\sigma_1, \mathbf{r}_2\sigma_2)\dots\Psi(\mathbf{r}_{N-1}\sigma_{N-1}, \mathbf{r}_N\sigma_N), \quad (2.6)$$

where we define a single-pair wave function in spin-singlet state:

$$\Psi(\mathbf{r}_1\sigma_1, \mathbf{r}_2\sigma_2) = \frac{1}{\sqrt{2}} \sum_{\mathbf{k}} \phi_{\mathbf{k}} \left( |\uparrow\downarrow\rangle e^{i\mathbf{k}\cdot(\mathbf{r}_1-\mathbf{r}_2)} - |\downarrow\uparrow\rangle e^{-i\mathbf{k}\cdot(\mathbf{r}_1-\mathbf{r}_2)} \right). \quad (2.7)$$

We change the notation by introducing the annihilation and creation operators. The creation operator  $c_{\mathbf{k}\sigma}^\dagger$  acting on the vacuum state  $|0\rangle$  creates a particle at  $\{\mathbf{k}, \sigma\}$ . The annihilation operator, which is the adjoint of the creation operator, acting on the vacuum has no effect,  $c_{\mathbf{k}\sigma} |0\rangle = |0\rangle$ . Here, the vacuum state represents the Fermi level. The fermionic creation and annihilation operators obey anti-commutation rules:

$$\begin{aligned} \{c_a, c_b^\dagger\} &= c_a c_b^\dagger + c_b^\dagger c_a = \delta_{ab}, \\ \{c_a, c_b\} &= 0, \\ \{c_a^\dagger, c_b^\dagger\} &= 0. \end{aligned} \quad (2.8)$$

Using the creation and annihilation operators Eq. (2.7) can be interpreted as:

$$\Psi = \sum_{\mathbf{k}} \phi_{\mathbf{k}} c_{\mathbf{k}\uparrow}^\dagger c_{-\mathbf{k}\downarrow}^\dagger |0\rangle = \sum_{\mathbf{k}} \phi_{\mathbf{k}} b_{\mathbf{k}}^\dagger |0\rangle. \quad (2.9)$$

where we define  $b_{\mathbf{k}}^\dagger = c_{\mathbf{k}\uparrow}^\dagger c_{-\mathbf{k}\downarrow}^\dagger$  as the spin-singlet pair creation operator. The many-body wave function in Eq. (2.6) can be written as:

$$\Psi_N = \sum_{\mathbf{k}_1, \mathbf{k}_2, \dots, \mathbf{k}_{N/2}} \phi_{\mathbf{k}_1} \phi_{\mathbf{k}_2} \dots \phi_{\mathbf{k}_{N/2}} b_{\mathbf{k}_1}^\dagger b_{\mathbf{k}_2}^\dagger \dots b_{\mathbf{k}_{N/2}}^\dagger |0\rangle. \quad (2.10)$$

At this point, it is clear that Eq. (2.10) is too complicated to deal with. For  $N/2$  pairs there are numerous different values of  $k_i$  which makes it difficult to calculate the amplitudes  $\phi_{k_i}$  for large particle numbers such as  $N \approx 10^{23}$ . Instead, what BCS did was to relax the constraint on having fixed particle numbers and consider the system as a coherent state of the fermion pairs. As it is stated in the Thouless' theorem [61], a  $N$ -body product wave function which is not orthogonal to its vacuum state (such as coherent states) can be described as:

$$|\Psi_{BCS}\rangle = \mathcal{C} e^{\sum_{\mathbf{k}} \phi_{\mathbf{k}} b_{\mathbf{k}}^\dagger} |0\rangle = \mathcal{C} \prod_{\mathbf{k}} e^{\phi_{\mathbf{k}} b_{\mathbf{k}}^\dagger} |0\rangle = \mathcal{C} \prod_{\mathbf{k}} \left( 1 + \phi_{\mathbf{k}} b_{\mathbf{k}}^\dagger \right) |0\rangle, \quad (2.11)$$

where we have used the commutation properties of pair creation operator  $[b_{\mathbf{k}}^\dagger, b_{\mathbf{k}'}^\dagger] = 0$  and  $(b_{\mathbf{k}}^\dagger)^2 = 0$ . To find the normalization constant  $\mathcal{C}$ :

$$\langle \Psi_{BCS} \rangle = \langle 0 | \left( 1 + \phi_{\mathbf{k}}^* b_{\mathbf{k}} \right) \left( 1 + \phi_{\mathbf{k}} b_{\mathbf{k}}^\dagger \right) | 0 \rangle = 1 + |\phi_{\mathbf{k}}|^2 = 1. \quad (2.12)$$

Therefore we can write the normalized BCS wave function as:

$$|\Psi_{BCS}\rangle = \prod_{\mathbf{k}} \left( u_{\mathbf{k}} + v_{\mathbf{k}} b_{\mathbf{k}}^\dagger \right) |0\rangle, \quad (2.13)$$

where  $u_{\mathbf{k}}$  and  $v_{\mathbf{k}}$  are called as *BCS parameters*. They are defined as:

$$\begin{aligned} \phi_{\mathbf{k}} &= \frac{v_{\mathbf{k}}}{u_{\mathbf{k}}}, \\ 1 &= |v_{\mathbf{k}}|^2 + |u_{\mathbf{k}}|^2. \end{aligned} \quad (2.14)$$

Note that we are not working with a system which has fixed particle numbers rather a superposition of different numbers of pairs. Therefore, there is a standard deviation of particle number  $\Delta N = \sqrt{\langle \hat{N}^2 \rangle - \langle \hat{N} \rangle^2}$  where  $\hat{N} = \sum_{\mathbf{k}, \sigma=\uparrow\downarrow} c_{\mathbf{k}\sigma}^\dagger c_{\mathbf{k}\sigma}$  is the particle number operator. However, if the macroscopic value of the number of particles is considered, this deviation is negligible in comparison.

Since  $\phi_{\mathbf{k}}$  has no restriction to be a real number, the BCS wave function can be written in terms of real components of the BCS parameters with a complex phase:

$$|\Psi_{BCS}\rangle = \prod_{\mathbf{k}} \left( |u_{\mathbf{k}}| + |v_{\mathbf{k}}| e^{i\varphi} b_{\mathbf{k}}^\dagger \right) |0\rangle. \quad (2.15)$$

The phase of the BCS wave function  $\varphi$  and the particle number  $N$  are conjugate operators hence there is an uncertainty relation between them:

$$\Delta N \cdot \Delta \varphi \geq \frac{1}{2}. \quad (2.16)$$

Later, we shall see that the phase factor plays a vital role in the transport properties of superconductors. More details on that could be found in Ref. [62].

## 2.2 Mean-field Hamiltonian

In order to model the BCS superfluid, consider the following Hamiltonian:

$$\mathcal{H}_{BCS} = \sum_{\mathbf{k}, \sigma=\uparrow\downarrow} \varepsilon_{\mathbf{k}} c_{\mathbf{k}\sigma}^{\dagger} c_{\mathbf{k}\sigma} - \sum_{\mathbf{k}, \mathbf{l}} V_{\mathbf{k}, \mathbf{l}} c_{\mathbf{k}\uparrow}^{\dagger} c_{-\mathbf{k}\downarrow}^{\dagger} c_{-\mathbf{l}\downarrow} c_{\mathbf{l}\uparrow}. \quad (2.17)$$

The first term contains the kinetic energy of a single particle  $\varepsilon_{\mathbf{k}} = \frac{\hbar^2}{2m} \mathbf{k}^2$  and the second term stands for the scattering of particles with momentum and spin  $\{\mathbf{l}, \uparrow\}$  and  $\{-\mathbf{l}, \downarrow\}$  to  $\{\mathbf{k}, \uparrow\}$  and  $\{-\mathbf{k}, \downarrow\}$ . Therefore, we restrict ourselves to the simple singlet pairing.

We switch to a more general notation:

$$\mathcal{H}_{BCS} = \sum_{\mathbf{k}} \varepsilon_{\mathbf{k}} \left( c_{\mathbf{k}}^{\dagger} c_{\mathbf{k}} + c_{\bar{\mathbf{k}}}^{\dagger} c_{\bar{\mathbf{k}}} \right) - \sum_{\mathbf{k}, \mathbf{l}} V_{\mathbf{k}, \mathbf{l}} c_{\mathbf{k}}^{\dagger} c_{\bar{\mathbf{k}}}^{\dagger} c_{\bar{\mathbf{l}}} c_{\mathbf{l}}, \quad (2.18)$$

where we consider the states  $\{\mathbf{k}, \uparrow\}$  and  $\{-\mathbf{k}, \downarrow\}$  as time-reversed pairs and rename them as  $\mathbf{k}$  and  $\bar{\mathbf{k}}$ .

By describing the BCS wave function as a coherent state (Eq. (2.11)) we have moved to a grand canonical ensemble. Consequently, in order to investigate a system with a certain average particle number we add the constraint on the particle number by using the chemical potential as a Lagrange multiplier:

$$\begin{aligned} \mathcal{H} &= \mathcal{H}_{BCS} - \sum_{\sigma} \mu_{\sigma} \hat{N}_{\sigma}, \\ \mathcal{H} &= \mathcal{H}_{BCS} - \mu_{\mathbf{k}} c_{\mathbf{k}}^{\dagger} c_{\mathbf{k}} - \mu_{\bar{\mathbf{k}}} c_{\bar{\mathbf{k}}}^{\dagger} c_{\bar{\mathbf{k}}}, \\ \mathcal{H} &= \sum_{\mathbf{k}} \left( h_{\mathbf{k}} c_{\mathbf{k}}^{\dagger} c_{\mathbf{k}} + h_{\bar{\mathbf{k}}} c_{\bar{\mathbf{k}}}^{\dagger} c_{\bar{\mathbf{k}}} \right) - \sum_{\mathbf{k}, \mathbf{l}} V_{\mathbf{k}, \mathbf{l}} c_{\mathbf{k}}^{\dagger} c_{\bar{\mathbf{k}}}^{\dagger} c_{\bar{\mathbf{l}}} c_{\mathbf{l}}, \end{aligned} \quad (2.19)$$

where  $h_{\mathbf{k}} = \varepsilon_{\mathbf{k}} - \mu_{\mathbf{k}}$ . Using different chemical potentials for different spin components makes it possible to have an unequal number of particles in the system. For the ground state of the BCS superfluid, all particles should be paired; therefore,  $\mu_{\mathbf{k}} = \mu_{\bar{\mathbf{k}}}$ . However, the excited configurations of this system may be obtained by spin imbalance.

The interaction term in Eq. (2.19) is quite demanding to deal with. To simplify, we use the fact that the system is at the thermodynamic limit; therefore, the fluctuations of an observable around its average value can be disregarded. To implement this, we rewrite the following operator as:

$$\begin{aligned}
c_{\mathbf{k}}^{\dagger}c_{\bar{\mathbf{k}}}^{\dagger} &= \langle c_{\mathbf{k}}^{\dagger}c_{\bar{\mathbf{k}}}^{\dagger} \rangle + c_{\mathbf{k}}^{\dagger}c_{\bar{\mathbf{k}}}^{\dagger} - \langle c_{\mathbf{k}}^{\dagger}c_{\bar{\mathbf{k}}}^{\dagger} \rangle, \\
c_{\mathbf{k}}^{\dagger}c_{\bar{\mathbf{k}}}^{\dagger} &= \langle c_{\mathbf{k}}^{\dagger}c_{\bar{\mathbf{k}}}^{\dagger} \rangle + \delta c_{\mathbf{k}}.
\end{aligned}
\tag{2.20}$$

Here  $\langle c_{\mathbf{k}}^{\dagger}c_{\bar{\mathbf{k}}}^{\dagger} \rangle$  is the expectation value of the operator  $c_{\mathbf{k}}^{\dagger}c_{\bar{\mathbf{k}}}^{\dagger}$  and  $\delta c_{\mathbf{k}}$  is the fluctuation around this expectation value. Now, we rewrite Eq. (2.19) with disregarding the small terms such as  $\delta c_{\mathbf{k}}\delta c_{\mathbf{l}}$ :

$$\mathcal{H} = \sum_{\mathbf{k}} \left( h_{\mathbf{k}}c_{\mathbf{k}}^{\dagger}c_{\mathbf{k}} + h_{\bar{\mathbf{k}}}c_{\bar{\mathbf{k}}}^{\dagger}c_{\bar{\mathbf{k}}} + \Delta_{\mathbf{k}}c_{\mathbf{k}}^{\dagger}c_{\bar{\mathbf{k}}}^{\dagger} + \Delta_{\mathbf{k}}^*c_{\bar{\mathbf{k}}}c_{\mathbf{k}} \right),
\tag{2.21}$$

where

$$\Delta_{\mathbf{k}} = - \sum_{\mathbf{l}} V_{\mathbf{k},\mathbf{l}} \langle c_{\mathbf{l}}c_{\bar{\mathbf{l}}} \rangle
\tag{2.22}$$

is the pairing potential between the time-reversed pairs. Here, it should be noted that the pairing potential is a complex field. It is expressed by its magnitude  $|\Delta|$ , and its complex phase  $\varphi$ :

$$\Delta(\mathbf{r}) = |\Delta(\mathbf{r})|e^{i\varphi(\mathbf{r})}.
\tag{2.23}$$

The mean-field approximation allows us to consider the inter-particle interactions as their average value. Despite the simplifications, it gives a clear description of the system, and it is easy to re-implement some of the fluctuations or interaction channels that are ignored.

The last thing to do with the Hamiltonian in Eq. (2.21) is to enforce the anti-commutation rules of the creation and annihilation operators in Eq. (2.8):

$$\begin{aligned}
\mathcal{H} = \frac{1}{2} \sum_{\mathbf{k}} & \left( h_{\mathbf{k}} \left( c_{\mathbf{k}}^{\dagger}c_{\mathbf{k}} - c_{\mathbf{k}}c_{\mathbf{k}}^{\dagger} + 1 \right) + h_{\bar{\mathbf{k}}} \left( c_{\bar{\mathbf{k}}}^{\dagger}c_{\bar{\mathbf{k}}} - c_{\bar{\mathbf{k}}}c_{\bar{\mathbf{k}}}^{\dagger} + 1 \right) \right. \\
& \left. + \Delta_{\mathbf{k}} \left( c_{\mathbf{k}}^{\dagger}c_{\bar{\mathbf{k}}}^{\dagger} - c_{\bar{\mathbf{k}}}^{\dagger}c_{\mathbf{k}}^{\dagger} \right) + \Delta_{\mathbf{k}}^* \left( c_{\bar{\mathbf{k}}}c_{\mathbf{k}} - c_{\mathbf{k}}c_{\bar{\mathbf{k}}} \right) \right).
\end{aligned}
\tag{2.24}$$

It can also be written as:

$$\mathcal{H} = \frac{1}{2} \sum_{\mathbf{k}} \begin{pmatrix} c_{\mathbf{k}}^{\dagger} & c_{\bar{\mathbf{k}}}^{\dagger} & c_{\mathbf{k}} & c_{\bar{\mathbf{k}}} \end{pmatrix} \begin{pmatrix} h_{\mathbf{k}} & 0 & 0 & \Delta_{\mathbf{k}} \\ 0 & h_{\bar{\mathbf{k}}} & -\Delta_{\mathbf{k}} & 0 \\ 0 & -\Delta_{\mathbf{k}}^* & -h_{\mathbf{k}} & 0 \\ \Delta_{\mathbf{k}}^* & 0 & 0 & -h_{\bar{\mathbf{k}}} \end{pmatrix} \begin{pmatrix} c_{\mathbf{k}} \\ c_{\bar{\mathbf{k}}} \\ c_{\mathbf{k}}^{\dagger} \\ c_{\bar{\mathbf{k}}}^{\dagger} \end{pmatrix}, \quad (2.25)$$

where we disregard the constant contributions and only focus on the operator terms. Above Hamiltonian defines a uniform system, where there is no spatial dependence. Since,  $k$  is a good quantum number, the Hamiltonian can be solved separately for each  $k$ . The expectation value of the Hamiltonian in Eq. (2.24) is:

$$\begin{aligned} \langle \mathcal{H} \rangle &= \frac{1}{2} \sum_{\mathbf{k}} \left( h_{\mathbf{k}} (|v_{\mathbf{k}}|^2 - |u_{\mathbf{k}}|^2 + 1) + h_{\bar{\mathbf{k}}} (|v_{\bar{\mathbf{k}}}|^2 - |u_{\bar{\mathbf{k}}}|^2 + 1) \right. \\ &\quad \left. + \Delta_{\mathbf{k}} (v_{\mathbf{k}} u_{\bar{\mathbf{k}}}^* - v_{\bar{\mathbf{k}}} u_{\mathbf{k}}^*) + \Delta_{\mathbf{k}}^* (u_{\bar{\mathbf{k}}} v_{\mathbf{k}}^* - u_{\mathbf{k}} v_{\bar{\mathbf{k}}}^*) \right) = \sum_{\mathbf{k}} E_{\mathbf{k}}. \end{aligned} \quad (2.26)$$

We minimize the Hamiltonian with respect to the BCS parameters:

$$\begin{aligned} \frac{\partial \langle \mathcal{H} \rangle}{\partial u_{\mathbf{k}}^*} + E_{\mathbf{k}} u_{\mathbf{k}} &= 0, & \frac{\partial \langle \mathcal{H} \rangle}{\partial v_{\mathbf{k}}^*} + E_{\mathbf{k}} v_{\mathbf{k}} &= 0, \\ \frac{\partial \langle \mathcal{H} \rangle}{\partial u_{\bar{\mathbf{k}}}^*} + E_{\mathbf{k}} u_{\bar{\mathbf{k}}} &= 0, & \frac{\partial \langle \mathcal{H} \rangle}{\partial v_{\bar{\mathbf{k}}}^*} + E_{\mathbf{k}} v_{\bar{\mathbf{k}}} &= 0, \end{aligned} \quad (2.27)$$

and consequently, because of the diagonal nature of above 4x4 matrix, we obtain two independent matrix equations:

$$\begin{pmatrix} h_{\mathbf{k}} & \Delta_{\mathbf{k}} \\ \Delta_{\mathbf{k}}^* & -h_{\bar{\mathbf{k}}}^* \end{pmatrix} \begin{pmatrix} u_{\mathbf{k}} \\ v_{\bar{\mathbf{k}}} \end{pmatrix} = E_{\mathbf{k}} \begin{pmatrix} u_{\mathbf{k}} \\ v_{\bar{\mathbf{k}}} \end{pmatrix}, \quad (2.28)$$

$$\begin{pmatrix} h_{\bar{\mathbf{k}}} & -\Delta_{\mathbf{k}} \\ -\Delta_{\mathbf{k}}^* & -h_{\mathbf{k}}^* \end{pmatrix} \begin{pmatrix} u_{\bar{\mathbf{k}}} \\ v_{\mathbf{k}} \end{pmatrix} = E_{\mathbf{k}} \begin{pmatrix} u_{\bar{\mathbf{k}}} \\ v_{\mathbf{k}} \end{pmatrix}. \quad (2.29)$$

It is possible to obtain the second equation from the first one (or vice versa) through the following transformation:

$$\begin{aligned}
& \begin{pmatrix} 0 & 1 \\ 1 & 0 \end{pmatrix} \begin{pmatrix} h_{\mathbf{k}} & \Delta_{\mathbf{k}} \\ \Delta_{\mathbf{k}}^* & -h_{\bar{\mathbf{k}}}^* \end{pmatrix} \begin{pmatrix} 1 & 0 \\ 0 & 1 \end{pmatrix} \begin{pmatrix} u_{\mathbf{k}} \\ v_{\bar{\mathbf{k}}} \end{pmatrix} = E_{\mathbf{k}} \begin{pmatrix} 0 & 1 \\ 1 & 0 \end{pmatrix} \begin{pmatrix} u_{\mathbf{k}} \\ v_{\bar{\mathbf{k}}} \end{pmatrix}, \\
& \begin{pmatrix} 0 & 1 \\ 1 & 0 \end{pmatrix} \begin{pmatrix} h_{\mathbf{k}} & \Delta_{\mathbf{k}} \\ \Delta_{\mathbf{k}}^* & -h_{\bar{\mathbf{k}}}^* \end{pmatrix} \begin{pmatrix} 0 & 1 \\ 1 & 0 \end{pmatrix} \begin{pmatrix} 0 & 1 \\ 1 & 0 \end{pmatrix} \begin{pmatrix} u_{\mathbf{k}} \\ v_{\bar{\mathbf{k}}} \end{pmatrix} = E_{\mathbf{k}} \begin{pmatrix} 0 & 1 \\ 1 & 0 \end{pmatrix} \begin{pmatrix} u_{\mathbf{k}} \\ v_{\bar{\mathbf{k}}} \end{pmatrix}, \\
& \begin{pmatrix} h_{\bar{\mathbf{k}}} & -\Delta_{\mathbf{k}} \\ -\Delta_{\mathbf{k}}^* & -h_{\bar{\mathbf{k}}}^* \end{pmatrix} \begin{pmatrix} v_{\bar{\mathbf{k}}}^* \\ u_{\mathbf{k}}^* \end{pmatrix} = -E_{\mathbf{k}} \begin{pmatrix} v_{\bar{\mathbf{k}}}^* \\ u_{\mathbf{k}}^* \end{pmatrix}. \tag{2.30}
\end{aligned}$$

Therefore, we can calculate Eq. (2.28) and Eq. (2.29) might be easily solved using the transformation  $\{v_{\mathbf{k}}, u_{\bar{\mathbf{k}}}, E_{\mathbf{k}}\} \rightarrow \{u_{\mathbf{k}}^*, v_{\bar{\mathbf{k}}}^*, -E_{\mathbf{k}}\}$ .

### The BCS ground state

The single-particle potentials,  $h_{\mathbf{k}}$ , and  $h_{\bar{\mathbf{k}}}$  are different by the chemical potential term they have. To investigate the BCS ground state, we must have an equal number of particles for  $k$  and  $\bar{\mathbf{k}}$ , making  $h_{\mathbf{k}} = h_{\bar{\mathbf{k}}}$ . Solving the eigenvalue problem at Eq. (2.28) we get the eigenvalues:

$$E_{\mathbf{k}} = \pm \sqrt{(\varepsilon_{\mathbf{k}} - \mu)^2 + |\Delta|^2}, \tag{2.31}$$

and the BCS parameters:

$$\begin{aligned}
|u_{\mathbf{k}}|^2 &= \frac{1}{2} \left( 1 + \frac{\varepsilon_{\mathbf{k}} - \mu}{E_{\mathbf{k}}} \right), \\
|v_{\bar{\mathbf{k}}}|^2 &= \frac{1}{2} \left( 1 - \frac{\varepsilon_{\mathbf{k}} - \mu}{E_{\mathbf{k}}} \right), \\
u_{\mathbf{k}} v_{\bar{\mathbf{k}}}^* &= \frac{\Delta}{2E_{\mathbf{k}}}. \tag{2.32}
\end{aligned}$$

It is easy to see that in the case of no pairing  $\Delta = 0$ , the above equations describe the free Fermi gas where the energy of a quantum state is described by its kinetic energy relative to the chemical potential,  $E_{\mathbf{k}} = \pm (\varepsilon_{\mathbf{k}} - \mu)$ . The energies below the Fermi level describe the Fermi sea occupied by particles,  $|v_{\bar{\mathbf{k}}}|^2 = 1$  and the energies with positive values represent the hole states unoccupied by the particles above the Fermi level,  $|u_{\mathbf{k}}|^2 = 1$ . The existence of the pairing gap creates coherence between particle and hole states, allowing us to treat electron-hole pairs as *quasi-particles* (see Fig. 2.2).

The other limiting case where  $\varepsilon_{\mathbf{k}} = \mu$ , we have  $E_{\mathbf{k}} = \pm|\Delta|$ . Here we see that the pairing term plays a role of an effective barrier, setting a minimum energy cost of  $2|\Delta|$  to excite the ground state.

As stated in Eq. (2.30), the time-reversed solutions can be obtained by a simple transformation. Additionally, the self-consistency condition for the pairing field can be obtained with Eq. (2.22) and Eq. (2.32):

$$1 = \frac{V}{2} \sum_{\mathbf{k}} \frac{1}{\sqrt{(\varepsilon_{\mathbf{k}} - \mu)^2 - |\Delta|^2}}. \quad (2.33)$$

It is possible to convert the above summation into an integration:

$$1 = \frac{D(0)V}{2} \int_0^{\hbar\omega_D} \frac{dh}{\sqrt{h^2 - |\Delta|^2}}. \quad (2.34)$$

In the limit of weak pairing,  $\hbar\omega_D \gg \Delta$ , this integral gives:

$$\Delta = 2\hbar\omega_D e^{-\frac{1}{D(0)V}}. \quad (2.35)$$

Notice that this relation is similar to the energy of the bound state in Eq. (2.4). Another remark is that we have defined our Hamiltonian in its simplest form. We did not include a spin-orbit term in the mean-field description in Eq. (2.20) where the additional term  $c_{\mathbf{k}\uparrow}^\dagger c_{\mathbf{k}\downarrow}$  is needed. Moreover, we have only limited our case to singlet-pairing, where the pairing occurs between time-reversed pairs, Eq. (2.22). A more general Hamiltonian than Eq. (2.25) would be written as:

$$H = \begin{pmatrix} h_{\uparrow\uparrow}(\mathbf{k}) & h_{\uparrow\downarrow}(\mathbf{k}) & 0 & \Delta_{\uparrow\downarrow}(\mathbf{k}) \\ h_{\downarrow\uparrow}(\mathbf{k}) & h_{\downarrow\downarrow}(\mathbf{k}) & -\Delta_{\downarrow\uparrow}(\mathbf{k}) & 0 \\ 0 & -\Delta_{\downarrow\uparrow}^*(\mathbf{k}) & -h_{\uparrow\uparrow}^*(\mathbf{k}) & -h_{\uparrow\downarrow}^*(\mathbf{k}) \\ \Delta_{\uparrow\downarrow}^*(\mathbf{k}) & 0 & -h_{\downarrow\uparrow}^*(\mathbf{k}) & -h_{\downarrow\downarrow}^*(\mathbf{k}) \end{pmatrix}. \quad (2.36)$$

The eigenvalue problem of the above Hamiltonian is called the Hartree-Fock Bogoliubov (HFB) problem. The Hartree term stands for the diagonal terms of the single-particle part of the Hamiltonian, while the Fock terms are the off-diagonals. The Bogoliubov terms are the contribution coming from the spin-singlet pairing. In more exotic cases, such as p-wave pairing, where spin-triplet channels are active, the off-diagonals of the pairing sector of above Hamiltonian would acquire non-zero values. We consider neither a spin-orbit case nor triplet pairing throughout this work, so we

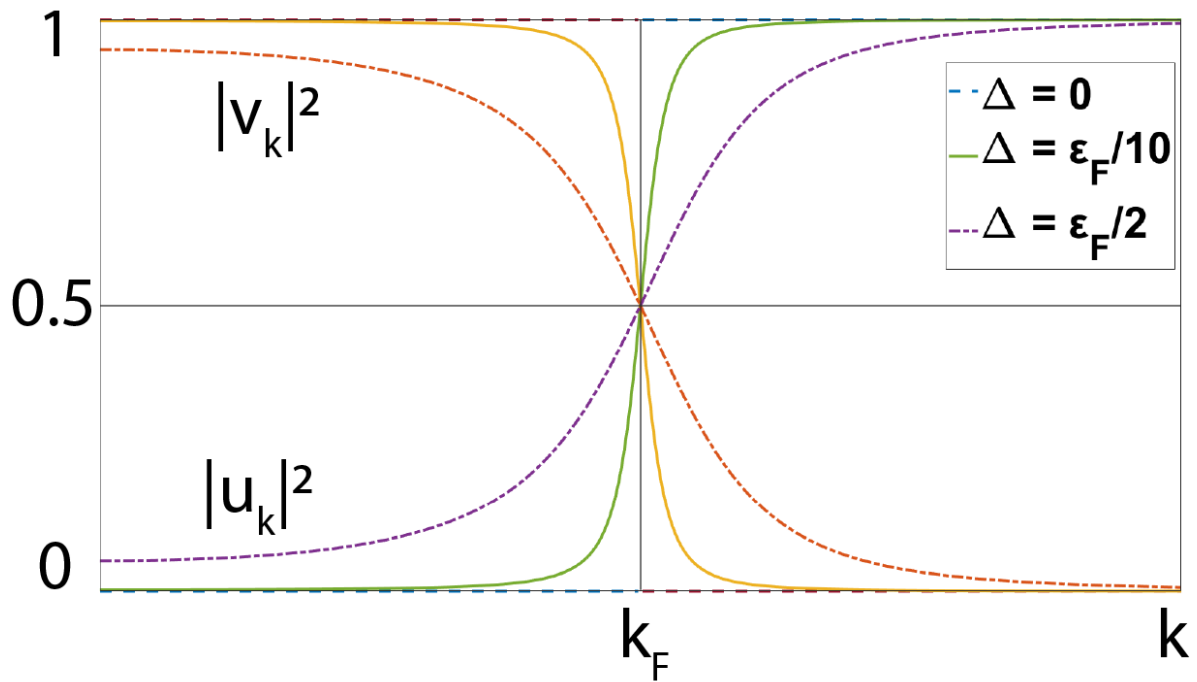


FIGURE 2.2: The occupations of energy levels according to BCS model. It can be seen that for  $\Delta = 0$ , the levels below the Fermi level are completely occupied by particles ( $|v_k|^2$ ) whereas the levels above the Fermi level are completely occupied by holes ( $|u_k|^2$ ). When  $\Delta \neq 0$ , the particle and hole states mix.

stick to the Hamiltonian of the form Eq. (2.25), which is called the Bogoliubov–de Gennes (BdG) framework. Even though it has a more straightforward form, it is still tedious to deal with its excited states. In the next section, to study the excited states, we will describe a canonical transformation to handle the complications elegantly.

## 2.3 The Bogoliubov transformation

As shown in the previous section, the BCS Hamiltonian has both positive and negative energy solutions,  $E_k$  and  $-E_k$ . The two eigenvectors corresponding to these energies are respectively  $\begin{pmatrix} u_{\mathbf{k}} \\ v_{\bar{\mathbf{k}}} \end{pmatrix}$  and  $\begin{pmatrix} -v_{\mathbf{k}}^* \\ u_{\mathbf{k}}^* \end{pmatrix}$ . From these eigenvectors we define a unitary matrix,  $\mathcal{W}$ , which will diagonalize the BCS Hamiltonian in the following way:

$$\mathcal{W}^\dagger H \mathcal{W} = \begin{pmatrix} u_{\mathbf{k}}^* & v_{\bar{\mathbf{k}}}^* \\ -v_{\bar{\mathbf{k}}} & u_{\mathbf{k}} \end{pmatrix} \begin{pmatrix} h_{\mathbf{k}} & \Delta_{\mathbf{k}} \\ \Delta_{\mathbf{k}}^* & -h_{\bar{\mathbf{k}}}^* \end{pmatrix} \begin{pmatrix} u_{\mathbf{k}} & -v_{\bar{\mathbf{k}}}^* \\ v_{\bar{\mathbf{k}}} & u_{\mathbf{k}}^* \end{pmatrix} = \begin{pmatrix} E_{\mathbf{k}} & 0 \\ 0 & -E_{\mathbf{k}} \end{pmatrix}. \quad (2.37)$$

Therefore,

$$\mathcal{H} = \sum_{\mathbf{k}} \begin{pmatrix} c_{\mathbf{k}}^\dagger & c_{\bar{\mathbf{k}}} \end{pmatrix} \mathcal{W} \begin{pmatrix} E_{\mathbf{k}} & 0 \\ 0 & -E_{\mathbf{k}} \end{pmatrix} \mathcal{W}^\dagger \begin{pmatrix} c_{\mathbf{k}} \\ c_{\bar{\mathbf{k}}}^\dagger \end{pmatrix}. \quad (2.38)$$

Here, we can define new particle annihilation and creation operators which is a linear combination of particle and hole operators:

$$\begin{aligned} \gamma_{\mathbf{k}} &= u_{\mathbf{k}}^* c_{\mathbf{k}} - v_{\bar{\mathbf{k}}}^* c_{\bar{\mathbf{k}}}^\dagger, \\ \gamma_{\bar{\mathbf{k}}}^\dagger &= u_{\bar{\mathbf{k}}} c_{\bar{\mathbf{k}}}^\dagger + v_{\mathbf{k}} c_{\mathbf{k}}, \end{aligned} \quad (2.39)$$

and write the Hamiltonian in a simplified way:

$$\mathcal{H} = \sum_{\mathbf{k}} E_{\mathbf{k}} \left( \gamma_{\mathbf{k}}^\dagger \gamma_{\mathbf{k}} + \gamma_{\bar{\mathbf{k}}}^\dagger \gamma_{\bar{\mathbf{k}}} \right). \quad (2.40)$$

The quasi-particle operators in Eq. (2.39) obey fermionic anti-commutation rules at Eq. (2.8). As we have pointed out in the previous section, the particle and hole states in a paired system do correlate. The Bogoliubov transformation, while diagonalizing the Hamiltonian, provides us a new quasi-particle description for these correlated particle and hole states by considering them as a linear combination of both.

The BCS ground state given in Eq. (2.13) is the vacuum for these quasi-particle operators as one can see from:

$$\gamma_{\mathbf{k}} |\Psi_{BCS}\rangle = 0. \quad (2.41)$$

Therefore, using the Bogoliubov operators, we can construct quasi-particle excitations from a fully paired ground state. Although various sources may cause these excitations, in this study, we focus mainly on two types of excitations: 1) An excitation in the whole system that is caused by the finite temperature. 2) Excited quasi-particle states caused by spin-imbalance,  $N_{\uparrow} \neq N_{\downarrow}$ , in other words a chemical potential difference between the spin components  $\mu_{\mathbf{k}} \neq \mu_{\bar{\mathbf{k}}}$ .

### 2.3.1 The BCS critical temperature

So far, we have considered the system in the limit of zero temperature, neglecting thermal fluctuations. For this reason the expectation of the number operator for Bogoliubov quasi-particles yields to zero,  $\langle \gamma_{\mathbf{k}}^{\dagger} \gamma_{\mathbf{k}} \rangle = 0$ . When a finite temperature is introduced to the system, there is a finite probability to find:

$$\begin{aligned} \langle \gamma_{\mathbf{k}}^{\dagger} \gamma_{\mathbf{k}} \rangle &= f(k), \\ \langle \gamma_{\mathbf{k}} \gamma_{\mathbf{k}}^{\dagger} \rangle &= 1 - f(k), \end{aligned} \quad (2.42)$$

where the probability  $f_k$  is a function of temperature. Repeating the calculations from the previous section for the finite temperature, we find that the gap equation in Eq. (2.22) is modified as:

$$\Delta_{\mathbf{k}} = - \sum_{\mathbf{l}} V_{\mathbf{kl}} u_{\mathbf{l}}^* v_{\mathbf{l}} (1 - 2f(l)). \quad (2.43)$$

Since the probability of  $f(k)$  has a value between 0 and 1, the introduction of the finite temperature diminishes the strength of the pairing field. The probability function  $f(k)$  is the Fermi-Dirac function describing thermal excitations. It can be obtained by minimizing the free energy. The free energy is:

$$\mathcal{F} = \langle \mathcal{H} \rangle - TS, \quad (2.44)$$

$$\begin{aligned} \mathcal{F} &= \sum_{\mathbf{k}} h_{\mathbf{k}} \left( f(k) |u_{\mathbf{k}}|^2 + (1 - f(k)) |v_{\mathbf{k}}|^2 \right) - \Delta \sum_{\mathbf{k}} ((1 - 2f(k)) v_{\mathbf{k}} u_{\mathbf{k}}^*) \\ &+ 2k_B T \sum_{\mathbf{k}} (f(k) \ln f(k) + (1 - f(k)) \ln(1 - f(k))). \end{aligned} \quad (2.45)$$

where  $S$  is the entropy and we have considered simple case of  $V_{\mathbf{k}\mathbf{l}} = V$  and  $\Delta_{\mathbf{k}} = \Delta_{\mathbf{l}} = \Delta$ . The minimization of the free energy with respect to  $f(k)$  gives the Fermi–Dirac distribution:

$$\frac{\partial \mathcal{F}}{\partial f(k)} = 0, \quad (2.46)$$

$$f(k) = \frac{1}{1 + e^{E_{\mathbf{k}} \beta}}, \quad (2.47)$$

where  $\beta = (k_B T)^{-1}$  is the inverse temperature. Rewriting Eq. (2.43):

$$1 = \frac{V}{2} \sum_{\mathbf{k}} \frac{\tanh(\sqrt{h^2 + \Delta^2}/2k_B T)}{\sqrt{h^2 + \Delta^2}}, \quad (2.48)$$

is the self consistency condition under the effect of finite temperature. In the limit of zero temperature, we obtain Eq. (2.35). We are interested in the critical temperature limit ( $T \rightarrow T_c$ ) where the pairing field suppose to vanish. Above summation can be written in integral form as the following:

$$\frac{1}{D(0)V} = \int_0^{\hbar\omega_D} \frac{\tanh(h/2k_B T_c)}{h} dh = \int_0^{\hbar\omega_D/2k_B T_c} \frac{\tanh(x)}{x} dx. \quad (2.49)$$

By integrating the above expression by parts, we get:

$$T_c = \frac{2e^{\gamma_E}}{\pi k_B} \hbar\omega_D e^{-\frac{1}{D(0)V}}, \quad (2.50)$$

where  $\gamma_E \approx 0.577$  is the Euler's constant. Comparing the above equation to Eq. (2.35), we get the critical temperature in BCS model:

$$\frac{\Delta_0}{k_B T_c} = 1.76. \quad (2.51)$$

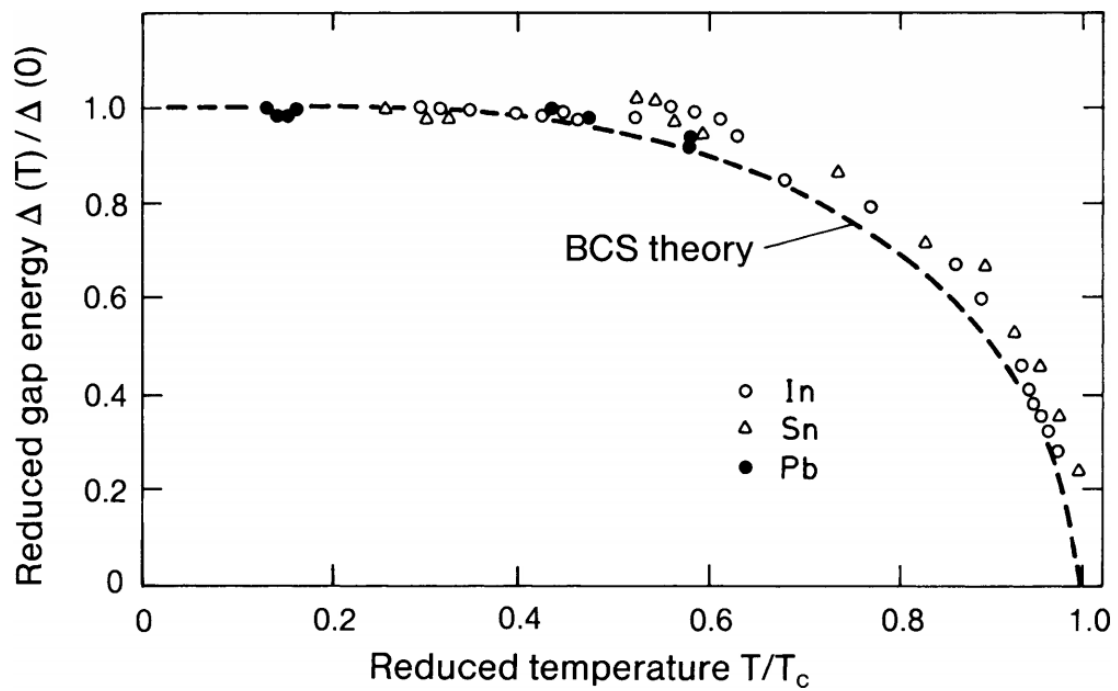


FIGURE 2.3: The behaviour of the magnitude of the pairing field as a function of temperature. The estimation of the BCS theory is compared with experimental results obtained by different superconductors. The figure is taken from Ref. [63].

The above result has been tested numerous times and holds outstanding accuracy [64]. The complete behavior of  $\Delta(T)$  can be described using the gap equation in Eq. (2.48). In the limit of low temperature, the effect of finite temperature on the pairing field is exponentially suppressed,  $e^{-\Delta/k_B T} \approx 0$ . However, for the values near the critical temperature,  $\Delta/\Delta_0 \sim \sqrt{1 - T/T_c}$ . The behavior of the magnitude of the pairing field as a function of temperature can be found at Fig. 2.3.

### 2.3.2 HFB equations in coordinate space

So far, we have discussed the BCS theory in momentum space where the system is assumed to be uniform. To introduce a pairing field or an external potential with spatial dependence, it is suitable to transfer the above methodology from momentum space to coordinate space. To do that, we define the field operators employing Fourier transform:

$$\begin{aligned}\hat{\Psi}_\sigma(\mathbf{r}) &= \sum_{\mathbf{k}} e^{i\mathbf{k}\cdot\mathbf{r}} c_{\sigma\mathbf{k}}, \\ \hat{\Psi}_\sigma^\dagger(\mathbf{r}) &= \sum_{\mathbf{k}} e^{-i\mathbf{k}\cdot\mathbf{r}} c_{\sigma\mathbf{k}}^\dagger.\end{aligned}\quad (2.52)$$

These field operators satisfy the anti-commutation relations in Eq. (2.8). Subsequently, the particle number operator,  $N$  can be defined as:

$$\hat{N} = \sum_\sigma \int d\mathbf{r} \hat{\Psi}_\sigma^\dagger(\mathbf{r}) \hat{\Psi}_\sigma(\mathbf{r}), \quad (2.53)$$

and the Hamiltonian can be rewritten as:

$$\mathcal{H} = \int d\mathbf{r} \sum_\sigma \hat{\Psi}_\sigma^\dagger(\mathbf{r}) \left( \frac{\mathbf{p}^2}{2m} + U(\mathbf{r}) \right) \hat{\Psi}_\sigma(\mathbf{r}) - \int d\mathbf{r} V(\mathbf{r}) \sum_\sigma \hat{\Psi}_\sigma^\dagger(\mathbf{r}) \hat{\Psi}_{\bar{\sigma}}^\dagger(\mathbf{r}) \hat{\Psi}_{\bar{\sigma}}(\mathbf{r}) \hat{\Psi}_\sigma(\mathbf{r}), \quad (2.54)$$

where  $U$  is an arbitrary spatial potential. For convenience, we simply take it  $U(\mathbf{r}) = 0$  unless it is stated otherwise. By diagonalizing the Hamiltonian, we obtain the BCS parameters,  $u$ , and  $v$ . Under finite temperature, utilizing the BCS parameters, we formulate the densities as the following:

$$n_\sigma(\mathbf{r}) = \sum_{|E_{\mathbf{k}}| < E_c} |v_{\mathbf{k},\sigma}(\mathbf{r})|^2 f_\beta(-E_{\mathbf{k}}), \quad (2.55)$$

$$\tau_\sigma(\mathbf{r}) = \sum_{|E_{\mathbf{k}}| < E_c} |\nabla v_{\mathbf{k},\sigma}(\mathbf{r})|^2 f_\beta(-E_{\mathbf{k}}), \quad (2.56)$$

$$\nu(\mathbf{r}) = \sum_{|E_{\mathbf{k}}| < E_c} v_{n,\downarrow}^*(\mathbf{r}) u_{k,\uparrow}(\mathbf{r}) \frac{f_\beta(-E_{\mathbf{k}}) - f_\beta(E_{\mathbf{k}})}{2}, \quad (2.57)$$

$$\mathbf{j}_\sigma(\mathbf{r}) = \sum_{|E_{\mathbf{k}}| < E_c} \text{Im}[v_{\mathbf{k},\sigma}(\mathbf{r}) \nabla v_{\mathbf{k},\sigma}^*(\mathbf{r})] f_\beta(-E_{\mathbf{k}}), \quad (2.58)$$

where  $n_\sigma(\mathbf{r})$  is the number density of spin  $\sigma$ .  $\tau_\sigma(\mathbf{r})$  is denoted as the kinetic density,  $\nu(\mathbf{r})$  is the anomalous density and  $\mathbf{j}_\sigma(\mathbf{r})$  is the current density. We introduce an energy cut-off,  $E_c$ , to avoid the divergence of kinetic and anomalous densities,  $\nu(\mathbf{r}, \mathbf{r}') \sim 1/|\mathbf{r} - \mathbf{r}'|$ . Finally, the energy density can be expressed as:

$$\mathcal{E}_{BdG} = \frac{\tau_\uparrow + \tau_\downarrow}{2} + g_{\text{eff}} \nu^\dagger \nu, \quad (2.59)$$

where  $g_{\text{eff}}$  is the effective coupling constant,  $\Delta(\mathbf{r}) = -g_{\text{eff}} \nu(\mathbf{r})$ .

## 2.4 Andreev bound states

Up to this point, we have only considered a pairing field that is uniform in coordinate space. But what happens at the edge of the superconductor?

An important length scale for superconductors (and superfluids) is the coherence length:

$$\xi = \frac{\varepsilon_F}{k_F \Delta}, \quad (2.60)$$

In detail, the coherence length is the approximate distance between the Cooper pairs; the more potent the pairing, the tighter the pairs. Moreover, the quasi-particle wave function can not end abruptly at the edge of the superconductor; it has to be continuous. Therefore, the scale in which the pairing vanishes smoothly at the edge is also described by the coherence length [62]. In neighboring normal and superconducting metals, the particle-hole correlations inside the superconductor may leak inside the

normal metal. The proximity effect does not transform the normal metal into a superconductor, but the coherence between the particle and hole states may yet survive up to the coherence length.

Let us consider a system divided into two parts, a normal metal in contact with a superconductor. Since there is an energy gap in the superconductor, quasi-particles below the pairing gap can not penetrate the superconductor because there are no allowed levels for particles to occupy. To investigate the junction, we refer to BdG equations:

$$\begin{pmatrix} H_0 & \Delta(\mathbf{r}) \\ \Delta^*(\mathbf{r}) & -H_0 \end{pmatrix} \begin{pmatrix} u(\mathbf{r}) \\ v(\mathbf{r}) \end{pmatrix} = E \begin{pmatrix} u(\mathbf{r}) \\ v(\mathbf{r}) \end{pmatrix}, \quad (2.61)$$

where pairing is defined as a step-like function,  $\Delta(\mathbf{r}) = \theta(x)\Delta_0 e^{i\varphi}$  and  $H_0 = -\frac{\hbar}{2m}\nabla^2 - \mu$  is the single particle Hamiltonian. We set  $\hbar = m = 1$ . We assume no potential barrier between the two parts, so there is no elastic scattering at the boundary. Furthermore, we take a uniform superconductor where  $\Delta(\mathbf{r})$  is smooth and changes slowly with respect to mean inter-particle distance. This assumption implies a coherence length much larger than lattice spacing,  $\xi \gg k_F^{-1}$ . In other words, the strength of the pairing field is much smaller than the Fermi energy,  $|\Delta| \ll \varepsilon_F$ . As a result of this assumption, it is possible to separate the BdG parameters  $u$  and  $v$  into slowly and rapidly varying parts,

$$u(\mathbf{r}) = \tilde{u}(\mathbf{r}) e^{ik_F \hat{n} \cdot \mathbf{r}}, \quad (2.62)$$

$$v(\mathbf{r}) = \tilde{v}(\mathbf{r}) e^{ik_F \hat{n} \cdot \mathbf{r}}. \quad (2.63)$$

Using Eq. (2.62) and Eq. (2.63) in Eq. (2.61) gives,

$$-\nabla^2 \tilde{u}(\mathbf{r}) - ik_F \nabla \tilde{u}(\mathbf{r}) + \Delta \tilde{v}(\mathbf{r}) = E \tilde{u}(\mathbf{r}), \quad (2.64)$$

$$\nabla^2 \tilde{v}(\mathbf{r}) + ik_F \nabla \tilde{v}(\mathbf{r}) + \Delta^* \tilde{u}(\mathbf{r}) = E \tilde{v}(\mathbf{r}). \quad (2.65)$$

Recalling the above assumption about the smoothness of  $\tilde{u}(\mathbf{r})$ , the term  $\nabla^2 \tilde{u}(\mathbf{r})$  will be non-significant with respect to  $ik_F \nabla \tilde{u}(\mathbf{r})$ . As a result, we obtain:

$$\begin{pmatrix} -ik_F \nabla & \Delta(\mathbf{r}) \\ \Delta^*(\mathbf{r}) & ik_F \nabla \end{pmatrix} \begin{pmatrix} \tilde{u}(\mathbf{r}) \\ \tilde{v}(\mathbf{r}) \end{pmatrix} = E \begin{pmatrix} \tilde{u}(\mathbf{r}) \\ \tilde{v}(\mathbf{r}) \end{pmatrix}. \quad (2.66)$$

Using *Andreev approximation*, the differential equations are reduced from second order to first order, which greatly simplifies the analytic examination. We now turn

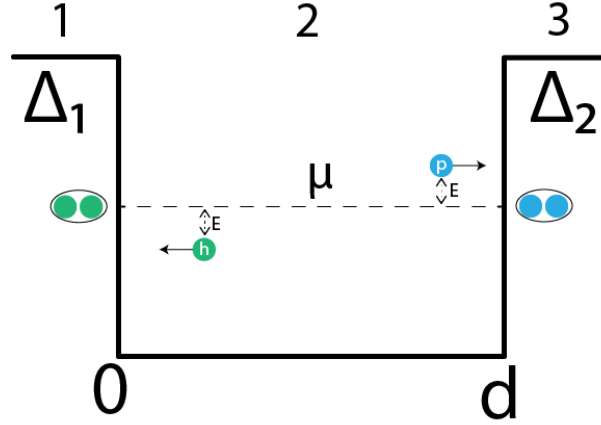


FIGURE 2.4: The SNS junction. The regions 1 and 3 are superconductors and the region 2 is the normal part in between. The particle with the energy  $E$  reflects as a hole having the energy  $-E$  (relative to the Fermi level). As a result a Cooper pair nucleates inside the superconductor.

our focus on a system consisting of a superconductor - normal - superconductor (SNS) junction, Fig. 2.4. For simplicity, the pairing well can be considered only in one dimension. As a result, contributions to the wave-function from other dimensions are simply plane waves,  $\Psi(x, y, z) = \Psi(x)e^{ik_y y}e^{ik_z z}$ . Furthermore, there are different solutions in each region of the junction. These solutions should satisfy the boundary conditions at  $x = 0$  and  $x = d$ .

In the normal part,  $\Delta = 0$ . Hence, we have:

$$\begin{pmatrix} -ik_F \frac{d}{dx} & 0 \\ 0 & ik_F \frac{d}{dx} \end{pmatrix} \begin{pmatrix} \tilde{u}(\mathbf{x}) \\ \tilde{v}(\mathbf{x}) \end{pmatrix} = E \begin{pmatrix} \tilde{u}(\mathbf{x}) \\ \tilde{v}(\mathbf{x}) \end{pmatrix}, \quad (2.67)$$

and the wavefunction is:

$$\Psi_2(x) = \begin{pmatrix} u_2 e^{i\frac{E}{k_F}x} \\ v_2 e^{-i\frac{E}{k_F}x} \end{pmatrix}. \quad (2.68)$$

In the superconductor regime, given the pairing field changes smoothly, the BCS parameters can be expanded in the following way:

$$\begin{aligned} \tilde{u}(\mathbf{x}) &= f e^{iqx}, \\ \tilde{v}(\mathbf{x}) &= g e^{iqx}. \end{aligned} \quad (2.69)$$

The first and the third regions differ by their pairing terms. Here they are assumed

that they have the same pairing strength,  $|\Delta_1| = |\Delta_2| = |\Delta|$  but their phases are unconstrained. The new BCS parameters are denoted as  $f_i$  and  $g_i$  where the index shows the region from Fig. 2.4. Using the Eq. (2.66) the following expressions are obtained:

$$\begin{aligned} k_F q f_i + \Delta g_i &= E f_i, \\ -k_F q g_i + \Delta^* f_i &= E g_i, \end{aligned} \quad (2.70)$$

with,

$$q^2 = \frac{E^2 - |\Delta|^2}{k_F^2}. \quad (2.71)$$

In the sub-gap regime where  $E < |\Delta|^2$  the wave-vector  $q$  is:

$$q = \pm i \frac{\sqrt{|\Delta|^2 - E^2}}{k_F} = \pm i p. \quad (2.72)$$

This means below gap energies the wave-functions in the superconducting region are evanescent. The single-particle solutions decay as they go further into the bulk of the superconductor. The wave functions are:

$$\Psi_2(x) = \begin{pmatrix} u(x) \\ v(x) \end{pmatrix} = \begin{pmatrix} \tilde{u}(x) e^{i k_F x} \\ \tilde{v}(x) e^{i k_F x} \end{pmatrix}, \quad (2.73)$$

$$\Psi_1(x) = \begin{pmatrix} f_1 e^{p x} e^{i k_F x} \\ g_1 e^{p x} e^{i k_F x} \end{pmatrix}, \quad (2.74)$$

$$\Psi_3(x) = \begin{pmatrix} f_3 e^{-p x} e^{i k_F x} \\ g_3 e^{-p x} e^{i k_F x} \end{pmatrix}. \quad (2.75)$$

The solutions must be continuous at the boundaries. Hence, the application of the boundary conditions gives the Andreev levels:

$$\begin{aligned} \Psi_1(0) &= \Psi_2(0), \\ \begin{pmatrix} u_2 \\ v_2 \end{pmatrix} &= \begin{pmatrix} f_1 \\ g_1 \end{pmatrix}, \end{aligned} \quad (2.76)$$

and

$$\begin{aligned}\Psi_2(d) &= \Psi_3(d), \\ \frac{g_3 f_1}{g_1 f_3} &= e^{-i \frac{E}{k_F} d}.\end{aligned}\quad (2.77)$$

Using the Eq. (2.70),

$$\begin{aligned}f_1 &= \frac{\Delta_1}{E + ik_F p} g_1, \\ f_3 &= \frac{\Delta_3}{E - ik_F p} g_3,\end{aligned}\quad (2.78)$$

resulting,

$$\frac{E - ik_F p}{E + ik_F p} e^{i\delta\varphi} = e^{-i \frac{E}{k_F} d} \quad (2.79)$$

where  $\delta\varphi = \varphi_1 - \varphi_2$  is the phase difference between two superconducting regions. Above equation can be written in a simpler way with the following trick:

$$\begin{aligned}\theta &= \arccos \frac{E}{|\Delta|}, \\ r e^{i\theta} &= E + i \sqrt{|\Delta|^2 - E^2}.\end{aligned}\quad (2.80)$$

Finally, the Andreev levels are obtained as:

$$\frac{E_n}{k_F} d - 2 \arccos \frac{E_n}{|\Delta|} + \delta\varphi = 2\pi n. \quad (2.81)$$

It is also possible to rewrite Eq. (2.81) using  $\xi = \varepsilon_F / (k_F \Delta)$ :

$$\frac{E_n}{|\Delta|} \frac{d}{2\xi} - 2 \arccos \frac{E_n}{|\Delta|} + \delta\varphi = 2\pi n. \quad (2.82)$$

As we have seen in Eq. (2.71), for energies below the pairing gap, the wave-function decays inside the superconductor. However, Eq. (2.82) describes bound states inside the normal metal. The energy of the states inside the normal metal explicitly depends on the phase difference between the superconductors. In the special case of  $\delta\varphi = \pi$ , we see that the result is trivial,  $E = 0$ . Here, it should be noted that the energies are relative to the Fermi energy. Eq. (2.73) describes the bound states inside the normal part of the junction. It can be rewritten as:

$$\Psi_2(x) = \begin{pmatrix} u_2 e^{i(k_F + \frac{E}{k_F})x} \\ v_2 e^{i(k_F - \frac{E}{k_F})x} \end{pmatrix}. \quad (2.83)$$

The BCS parameters  $u$  and  $v$  can be found from Eq. (2.76):

$$\frac{u_2}{v_2} = \frac{\Delta}{E + i\sqrt{|\Delta|^2 - E^2}}. \quad (2.84)$$

The normalization of Eq. (2.83) brings the condition  $|u_2|^2 + |v_2|^2 = 1$ . Therefore, it can be found that the occupation of Andreev levels are:

$$|u_2|^2 = |v_2|^2 = \frac{1}{2}. \quad (2.85)$$

The Andreev states are the results of the continuity of the quasi-particle wave function. The pairing field from each superconductor leak into the normal regime instead of ending abruptly at the boundary. However, this leak does not convert the normal metal into a superconductor, but it introduces the particle-hole correlation to the normal metal. When a thin layer of normal metal is between two superconductors, the particle-hole correlation leads to Andreev states. Eq. (2.85) shows that the Andreev states are occupied by half of a spin-up particle and half of a spin-down hole.

Eq. (2.83) shows that a particle incoming to the superconducting boundary reflects back as a hole. The incoming particle has the momentum  $q_+ = k_F + E/k_F$ . Therefore, the incoming wave-packet has the group velocity  $v_g = k_F$ . The outgoing (reflected) hole has the momentum  $q_- = k_F - E/k_F$  resulting the group velocity  $v_g = -k_F$ . This reflection is different than the ordinary reflection where the particle with the velocity  $v_p = \{v_x, v_y\}$  would reflect back as a particle with the velocity  $v_p = \{-v_x, v_y\}$ . In the case we are considering, the particle is converted to a hole with the velocity  $v_h = \{-v_x, -v_y\}$ . This kind of reflection is called as *retro-reflection* which is a result of particle-hole conversion.

## Chapter 3

# Modeling method and the numerical framework

Two distinguished methods to simulate the many-body quantum state are the Density Functional Theory (DFT) and the Quantum Monte-Carlo (QMC) method. The integrity of QMC has been tested over many years [21, 65–67]. It is a reliable tool to capture the ground-state and thermodynamic properties of the ultracold Fermi gas. However, when it comes to the excited states, such as the spin-imbalanced scenario, it breaks down. QMC is also computationally demanding when it comes to simulating large systems where particle number is on the order of a couple of thousands. In order to examine the spin-imbalanced ultracold Fermi gas and its dynamics, DFT is proven to be a reliable method [68].

### 3.1 Density functional theory

DFT relies on two theorems called Hohenberg-Kohn theorems, which was originally published in 1964 [69]. The first Hohenberg-Kohn theorem states that the external potential  $V_{\text{ext}}$  acting on a system composed of many fermions is a unique functional of the particle density. Since the kinetic energy  $T$  and the interaction between the particles  $V$  are also functionals of the density, the energy of the many-body fermionic system can be written as:

$$E[n(\mathbf{r})] = F[n(\mathbf{r})] + \int V_{\text{ext}}(\mathbf{r})n(\mathbf{r})d\mathbf{r}, \quad (3.1)$$

where  $F[n(\mathbf{r})] = T[n(\mathbf{r})] + V[n(\mathbf{r})]$ , and  $n(\mathbf{r}) = \langle \Psi(r) \rangle$  is the particle density. The uniqueness of the  $V_{\text{ext}}$  can be shown by taking two different external potentials  $V_{\text{ext}}$ , and  $V'_{\text{ext}}$ . These different potentials result to Hamiltonians  $\mathcal{H}$ ,  $\mathcal{H}'$  and consequently

describe the wave functions  $\Psi$  and  $\Psi'$ . Whether these two different wave functions define the same density or not can be checked by variational method. It turns out that two different external potentials can not describe the same ground state particle density. Therefore, the ground state energy of the system is a functional of its ground state particle density as in Eq. (3.1).

The second Hohenberg–Kohn theorem states that Eq. (3.1) delivers the ground state energy given the employed particle density belongs to the ground state of the system. For a certain density,  $n(\mathbf{r})$ , we have a certain  $V_{\text{ext}}$ , therefore, a certain  $\mathcal{H}$  and  $\Psi$ . If  $n(\mathbf{r})$  is the true ground state density described by  $V_{\text{ext}}(\mathbf{r})$ , by variational principle we have:

$$\begin{aligned} \langle \Psi' | \mathcal{H} | \Psi' \rangle &> \langle \Psi | \mathcal{H} | \Psi \rangle, \\ E[n'(\mathbf{r})] &> E[n(\mathbf{r})]. \end{aligned} \quad (3.2)$$

Therefore, the ground state density is genuinely the only function that minimizes the energy.

### The Kohn–Sham equations

The Kohn–Sham (KS) formulation is founded on Hohenberg–Kohn theorems [70]. The idea is to consider a system of non–interacting fermions under the influence of the same effective potential  $V_{\text{KS}}$  instead of a system of interacting fermions. Of course, the interacting and non–interacting systems of fermions yield different ground state density configurations. However, it is possible to map all interaction terms and the external potential term to  $V_{\text{KS}}$ .

The energy functional in a many–body system can be written as:

$$E[n] = T[n] + E_{\text{int}}[n] + E_{\text{ext}}[n], \quad (3.3)$$

where

$$T_{\text{KS}}[n] = -\frac{1}{2} \sum_{i=1}^N \int \Psi_i^*(\mathbf{r}) \nabla^2 \Psi_i(\mathbf{r}) d\mathbf{r} \quad (3.4)$$

is the kinetic energy of non–interacting particles.  $E_{\text{int}}[n]$  is the energy density functional representing all of the interactions between the particles and  $E_{\text{ext}}[n]$  is the energy density functional belonging to the external potential.

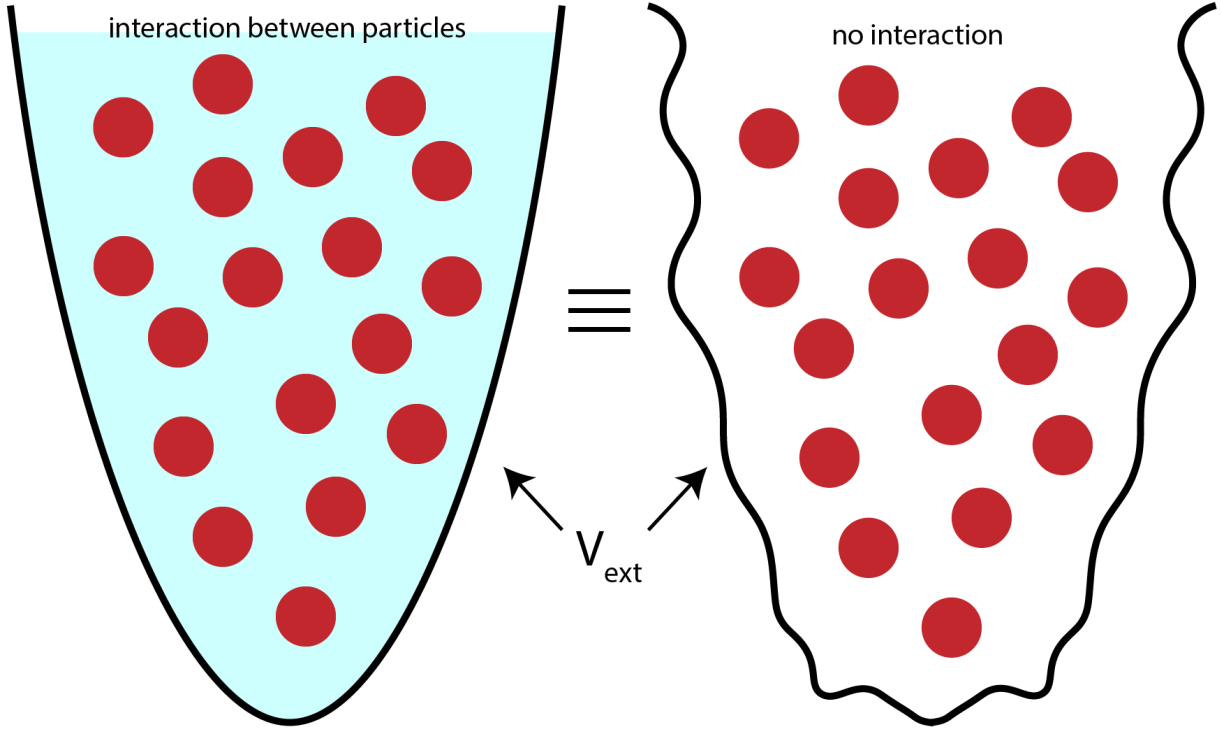


FIGURE 3.1: A schematic representation of equivalence between a real fermionic system under a harmonic potential (left) and Kohn–Sham framework (right). A set of interacting particles under a trivial external potential  $V_{\text{ext}}$  can be mapped to a set of non-interacting particles under the influence of a more complicating external potential.

The minimization of the energy yields to:

$$\begin{aligned}
 \epsilon_i \Psi_i(\mathbf{r}) &= \frac{\delta E}{\delta \Psi_i^*(\mathbf{r})}, \\
 \epsilon_i \Psi_i(\mathbf{r}) &= -\frac{1}{2} \nabla^2 \Psi_i(\mathbf{r}) + \left( \frac{\delta E_{\text{int}}[n]}{\delta n(\mathbf{r})} + \frac{\delta E_{\text{ext}}[n]}{\delta n(\mathbf{r})} \right) \frac{\delta n(\mathbf{r})}{\delta \Psi_i^*(\mathbf{r})}, \\
 \epsilon_i \Psi_i(\mathbf{r}) &= \left( -\frac{1}{2} \nabla^2 + V_{\text{KS}}(\mathbf{r}) \right) \Psi_i(\mathbf{r}).
 \end{aligned} \tag{3.5}$$

where  $V_{\text{KS}}(\mathbf{r}) = V_{\text{int}}(\mathbf{r}) + V_{\text{ext}}(\mathbf{r})$ . It can be seen that Eq. (3.5) is similar to Schrödinger equation. Eq. (3.5) describes a set of KS orbitals which defines the densities. Therefore, it is technically possible to map the interactions between the particles to a single potential known as the KS potential,  $V_{\text{KS}}$ .

It should be noted that the KS potential itself depends on the densities and the

densities are to be obtained by the KS potential. Therefore, one needs to solve this system self-consistently.

## 3.2 Superfluid Local Density Approximation

Although the KS framework states that it is possible to map an interacting system to a non-interacting one, it does not give any prescription on how to construct a KS potential. In order to describe superfluid or superconducting systems within the DFT, one needs to construct the energy density functional by means of particle density  $n(\mathbf{r})$ , kinetic density  $\tau(\mathbf{r})$ , and the anomalous density  $\nu(\mathbf{r})$ . Through the anomalous density, the pairing interaction can be determined as:

$$\Delta(\mathbf{r}\sigma, \mathbf{r}'\sigma') = -\frac{\delta\mathcal{E}[n, \nu]}{\delta\nu^*(\mathbf{r}\sigma, \mathbf{r}'\sigma')}. \quad (3.6)$$

The first attempt to construct a DFT formalism for superconductors has been done with the motivation to capture the properties of high-temperature superconductors [71, 72]. However, the non-local pairing potential  $\Delta(\mathbf{r}\sigma, \mathbf{r}'\sigma')$  gives rise to set of integro-differential equations which are highly difficult to deal with in practice. To reduce the difficulty of the problem, a local pairing potential  $\Delta(\mathbf{r})$  may be used [73]. The Superfluid Local Density Approximation (SLDA) has been developed over the years [74–77] by employing such a local pairing potential and has been confirmed to be very accurate [78–80].

In order to study the ultracold Fermi gas, one needs to solve Eq. (2.28) and find the wave functions and corresponding energies. In coordinate space, the equation has the following general form:

$$\begin{pmatrix} h_{\uparrow}(\mathbf{r}) & \Delta(\mathbf{r}) \\ \Delta^*(\mathbf{r}) & -h_{\downarrow}^*(\mathbf{r}) \end{pmatrix} \begin{pmatrix} u_{n,\uparrow}(\mathbf{r}) \\ v_{n,\downarrow}(\mathbf{r}) \end{pmatrix} = E_n \begin{pmatrix} u_{n,\uparrow}(\mathbf{r}) \\ v_{n,\downarrow}(\mathbf{r}) \end{pmatrix}. \quad (3.7)$$

The solutions corresponding to Eq. (2.29) can be obtained by the transformation:  $\{u_{n,\uparrow}(\mathbf{r}), v_{n,\downarrow}(\mathbf{r}), E_n\} \rightarrow \{v_{n,\uparrow}^*(\mathbf{r}), u_{n,\downarrow}^*(\mathbf{r}), -E_n\}$ . The densities are defined as the following:

$$n_\sigma(\mathbf{r}) = \sum_n |v_{n,\sigma}(\mathbf{r})|^2 f_\beta(-E_n), \quad (3.8)$$

$$\tau_\sigma(\mathbf{r}) = \sum_n |\nabla v_{n,\sigma}(\mathbf{r})|^2 f_\beta(-E_n), \quad (3.9)$$

$$v(\mathbf{r}) = \sum_n v_{n,\downarrow}^*(\mathbf{r}) u_{n,\uparrow}(\mathbf{r}) \frac{f_\beta(-E_n) - f_\beta(E_n)}{2}, \quad (3.10)$$

and the density functional that defines the ground state energy is:

$$E_{\text{gs}} = \int \mathcal{E}(n(\mathbf{r}), \tau(\mathbf{r}), v(\mathbf{r})) d\mathbf{r}. \quad (3.11)$$

It should be noted that the arguments of the energy density functional is not limited by three densities above. A better description of the system can be obtained with the addition of current densities  $\mathbf{j}(\mathbf{r})$  and density gradients  $\nabla n(\mathbf{r})$ .

In order to obtain such functional, the first candidate would be the BdG approach. One may construct a functional with the following form:

$$\mathcal{E}_{\text{BdG}} = \frac{\hbar^2 \tau}{2m} + g v^\dagger v, \quad (3.12)$$

where  $g$  is the coupling constant. The BdG method only includes the pairing interaction between the Cooper pairs (see Eq. (2.21)). The contribution coming from the self-energy (Hartree-Fock) term is disregarded. In the weak-coupling limit, this approach proved successful [64, 81]. However, the unitary limit has important differences from the BCS limit. In particular, the pairing field in the unitary regime is comparable to the Fermi energy which is contradictory to the BCS assumption,  $|\Delta| \ll \varepsilon_F$ . In this regime, the scattering length  $a$  diverges,  $a \rightarrow \infty$  and the approximate size of the Cooper pairs  $\xi$  decreases and becomes similar to the average inter-particle distance  $k_F^{-1}$ . This makes the unitary Fermi gas a better system than a BCS-superfluid to consider local pairing interactions. In the local density approximation, the anomalous density is divergent:  $v(\mathbf{r}, \mathbf{r}') \sim 1/(|\mathbf{r} - \mathbf{r}'|)$ . Therefore, to keep the pairing field  $\Delta = -gv$  finite, the coupling constant is taken as  $g \rightarrow 0$ .

### 3.2.1 Spin-symmetric case

In order to extend the DFT to superfluids, it is instructive to start with the spin-symmetric case  $n_\uparrow = n_\downarrow$ . The contribution of self-energy can be estimated from the

energy of non-interacting uniform Fermi gas which is described by the semi-classical Thomas–Fermi model as:

$$E_{\text{FFG}} = \frac{3}{5}\varepsilon_{\text{F}}N, \quad (3.13a)$$

$$E_{\text{FFG}} = \frac{3\hbar}{10m} \left(3\pi^2\right)^{2/3} n^{5/3}V, \quad (3.13b)$$

where  $N$  is the total particle number, and  $V$  is the volume of the system. The relevance of this semi-classical model to the unitary Fermi gas lies in the relation between the normal and superfluid states [17]. It is shown that for the unitary Fermi gas, where the scattering length diverges, the ground state energy is related to the energy of the free Fermi gas as in following:

$$E_{\text{unitary}} = E_{\text{FFG}}\zeta_{\text{B}}, \quad (3.14)$$

where  $\zeta_{\text{B}}$  is the Bertsch parameter. Using this model as an educated guess, the self-energy term is a functional of the density as  $\sim n(\mathbf{r})^{5/3}$ . By further dimensional analysis, the proposed Superfluid Local Density Approximation (SLDA) functional is:

$$\mathcal{E}_{\text{SLDA}} = \alpha \frac{\hbar^2\tau}{2m} + \beta \frac{3\hbar^2}{10m} \left(3\pi^2\right)^{2/3} n^{5/3} + gv^\dagger v, \quad (3.15)$$

where parameters  $\alpha$ , and  $\beta$  are obtained from fits to *ab initio* QMC results and experimental results [68]. The parameter  $\beta$  is taken so to recover the Bertsch parameter:

$$\beta = -0.526. \quad (3.16)$$

As it can be seen, the parameter  $\alpha$  stands for the effective mass  $m_{\text{eff}} = m/\alpha$ , which will be elaborated on in the next section.

## Regularization

One obstacle in framework of the SLDA is, as mentioned above, the divergence of the anomalous and kinetic densities. In order to deal with that, an energy cutoff is introduced to the densities:

$$n_\sigma(\mathbf{r}) = \sum_{|E_k| < E_c} |v_{k,\sigma}(\mathbf{r})|^2 f_\beta(-E_k), \quad (3.17)$$

$$\tau_\sigma(\mathbf{r}) = \sum_{|E_k| < E_c} |\nabla v_{k,\sigma}(\mathbf{r})|^2 f_\beta(-E_k), \quad (3.18)$$

$$v(\mathbf{r}) = \sum_{|E_k| < E_c} v_{n,\downarrow}^*(\mathbf{r}) u_{k,\uparrow}(\mathbf{r}) \frac{f_\beta(-E_k) - f_\beta(E_k)}{2}. \quad (3.19)$$

According to the above equations, the densities are calculated from BCS parameters whose eigenvalues are below  $E_c$ . Therefore, the resulting pairing field  $\Delta = -g_{\text{eff}}v_c$  is finite. As dictated by the self-consistency requirement of the pairing field (see Eq. (2.33)), the coupling constant should be renormalized according to the regularization scheme. In Ref.[75] it is introduced such a scheme where the renormalized coupling constant,  $g_{\text{eff}}$  can be obtained from:

$$\frac{1}{g_{\text{eff}}(\mathbf{r})} = \frac{1}{g(\mathbf{r})} - \frac{mk_c(\mathbf{r})}{2\pi^2\hbar^2} \left( 1 - \frac{k_F(\mathbf{r})}{2k_c(\mathbf{r})} \ln \frac{k_c(\mathbf{r}) + k_F(\mathbf{r})}{k_c(\mathbf{r}) - k_F(\mathbf{r})} \right), \quad (3.20)$$

where  $k_c$  is the momentum cutoff corresponding to the cutoff energy  $E_c$ . In Ref.[75] it is shown that, for cutoff energies that are large enough compared to the Fermi energy, the pairing field is no more a function of cutoff energy; it stays the same as the cutoff is increased. Therefore, the above regularization procedure effectively gives the same result with non-divergent densities compared to infinite cutoff.

### 3.2.2 Polarized case

In spin-imbalanced case, the local polarization is given by:

$$p(\mathbf{r}) = \frac{n_\uparrow(\mathbf{r}) - n_\downarrow(\mathbf{r})}{n_\uparrow(\mathbf{r}) + n_\downarrow(\mathbf{r})}. \quad (3.21)$$

With the introduction of non-zero polarization, the energy density functional in Eq. (3.15) is generalized as the Asymmetric Superfluid Density Functional (ASLDA) [68]:

$$\mathcal{E}_{\text{ASLDA}} = \frac{\hbar^2}{m} \left( \alpha_\uparrow(n_\uparrow, n_\downarrow) \frac{\tau_\uparrow}{2} + \alpha_\downarrow(n_\uparrow, n_\downarrow) \frac{\tau_\downarrow}{2} + D(n_\uparrow, n_\downarrow) \right) + g_{\text{eff}} v^\dagger v, \quad (3.22)$$

with the definitions:

$$\alpha(p) = 1.094 + 0.156p \left(1 - \frac{2p^2}{3} + \frac{p^4}{5}\right) - 0.532p^2 \left(1 - p^2 + \frac{p^4}{3}\right), \quad (3.23a)$$

$$\alpha_{\uparrow}(n_{\uparrow}, n_{\downarrow}) = \alpha(p), \quad (3.23b)$$

$$\alpha_{\downarrow}(n_{\uparrow}, n_{\downarrow}) = \alpha(-p), \quad (3.23c)$$

$$D(n_{\uparrow}, n_{\downarrow}) = \frac{(6\pi^2(n_{\uparrow} + n_{\downarrow}))^{5/3}}{20\pi^2} \left[ G(p) - \alpha(p) \left(\frac{1+p}{2}\right)^{5/3} - \alpha(-p) \left(\frac{1-p}{2}\right)^{5/3} \right], \quad (3.23d)$$

$$G(p) = 0.357 + 0.642p^2, \quad (3.23e)$$

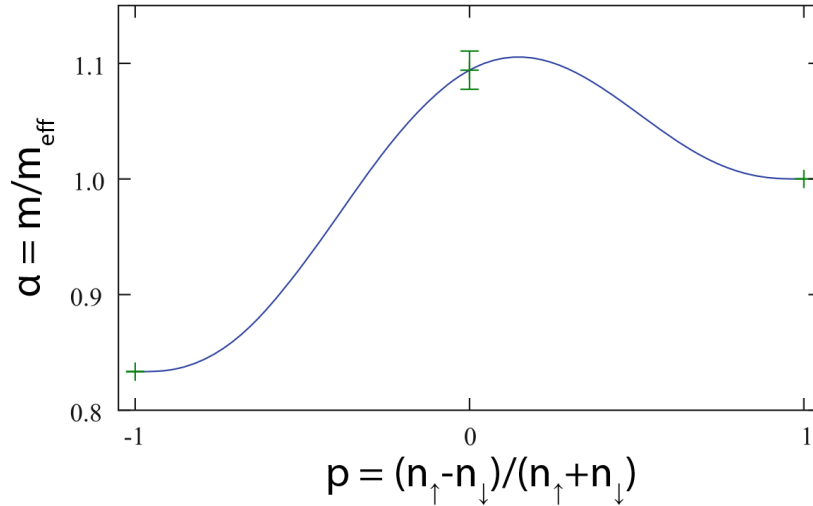


FIGURE 3.2: The extraction of the effective mass parameter  $\alpha$  from three cases  $p = -1$ ,  $p = 0$ , and  $p = 1$  indicated by green ticks. Resulting fit is given in Eq. (3.23a). The figure is taken from Ref. [68].

and finally, the effective coupling constant is calculated by

$$\frac{\alpha_+}{g_{\text{eff}}} = \frac{m}{\hbar^2} \frac{\alpha_+(n_{\uparrow} + n_{\downarrow})^{1/3}}{\gamma} - \frac{mk_c(\mathbf{r})}{2\pi^2\hbar^2} \left(1 - \frac{k_F(\mathbf{r})}{2k_c(\mathbf{r})} \ln \frac{k_c(\mathbf{r}) + k_F(\mathbf{r})}{k_c(\mathbf{r}) - k_F(\mathbf{r})}\right), \quad (3.24)$$

where  $\alpha_+ = (\alpha_{\uparrow} - \alpha_{\downarrow})/2$ . The parameter  $\gamma$  is obtained from QMC calculations to reflect the  $|\Delta|/\varepsilon_F = 0.504$  ratio of the unitary Fermi gas:

$$\gamma = -11.11. \quad (3.25)$$

The SLDA functional in Eq. (3.15) can be obtained by employing the ASLDA functional (Eq. (3.22)) for  $p = 0$  case. The parameter  $\alpha$  is obtained from different QMC results under polarizations (Eq. (3.23a)). Namely, the effective mass of majority and minority particles in the limit of fully-polarized system and the spin-symmetric scenario (see Fig. 3.2).

$(N_a, N_b)$	$E_{FNDMC}$	$E_{ASLDA}$	(error) (%)
<i>Normal State</i>			
(3,1)	$6.6 \pm 0.01$	6.687	1.3
(4,1)	$8.93 \pm 0.01$	8.962	0.36
(5,1)	$12.1 \pm 0.1$	12.22	0.97
(5,2)	$13.3 \pm 0.1$	13.54	1.8
(6,1)	$15.8 \pm 0.1$	15.65	0.93
(7,2)	$19.9 \pm 0.1$	20.11	1.1
(7,3)	$20.8 \pm 0.1$	21.23	2.1
(7,4)	$21.9 \pm 0.1$	22.42	2.4
(8,1)	$22.5 \pm 0.1$	22.53	0.14
(9,1)	$25.9 \pm 0.1$	25.97	0.27
(9,2)	$26.6 \pm 0.1$	26.73	0.5
(9,3)	$27.2 \pm 0.1$	27.55	1.3
(9,5)	$30 \pm 0.1$	30.77	2.6
(10,1)	$29.4 \pm 0.1$	29.41	0.034
(10,2)	$29.9 \pm 0.1$	30.05	0.52
(10,6)	$35 \pm 0.1$	35.93	2.7
(20,1)	$73.78 \pm 0.01$	73.83	0.061
(20,4)	$73.79 \pm 0.01$	74.01	0.3
(20,10)	$81.7 \pm 0.1$	82.57	1.1
(20,20)	$109.7 \pm 0.1$	113.8	3.7
(35,4)	$154 \pm 0.1$	154.1	0.078
(35,10)	$158.2 \pm 0.1$	158.6	0.27
(35,20)	$178.6 \pm 0.1$	180.4	1
<i>Superfluid State</i>			
(1, 1)	$2.002 \pm 0$	2.302	15
(2, 2)	$5.051 \pm 0.009$	5.405	7
(3, 3)	$8.639 \pm 0.03$	8.939	3.5
(4, 4)	$12.573 \pm 0.03$	12.63	0.48
(5, 5)	$16.806 \pm 0.04$	16.19	3.7
(6, 6)	$21.278 \pm 0.05$	21.13	0.69
(7, 7)	$25.923 \pm 0.05$	25.31	2.4
(8, 8)	$30.876 \pm 0.06$	30.49	1.2
(9, 9)	$35.971 \pm 0.07$	34.87	3.1
(10, 10)	$41.302 \pm 0.08$	40.54	1.8
(11, 11)	$46.889 \pm 0.09$	45	4
(12, 12)	$52.624 \pm 0.2$	51.23	2.7
(13, 13)	$58.545 \pm 0.18$	56.25	3.9
(14, 14)	$64.388 \pm 0.31$	62.52	2.9
(15, 15)	$70.927 \pm 0.3$	68.72	3.1
(1, 0)	$1.5 \pm 0.0$	1.5	0
(2, 1)	$4.281 \pm 0.004$	4.417	3.2
(3, 2)	$7.61 \pm 0.01$	7.602	0.1
(4, 3)	$11.362 \pm 0.02$	11.31	0.49
(7, 6)	$24.787 \pm 0.09$	24.04	3
(11, 10)	$45.474 \pm 0.15$	43.98	3.3
(15, 14)	$69.126 \pm 0.31$	62.55	9.5

FIGURE 3.3: The comparison between the Superfluid Local Density Approximation (SLDA) and the *ab initio* fixed-node diffusion Monte Carlo (FNDMC) calculations performed for a harmonically trapped unitary Fermi gas at zero temperature. The figure is taken from Ref. [68].

In Fig. 3.3 the comparison between *ab initio* QMC results and the (A)SLDA results is presented. The normal state in (A)SLDA has been calculated by fixing  $\Delta = 0$  in the functional. The superfluid system is considered in the unitary regime, and the system is in a harmonic trap. The comparison shows the high agreement between the methods and validates the accuracy of the (A)SLDA method.

### 3.2.3 Time-dependent ASLDA

Time-dependent phenomena within the Kohn–Sham framework relies on the Runge–Gross theorem which is essentially an analogue of Hohenberg–Kohn theorems for the time-dependent Schrödinger equation [82]. The theorem states that a given initial state  $\Psi_0$  evolving under the influence of two different external potentials  $V_{\text{ext}}$  and  $V'_{\text{ext}}$  results to two different densities  $n(\mathbf{r}, t)$  and  $n'(\mathbf{r}, t)$ . An important remark is that if the external potentials are different only by a time-dependent constant  $c(t)$ , the fermionic densities would be  $n(\mathbf{r}, t) = n'(\mathbf{r}, t)$ . The Runge–Gross theorem states that the resulting densities are different only if the external potentials are different.

ASLDA can be extended to a time-dependent framework in order to describe the dynamics of the unitary Fermi gas. Under the time-dependent ASLDA (TDASLDA) framework, the BCS parameters  $u(\mathbf{r}, t)$  and  $v(\mathbf{r}, t)$  evolve in similar way to time-dependent BdG equations [68]:

$$i\hbar \frac{\partial}{\partial t} \begin{pmatrix} u_{n,\uparrow}(\mathbf{r}, t) \\ u_{n,\downarrow}(\mathbf{r}, t) \\ v_{n,\uparrow}(\mathbf{r}, t) \\ v_{n,\downarrow}(\mathbf{r}, t) \end{pmatrix} = \begin{pmatrix} h_{\uparrow}(\mathbf{r}, t) & 0 & 0 & \Delta(\mathbf{r}, t) \\ 0 & h_{\downarrow}(\mathbf{r}, t) & -\Delta(\mathbf{r}, t) & 0 \\ 0 & -\Delta^*(\mathbf{r}, t) & -h_{\uparrow}^*(\mathbf{r}, t) & 0 \\ \Delta^*(\mathbf{r}, t) & 0 & 0 & -h_{\downarrow}^*(\mathbf{r}, t) \end{pmatrix} \begin{pmatrix} u_{n,\uparrow}(\mathbf{r}, t) \\ u_{n,\downarrow}(\mathbf{r}, t) \\ v_{n,\uparrow}(\mathbf{r}, t) \\ v_{n,\downarrow}(\mathbf{r}, t) \end{pmatrix}, \quad (3.26)$$

where  $h_{\sigma}(\mathbf{r}, t) = -\frac{\nabla^2}{2} - \mu_{\sigma} + U_{\sigma}(\mathbf{r}, t)$  is the single-particle part and  $U_{\sigma}(\mathbf{r}, t)$  denotes the time-dependent external potential, and they are real functions. The initial state to evolve in time is the ground state described by ASLDA.

In the dynamical framework it is always interesting to examine time-reversal symmetry breaking phenomena. Therefore, the current density becomes an important quantity. It is defined as:

$$\mathbf{j}_{\sigma}(\mathbf{r}) = \frac{i}{2} \sum_{|E_k| < E_c} [v_{n,\sigma}^*(\mathbf{r}) \nabla v_{n,\sigma}(\mathbf{r}) - v_{n,\sigma}(\mathbf{r}) \nabla v_{n,\sigma}^*(\mathbf{r})] f_{\beta}(-E_n). \quad (3.27)$$

The effective mass parameter  $\alpha$  is a function of local polarization  $p(\mathbf{r})$  (Eq. (3.23a)). Since the effective mass is defined locally, in dynamic calculations, the Galilean invariance has to be restored. For this reason, the TDASLDA functional has a different form than the ASLDA functional. The TDASLDA functional is:

$$\mathcal{E}_{\text{TDASLDA}} = \frac{\hbar^2}{m} \left( \alpha_{\uparrow} \frac{\tau_{\uparrow}}{2} + \alpha_{\downarrow} \frac{\tau_{\downarrow}}{2} + D \right) + g_{\text{eff}} \nu^{\dagger} \nu + (1 - \alpha_{\uparrow}) \frac{|j_{\uparrow}|^2}{2n_{\uparrow}} + (1 - \alpha_{\downarrow}) \frac{|j_{\downarrow}|^2}{2n_{\downarrow}}. \quad (3.28)$$

Another remark on the TDASLDA is on the stability of evolution. The time evolution of a closed system necessitates the conservation of the total energy by the first law of thermodynamics. However, the energy may not be conserved due to the energy cutoff employed for the means of regularization. In order to examine the effect of the truncated momentum space, let us turn to Bogoliubov transformation:

$$\begin{pmatrix} c \\ c^{\dagger} \end{pmatrix} = \mathcal{B} \begin{pmatrix} \gamma \\ \gamma^{\dagger} \end{pmatrix}, \quad (3.29)$$

where the transformation matrix is [60]:

$$\mathcal{B} = \begin{pmatrix} U & V^* \\ V & U^* \end{pmatrix}. \quad (3.30)$$

The completeness of the transformation matrix,  $\mathcal{B}\mathcal{B}^{\dagger} = 1$  ensures the fermionic anti-commutation relations to be present in the quasi-particle basis. However, the transformation spans over the whole Hilbert space. Therefore, in the presence of a cutoff (e.g., momentum cutoff), the relation  $\mathcal{B}\mathcal{B}^{\dagger} = 1$  does not hold anymore, and the system does not strictly show fermionic behavior. Consequently, the particle and anomalous densities constituted by the  $U$ 's and  $V$ 's become inconsistent, resulting in non-conservation of the energy (defined through the densities). Nevertheless, this effect depends on the strength of the pairing field and the size of the cutoff. For a relatively short amount of time, the accuracy in the energy conservation is still high [80].

### 3.3 Numerical details

In a 1D system, the Hamiltonian given at Eq. (3.7) has the size of  $2L \times 2L$ , where  $L$  is the lattice size. For the 3D case, the size of the Hamiltonian greatly increases and becomes  $2L_x L_y L_z \times 2L_x L_y L_z$ . Moreover, in order to obtain meaningful results, the non-equilibrium study of ultracold gases needs rather large lattices. The average lattice size (or the box size) used in this study for time-dependent calculations is  $L^3 = 40k_F^{-3}$ . This means  $\sim 10^5$  coupled partial differential equations that need to evolve in time. Therefore, the study presented in this thesis is computationally highly demanding. The simulations are performed using different supercomputers from around the world: Tsubame (Japan), Piz Daint (Switzerland), Okeanos (Poland), Prometheus (Poland). Within this study, the W-SLDA toolkit is used [83]. This study, among others, has been used as a benchmark during the development of the toolkit.

The W-SLDA toolkit has a hybrid structure: It typically employs central processing units (CPUs) in order to carry the static calculations, which are mainly diagonalization of the BdG Hamiltonian. For a time-dependent studies using graphical processing units (GPUs) increases the technical limits remarkably.

The toolkit employs a Cartesian lattice grid which can be constructed in one, two, or three dimensions with periodic boundary conditions. The Laplacian and gradient operators are calculated in the momentum space, using fast-Fourier-transform (FFT) algorithms. From the eigenvectors of the Hamiltonian, it is possible to construct the various densities, such as particle densities, anomalous density, etc. These densities can be used to extract the observables of the system.

The static code utilizes multiple CPUs, although it can be supported by the use of GPUs. The CPU codes are written in C99 language and employ the message passing interface (MPI) for the parallelization to fasten the BdG matrix's diagonalization. In static calculations, the diagonalization of the matrix consumes the most time. The matrix is separated between MPI processes using "block-cyclic distribution." The method decomposes the matrix into repeating blocks, dividing the matrix into different processes (see Fig. 3.4) and reducing the dimensionality in order to gain speed without losing accuracy [83].

After decomposing the matrix into cyclic blocks, it is diagonalized using ScaLAPACK (CPU based) or ELPA (GPU based) libraries. The detailed information on ELPA library can be found at Refs. [83, 84]. One diagonalization corresponds to one iteration of the code. The diagonalization begins with an initial guess for the problem (e.g., the

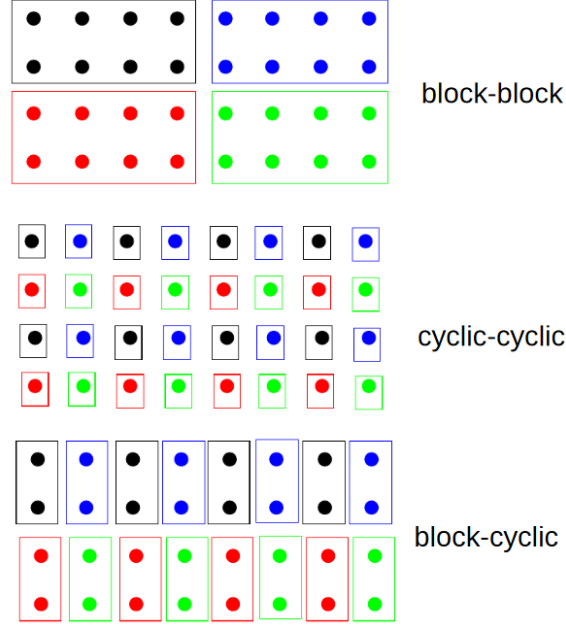


FIGURE 3.4: The comparison between block, cyclic and block–cyclic (bc) methods. Bc method is a compromise between the other methods. For more details see Ref. [83].

particle and anomalous densities for the uniform case). During the diagonalization, the total energy of the system is minimized:

$$\langle \Omega \rangle = \left\langle H - \sum_{\sigma=\{\uparrow,\downarrow\}} \mu_{\sigma} N_{\sigma} \right\rangle. \quad (3.31)$$

By minimization, convergence in both energy and particle number is achieved. The convergence is reached when the value of the parameter (e.g., energy or particle number) is changed only by a tolerance after the previous iteration. For example, in the case of energy convergence, the algorithm stops when  $|E_{\text{final}} - E_{\text{final-1}}| \leq 10^{-6}$  where  $E_{\text{final}}$  is the total energy of the system after the last iteration, and  $E_{\text{final-1}}$  is the total energy one iteration before the last one.

The time–dependent code solves the following form:

$$i \frac{\partial \Psi_n(t)}{\partial t} = \mathcal{H}(\Psi_n, t) \Psi_n(t), \quad (3.32)$$

where the Hamiltonian and the wave functions have the form in Eq. (3.7). The time–evolution is performed using the Adams–Bashforth–Moulton (ABM) algorithm.

Within this scheme, the initial definitions are:

$$f(y, t) = \frac{\partial y(t)}{\partial t}, \quad (3.33)$$

where

$$\begin{aligned} y(t) &\equiv \Psi_n(\mathbf{r}, t), \\ f(y, t) &\equiv i^{-1} (\mathcal{H}(\Psi_n, t) - \langle \mathcal{H} \rangle_n) \Psi_n(t). \end{aligned} \quad (3.34)$$

Here,  $\langle \mathcal{H} \rangle$  is the *instantaneous* quasi-particle energy [79, 83]. From these definitions, the ABM algorithm has the following predictor-corrector structure:

- 4th order predictor:

$$y_k^p = y_{k-1} + \frac{55}{24} \Delta t f_{k-1} - \frac{59}{24} \Delta t f_{k-2} + \frac{37}{24} \Delta t f_{k-3} - \frac{9}{24} \Delta t f_{k-4}. \quad (3.35)$$

- 5th order corrector:

$$y_k = y_{k-1} + \frac{251}{720} \Delta t f(y_k^p, k\Delta t) + \frac{646}{720} \Delta t f_{k-1} - \frac{264}{720} \Delta t f_{k-2} + \frac{106}{720} \Delta t f_{k-3} - \frac{19}{720} \Delta t f_{k-4}. \quad (3.36)$$

In Fig. 3.5 the job distribution diagram of W-SLDA toolkit is presented. Most of the "run-time" is occupied by the (cu)FFT (41%) and the multiplication of the wave functions by the momenta vectors (11%). During these two operations, the Lapcaian and gradients of wave functions are calculated. Therefore, this process alone takes more than half of the run-time. Another time-consuming procedure is the MPI communication ( $\sim 20\%$ ) which strongly depends on the amount of data processed by the GPU each time step.

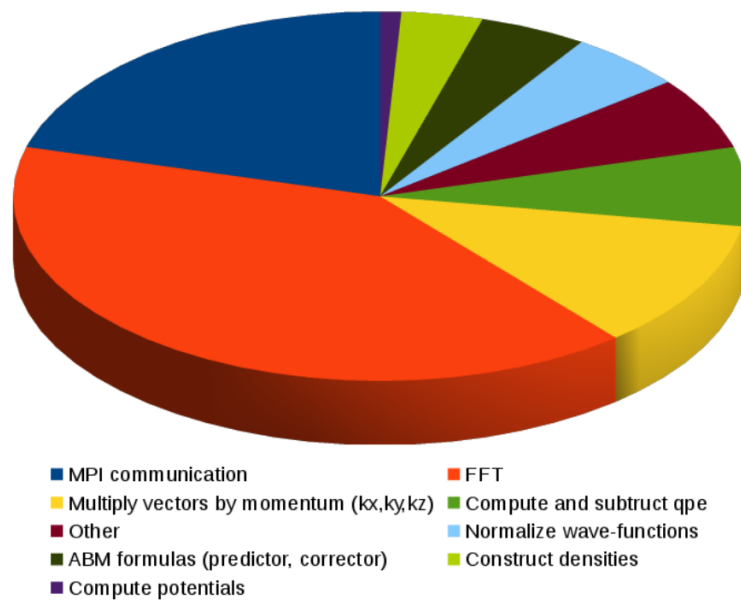


FIGURE 3.5: Profiling of TDSLDA code executed on 512 GPUs (Piz Daint).  
For more details see Ref. [83].



## Chapter 4

# Dynamic creation of spin-polarized impurity

The superfluid systems are separated from single-particle excitations by the pairing gap. Therefore, the polarized particles who can not form Cooper pairs are expelled from the superfluid. The question whether there is a stable polarized superfluid configuration has gathered a lot of attention [25–38]. This chapter introduces the ferron, a spin-polarized impurity which stores the local polarization inside the superfluid system. In particular, as the title suggests, the creation of the ferron by a time-dependent, spin-selective external potential is shown and the stability of the ferron is discussed.

To investigate the spin-imbalance in ultracold Fermi gas, we start with a cubic 3D simulation box where the periodic boundary conditions are imposed. The density of the box is set accordingly to obtain  $k_F = (3\pi^2 n)^{1/3} \approx 1$ , where  $n$  is the particle density inside the box. The regime we consider is the unitary Fermi gas (UFG). Since it has the strongest pairing field, the UFG offers a larger window to admit magnetic impurities without destroying the superfluidity [20, 22, 23]. As it is described in the previous chapter, we employ the TDASLDA method to simulate and capture the dynamics of the UFG. We start with minimizing the energy for the spin-balanced case and obtaining a uniform solution by solving the static equations. Next, we switch to dynamics where a time-dependent local external potential is introduced. The potential has the Gaussian form in real space and is spin-selective: attractive for one spin component and repulsive for the other. Therefore, it locally breaks the Cooper pairs (see Fig. 4.1). The external potential has the following form:

$$V_i(\mathbf{r}, t) = \lambda_i A(t) \exp \left[ -\frac{x^2 + (1 - \epsilon_y)y^2 + (1 - \epsilon_z)z^2}{2\sigma^2} \right], \quad (4.1)$$

where  $\lambda_i = \pm 1$  describes if the potential is attractive or repulsive. It is set as  $\lambda_\uparrow = 1$

and  $\lambda_{\downarrow} = -1$ . Therefore, the potential attracts the spin-down particles and repels the spin-up particles. The amplitude,  $A(t)$  is a function of time. The external potential used to break the Cooper pairs excites phonons in the system that interacts with the particles. To avoid this effect as much as possible, we adiabatically turn the potential on, keep it on for some time, and slowly turn it off. The amplitude is:

$$A(t) = \begin{cases} A_0 s(t, t_{\text{on}}), & 0 \leq t < t_{\text{on}}, \\ A_0, & t_{\text{on}} \leq t < t_{\text{hold}}, \\ A_0 [1 - s(t - t_{\text{hold}}, t_{\text{off}} - t_{\text{hold}})], & t_{\text{hold}} \leq t < t_{\text{off}}, \\ 0, & t \geq t_{\text{off}}, \end{cases} \quad (4.2)$$

where

$$s(t, w) = \frac{1}{2} + \frac{1}{2} \tanh \left[ \tan \left( \frac{\pi t}{w} - \frac{\pi}{2} \right) \right], \quad (4.3)$$

is the switching function used in order to introduce the potential adiabatically. The typical maximum strength of the external potential is,  $A_0 = 2\varepsilon_{\text{F}}$ . The parameters  $\varepsilon_y$ , and  $\varepsilon_z$  are introduced to break the spherical symmetry of the potential,  $\varepsilon_{y,z} = 10^{-6}$ . Finally,  $\sigma$  is the width of the potential in units of lattice spacing,  $k_{\text{F}}^{-1}$ .

The time-evolution of the total energy of the system under such potential is given in Fig. 4.1. It can be seen that the energy only changes when the time derivative of the external potential is non-zero, in other words, when the potential is performing the necessary work to break the Cooper pairs. Otherwise, the energy is conserved, proving the stability of the simulations. We, typically, set  $t_{\text{on}} = t_{\text{off}} = 25t\varepsilon_{\text{F}}$  and the total application duration of the potential is  $t_{\text{pot}} = 150t\varepsilon_{\text{F}}$ . The excitation energy showed in Fig. 4.1 is due to both the newly created unpaired particles and the excited phonons in the system.

During the pair-breaking process, the Fermi surfaces corresponding to different spin components shift inside the volume where the potential is applied. This shift causes oscillations in the pairing field [40], and eventually induces a nodal shell. Inside this shell, the phase of the pairing field is shifted by  $\pi$ . In Fig. 4.2, it can be seen that the excess particles occupy the states at the vicinity of the nodal shell. This is effectively analogous to the superconductor - ferromagnet - superconductor (SFS) junctions where the ferromagnet part is composed of one spin component and the phase of the pairing field changes by  $\pi$  across the junction [40]. It is because of this similarity; this particular spin-polarized shell is named as ferron.

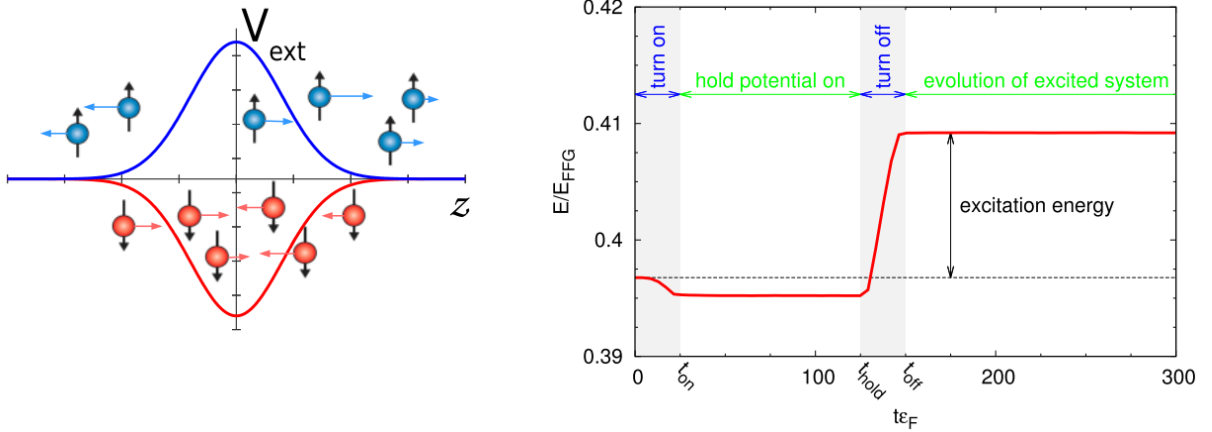


FIGURE 4.1: The schematic of the spin-selective external potential (left subfigure) and an example of time evolution of the total energy of the system (right subfigure). Both images are taken from Ref. [46].

In Fig. 4.3 two snapshots during the time evolution are presented. The Gaussian potential is applied to the center of the simulation box. The 3D results are presented as cross-sections from the center of the box. The upper subfigure shows a configuration while the external potential is active. It can be seen that, at that time, the phase inside the region where the potential is applied is shifted by  $\pi$  with respect to the bulk value. This creates a nodal shell where the magnitude of the pairing field goes through zero while changing its sign due to the phase shift. The local polarization,  $p(\mathbf{r}) = \frac{n_{\uparrow}(\mathbf{r}) - n_{\downarrow}(\mathbf{r})}{n_{\uparrow}(\mathbf{r}) + n_{\downarrow}(\mathbf{r})}$  shows that the majority of the unpaired particles occupy the region where  $|\Delta(\mathbf{r})| \rightarrow 0$ . The spin-up particles that are repelled by the external potential create a uniform non-zero polarization in bulk.

After the potential is turned off, the pairing field, which was previously suppressed, recovers itself because of the proximity effect. However, its phase is still shifted, and the nodal surface remains. If the radius of the nodal shell is close to the coherence length, the pairing may not recover itself to its bulk strength. As a result, this creates a non-zero polarization even in the core of the object. This non-zero polarization in the center is enhanced by the phonon scatterings. However, the majority of the unpaired population is gathered at the nodal shell (see lower subfigure of Fig. 4.3).

One of the essential properties of the ferron is its stability. Once the nodal shell is formed, the external potential is removed from the system. If the system parameters are adjusted appropriately, the simulations show that the object is stable by itself up to  $t\varepsilon_F \approx 1000$  without hinting at any sign of decay.

The stability of the ferron is affected by various system parameters. The first check

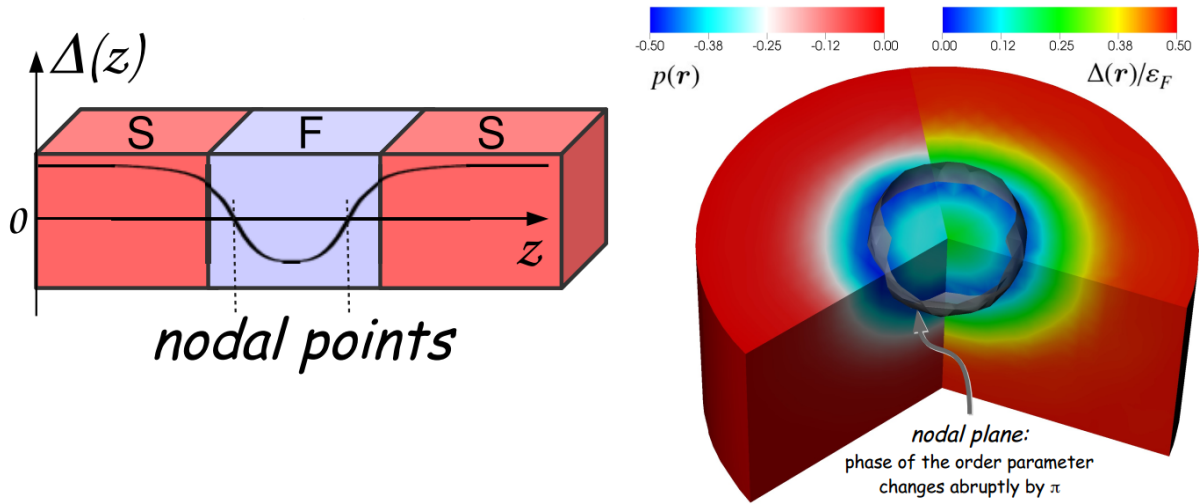


FIGURE 4.2: **Left subfigure:** The behavior of the pairing field within a SFS junction. The phase of the pairing field is shifted by  $\pi$  across the junction. **Right subfigure:** The structure of the polarized shell in 3D. On the left-hand side of the figure the local spin polarization,  $p(\mathbf{r})$  and on the right-hand side the local pairing strength,  $|\Delta(\mathbf{r})|$  is shown.

is the effect of the size of the simulation box,  $L^3$ . Fig. 4.4 shows that for a box size of  $L^3 \approx (19\xi)^3$ , the nodal shell is unstable, and the system eventually recovers its initial completely paired configuration with the extra presence of excited phonons. This instability is due to the phonons interacting with the unpaired population. When the box size is too small, the perturbations due to the external potential are enhanced because of the periodic boundary effects. The enhanced phonon scatterings lead to the destruction of the polarized nodal shell. In Fig. 4.4 it can be seen that a box size of  $L^3 = (31.42\xi)^3$  allows enough distance between the periodic potentials and the impurity is stable. Moreover, it can be seen that the amplitude of deviations from  $\delta\varphi = \pi$  line decreases for a larger box such as  $L^3 = (47.12\xi)^3$ .

The next parameter is the size of the Gaussian external potential,  $\sigma$ . To test the stability due to the potential size, simulations with different sizes ranging from  $2.36\xi$  to  $7.37\xi$  are performed. Fig. 4.5 (upper subfigure) shows for small sizes, such as  $\sigma = 2.36\xi$ , the ferron is destroyed after the potential is turned off. If the polarizing potential is too small, the pairing field inside the nodal shell is weaker than the bulk pairing strength. This is because the oscillations of the pairing field are on the order of the coherence length  $\xi$ . In such a case, the unpaired particles may tunnel across the droplet leading to the decay of the structure. Moreover, since the dynamically created system is far from equilibrium, the phonon scatterings may contribute to the decay. Therefore,

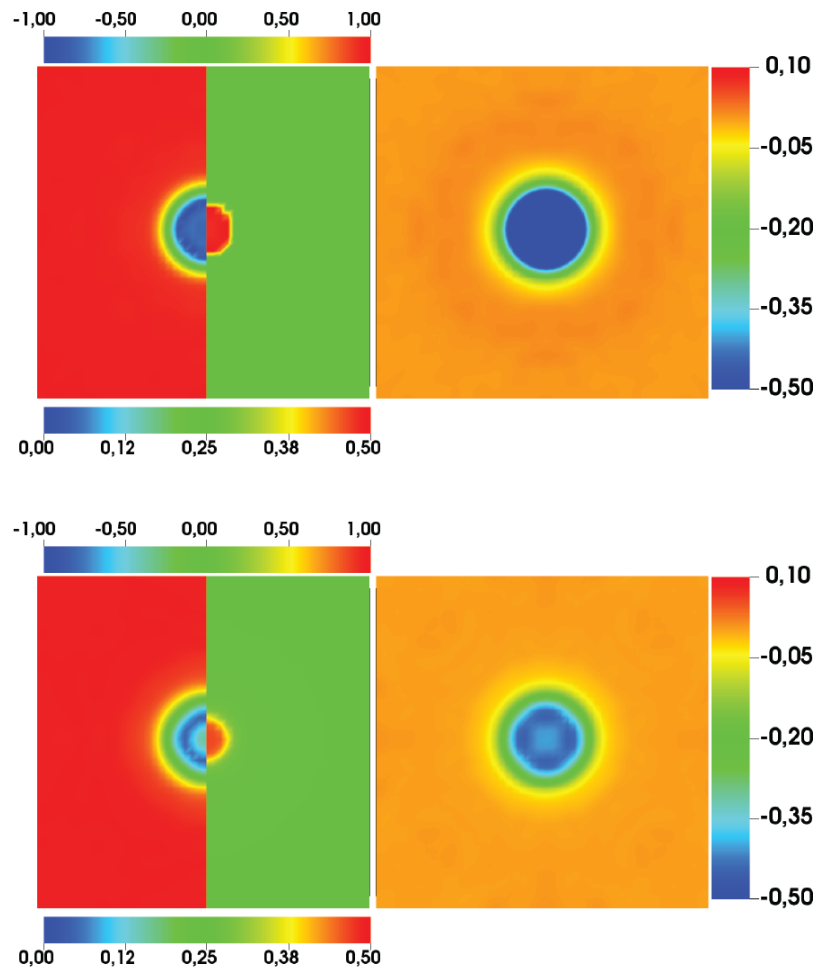


FIGURE 4.3: Two snapshots of the dynamical creation of the ferron is presented. The upper subfigure is a snapshot while the potential is applied, and the lower subfigure is after the potential is turned off. The potential is turned off at  $t_{\varepsilon_F} = 150$ . In both figures, on the left half-box, the magnitude of the pairing field is presented, while on the right half-box, the phase of the pairing field is given. The right image in both figures is the local spin-polarization.

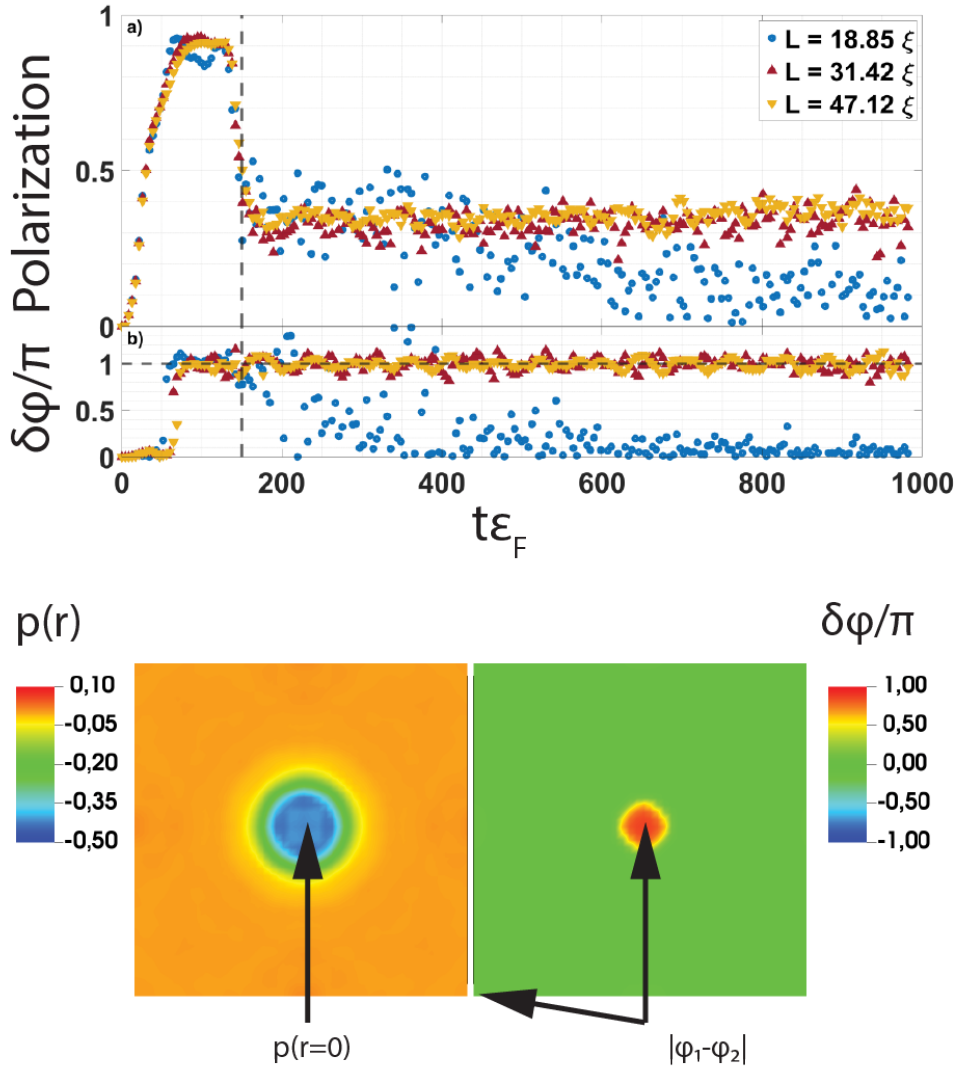


FIGURE 4.4: The effect of the periodic box size on the creation of a stable droplet. The polarization and the phase difference are calculated at the center of the box as a reference to the bulk values. **Upper subfigure:** Panel a) shows the time evolution of the relative local polarization for different box sizes. Panel b) shows the time evolution of the phase difference. The vertical dashed lines represent when the external potential is completely turned off ( $t\varepsilon_F = 150$ ). The horizontal dashed line in the panel b) is a guide to the eye, showing  $\delta\varphi = \pi$ . **Lower subfigure:** This figure demonstrates the relative phase difference and the polarization. The bulk values are taken from the edge of the box.

the pairing field inside the shell plays the part of an effective potential barrier to protect the shell from collapsing. In Fig. 4.5 we numerically confirm for sizes  $\sigma \gtrsim 3\zeta$ , the pairing field inside the nodal shell prevents the collapse.

In Fig. 4.5 (upper subfigure), for wide potentials, such as  $\sigma = 7.07\zeta$ , we, again, encounter with the instability, which is attributed to the  $t_{\text{hold}}$  parameter. Fig. 4.6 (upper subfigure) shows for a potential with  $\sigma = 7.07\zeta$ , the extended application duration of the potential is successful on the creation of the nodal shell. A wider potential means a larger surface for the nodal shell that needs to be occupied by a larger number of unpaired particles. Extended application duration of the polarizing potential eventually causes the necessary shift in the Fermi surfaces to generate the oscillation of the pairing field.

Another system parameter is the maximum strength of the Gaussian potential,  $A_0$ . In Fig. 4.6 (lower subfigure) the effect of different amplitudes is shown. For weak amplitudes, such as  $A_0 = 1\varepsilon_F$ , the potential is not strong enough to create the nodal shell for a given  $t_{\text{hold}}$ . On the other hand, large amplitudes, such as  $A_0 = 4\varepsilon_F$ , the potential excites background phonons which interact with the polarized population, causing instability and eventually leading to a possible decay of the nodal shell.

The final system parameter is the switching on/off rates of the external potential,  $t_{\text{switch}}$ . It describes the effect of adiabaticity on the creation of the ferron. Fig. 4.7 shows the ferron is stable even with a sudden introduction of the potential. However, it can be seen that a more adiabatic process transfers less energy to the system. Such a case excites fewer phonons than less adiabatic cases, resulting in a configuration closer to equilibrium. Therefore, more adiabatic processes provide more stable structures.

## 4.1 Stability of the ferron

So far, we have investigated various system parameters that can be tuned to obtain a stable ferron. Among those parameters, the only physical limitation is the minimum size of the ferron. As mentioned above, the pairing inside the nodal shell behaves as an effective potential barrier, preventing the collapse of the nodal shell. Since the healing of the pairing field occurs on the order of the coherence length, a ferron smaller than a certain size can not exist.

To investigate ferron's stability, we turn to 1D case to see the geometry and dimensionality effects. To simulate a 1D UFG system, instead of TDASLDA, we have used

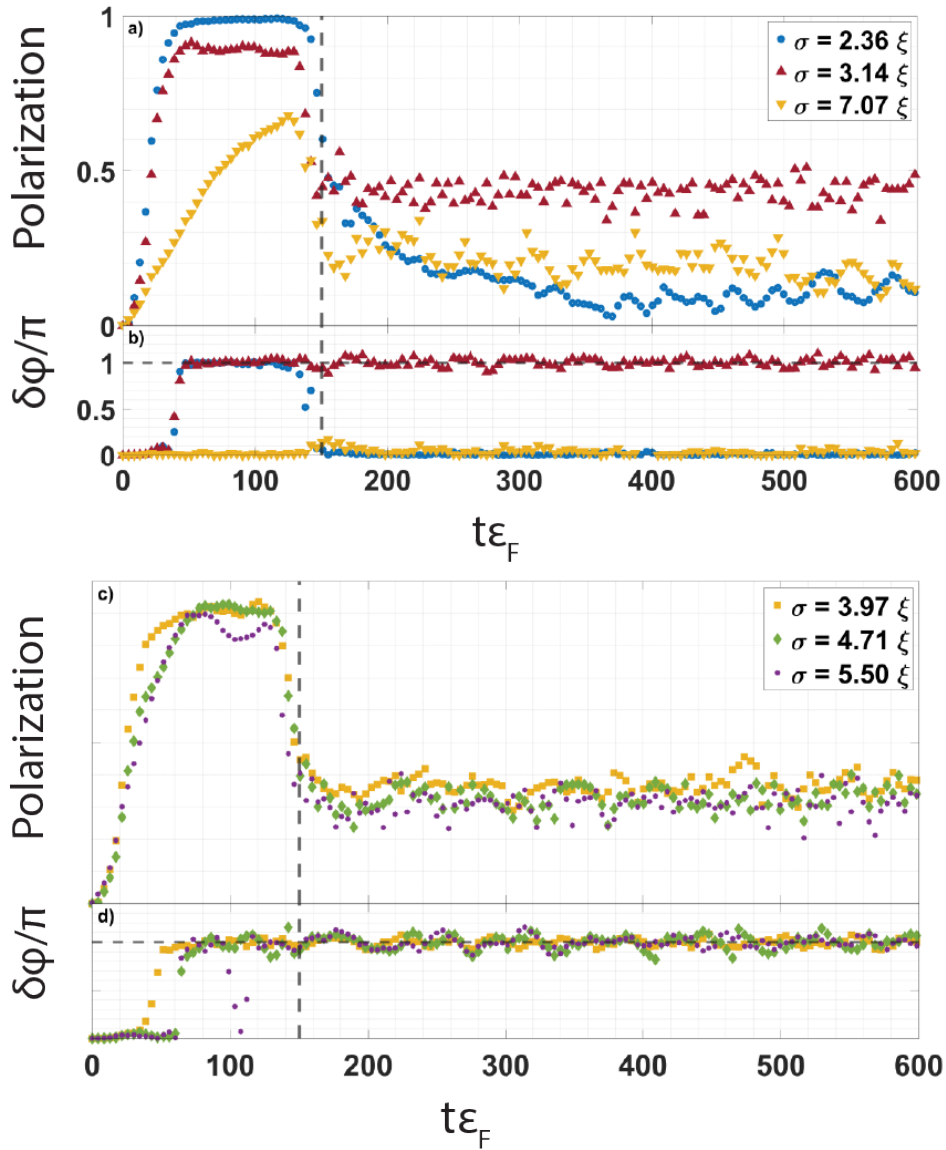


FIGURE 4.5: The time evolution of the ferron is presented. The box size is  $L = 31.42\xi$ . **Upper subfigure:** Small, medium, and large potential widths are compared. In panel a), the local polarization from the center of the box is presented. In panel b), the phase difference between the center of the box and the bulk is shown. It can be seen if the potential is too narrow ( $\sigma = 2.36\xi$ ), the nodal shell does not survive. In the case of wide potential ( $\sigma = 7.07\xi$ ), the given system parameters, such as the amplitude of the potential or the application duration, are not enough to break enough Cooper pairs to create a phase shift. **Upper subfigure:** The stability of the ferron in intermediate potential sizes are shown. The presentation of the results is the same as the above subfigure.

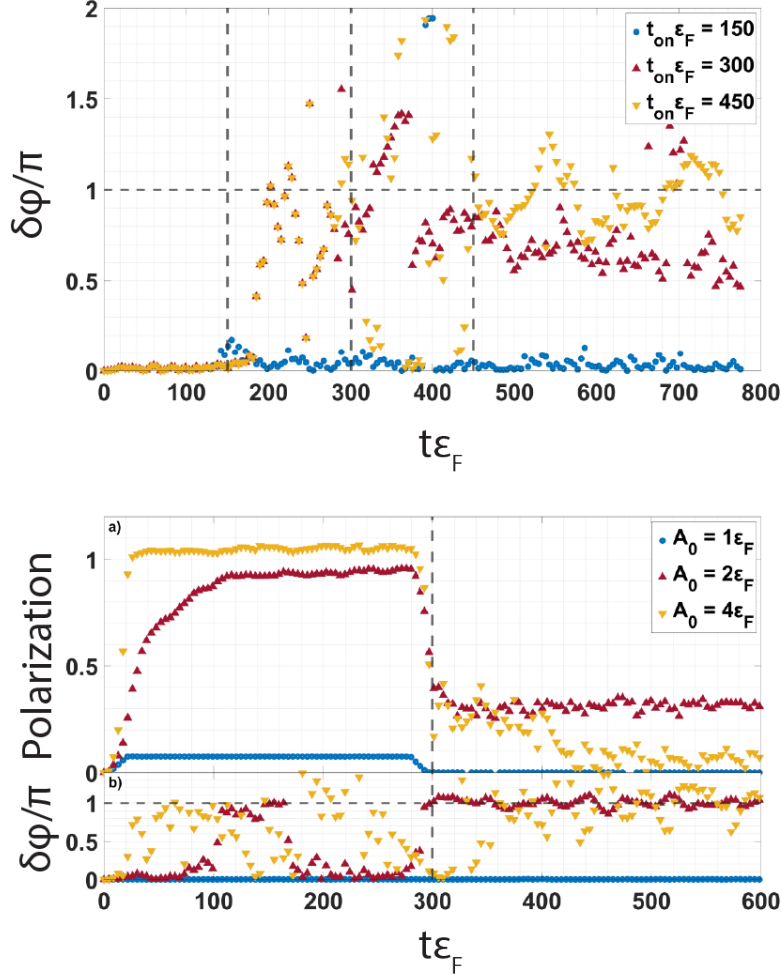


FIGURE 4.6: **Upper subfigure:** The effect of the duration of the application of the external potential is presented. The amplitude of the potential is  $A_0 = 2\varepsilon_F$  and the width is  $\sigma = 7.07\xi$ . It can be seen that for wide potentials, increased duration of the application helps to break enough Cooper pairs to create the necessary shift in the phase between the core and the bulk. The vertical dashed lines represent the time where the external potential is completely turned off for different cases. The horizontal dashed line is a guide to the eye, showing  $\delta\varphi = \pi$ . **Lower subfigure:** The effect of the amplitude of the external potential. The box size is  $L = 37.7\xi$ , and the width is  $\sigma = 4.71\xi$ . Panel a) shows the local relative polarization, and panel b) shows the phase difference from the center of the box to the bulk value. Among three selected amplitudes, only  $A_0 = 2\varepsilon_F$  produces a stable ferron. The vertical dashed line represents when the external potential is completely turned off ( $t\varepsilon_F = 150$ ).

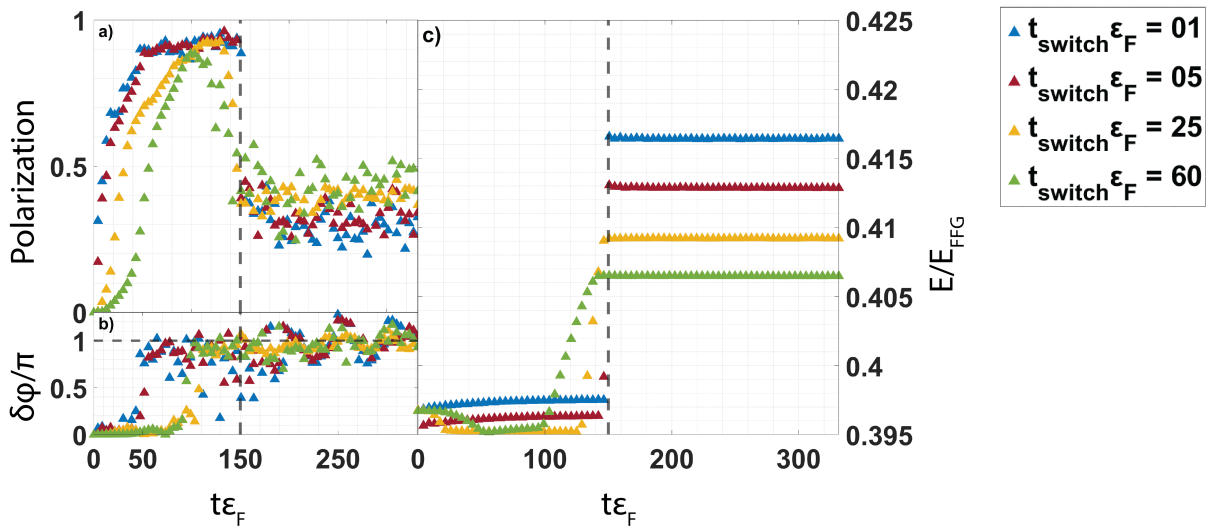


FIGURE 4.7: The creation of ferron with different switching on/off rates,  $t_{switch}$ . Panel a) shows the local polarization in the core of the potential with respect to the bulk. Panel b) shows the phase difference. In panel c) the effect of different switching on/off rates is presented. It can be seen that in all cases, a stable ferron is successively produced. The vertical dashed lines represent the time where the external potential is completely turned off ( $t\varepsilon_F = 150$ ), and the horizontal dashed line is a guide to the eye, showing  $\delta\varphi = \pi$ .

the time-dependent Bogoliubov de-Gennes (TDBdG) approach since TDASLDA is not suited for the 1D case. TDBdG equations are:

$$i\frac{\partial}{\partial t} \begin{pmatrix} u_{n,\lambda}(x,t) \\ v_{n,-\lambda}(x,t) \end{pmatrix} = \begin{pmatrix} h_\lambda(x,t) & \lambda\Delta(x,t) \\ \lambda\Delta(x,t)^* & -h_{-\lambda}^*(x,t) \end{pmatrix} \begin{pmatrix} u_{n,\lambda}(x,t) \\ v_{n,-\lambda}(x,t) \end{pmatrix}, \quad (4.4)$$

where  $\lambda = \pm 1$  denotes spin indices,  $h_\lambda(x,t) = -\frac{1}{2}\frac{d^2}{dx^2} + gn_{-\lambda}(x,t) + V_\lambda(x,t)$  and  $\Delta(x,t) = gv(x,t)$  ( $n_\lambda$  is the density of spin- $\lambda$  particles,  $v$  is the anomalous density). The coupling constant  $g$  has been adjusted to obtain the pairing strength in unitary regime:  $\Delta/\varepsilon_F \approx 0.5$ ,  $\varepsilon_F = k_F^2/2$ . In time-dependent 1D calculations, one may generate a similar form of spin-polarized impurity:

$$V_\lambda(x,t) = 1.8f(t)\lambda\varepsilon_F \exp\left(-\frac{x^2}{2\sigma^2}\right), \quad (4.5)$$

where

$$\begin{aligned} f(t) &= \sin^2\left(\frac{\pi t}{2T}\right)\theta(T_1 - t) \\ &+ \theta(t - T_1)\theta(T_2 - t) \\ &+ \cos^2\left(\frac{\pi(t - T_2)}{2T}\right)\theta(t - T_2)\theta(T_1 + T_2 - t), \end{aligned} \quad (4.6)$$

describes the switching-on/off rates.

The results presented in Fig. 4.8 show that the nodal points repel each other. This indicates there is superflow present in the system. A non-zero current implies that the pairing field has a non-zero imaginary part  $\Delta(\mathbf{r}) \sim |\Delta|e^{i\mathbf{q}\cdot\mathbf{r}}$  where  $|\mathbf{j}| \sim q$ . Such form of the pairing field may be attributed to Fulde-Ferrel (FF) type pairing. Note that the polarization effectively travels with the nodal points in opposite directions. In Fig. 4.9 it can be seen that the energy of a system with two polarized nodal points decreases as the distance between those two points increases.

The repulsion of the nodal points in 1D does not happen in 3D simply because expanding the nodal area costs energy. Such an expansion means spontaneous breaking of more Cooper pairs which is not possible since there is no internal mechanism to provide that. Therefore, the ultimate size of the impurity is dictated by the number of broken Cooper pairs due to the external potential. Moreover, as discussed above, the contraction of the nodal shell is prohibited by the pairing field inside. Consequently, the energy of the polarized shell can be written as an interplay between a surface term,  $E_{\text{shell}}$  and a volume term,  $E_{\text{vol}}$ :

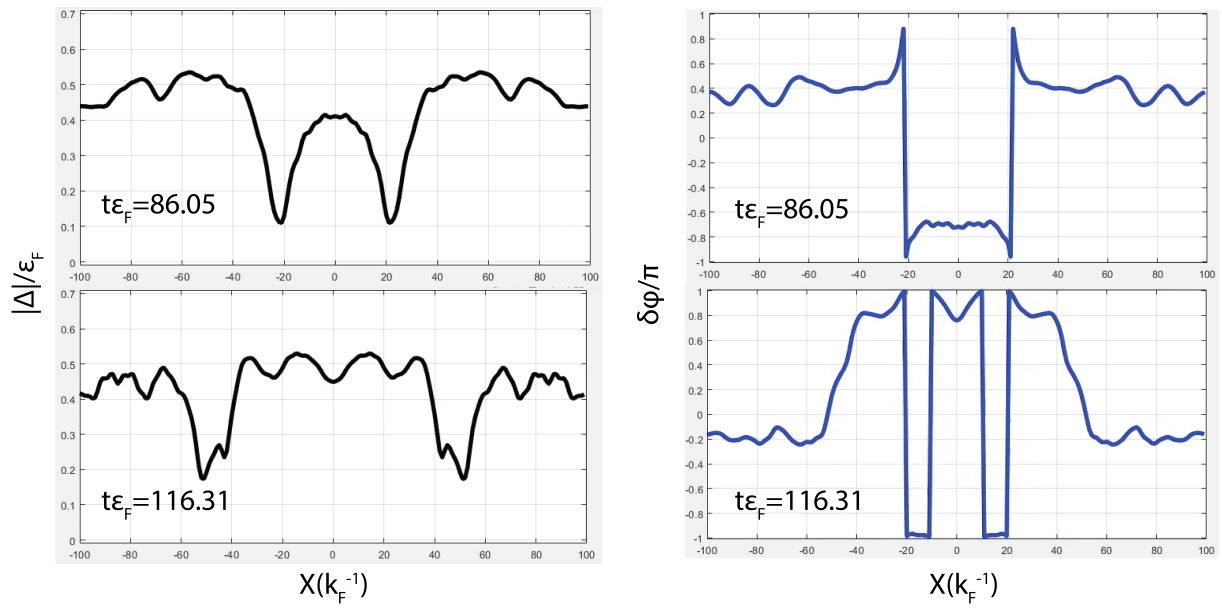


FIGURE 4.8: The snapshots of time-dependent 1D calculations. The left-hand side shows the strength of the pairing field relative to the Fermi energy. The right-hand side shows the phase of the pairing field in units of  $\pi$ . The parameters used in Eq. (4.4) are  $k_F\sigma = 4.441$ ,  $T = T_1 = 29.55\epsilon_F^{-1}$ , and  $T_2 = 49.25\epsilon_F^{-1}$ . The external potential is completely turned off at  $t\epsilon_F = 78.8$ . Both snapshots are taken after the external potential is turned off.

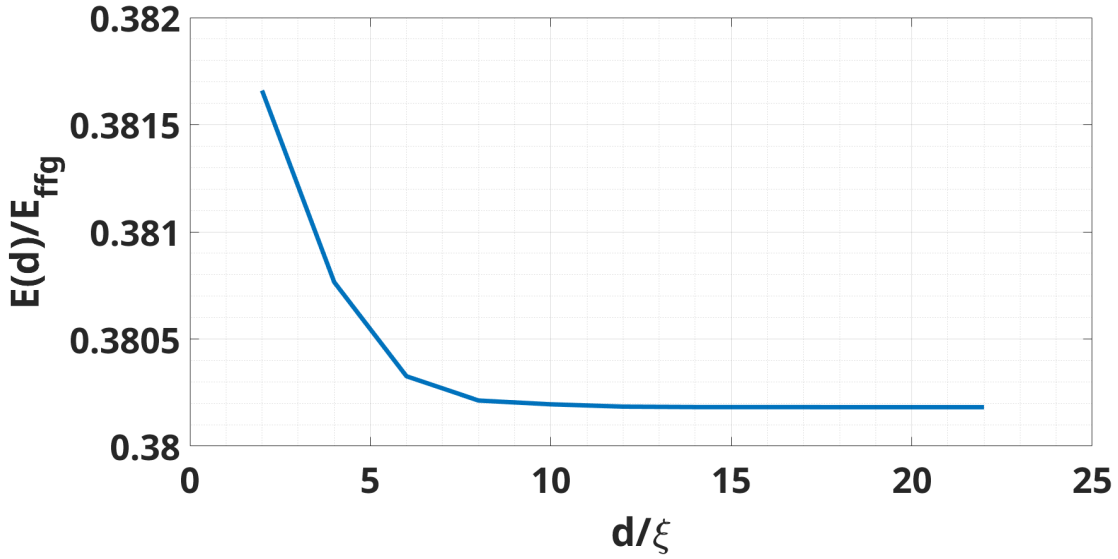


FIGURE 4.9: The energy of the 1D system with the presence of two nodal points. On the x-axis, the distance between two nodal lines in units of coherence length is presented. Y-axis shows the total energy of different configurations with respect to the free Fermi gas. It can be seen that the energy decreases as the distance between the nodal points increases.

$$E_{\text{ferron}} = E_{\text{shell}} + E_{\text{vol}}. \quad (4.7)$$

The stability of the nodal shell is the direct consequence of the polarized population it harbors. Otherwise, in an unpolarized scenario, where the phase difference is imprinted, the nodal shell would decay as there is no mechanism to prevent that. The origin of the nodal shell is due to the splitting of Fermi spheres belonging to different spin components. Because of the proximity effect, the Andreev levels appear inside the nodal shell. It is the Andreev states occupied by locally polarized particles that keep the nodal shell stable. Therefore, the ferron can be considered as a set of Andreev states responding to the environment as a whole.

It is also necessary that the system is superfluid, and the strength of the pairing field neighboring the nodal shell is comparable on both sides. In scenarios where  $T > T_c$ , the polarized cluster would diffuse simply by obeying the Fick's Law,  $\mathbf{J}_s = -D_s \nabla n_s$ , where  $n_s(\mathbf{r}) = n_\uparrow(\mathbf{r}) - n_\downarrow(\mathbf{r})$  is the spin density,  $\mathbf{J}_s$  is the spin current, and  $D_s$  is the spin diffusion coefficient. The existence of the pairing field provides a natural potential barrier, which provides the Andreev levels that keeps the polarized population inside the nodal shell. It should be noted that the external potential is applied only for a limited

time amount to break the Cooper pairs and generate the nodal shell. Provided that it is not a "violent" potential, it does not affect the stability of the impurity after the external potential is turned off. The ferron is solely a result of spin-polarized superfluid system properties, i.e., the only needed ingredients are the spin-imbanced particles to occupy the Andreev states and the pairing field, which prevents the object from collapse. As discussed above, in 1D, where the pairing field has an FF-like structure,  $\Delta(x) \sim |\Delta|e^{iqx}$ , the nodal points are unstable. On the other hand, in 3D and 2D, as we shall discuss, the pairing field has a Larkin–Ovchinnikov (LO) type of structure,  $\Delta(\mathbf{r}) \sim |\Delta| \cos(\mathbf{q} \cdot \mathbf{r})$  which does not induces currents as in FF case. Therefore, from this perspective, the ferron can be considered as a LO droplet. Another note is the dynamic creation of the ferron results in an excited system. Therefore, it does not suggest a local minimum in the free energy. Instead, by stability, what is meant is a long-living configuration without any sign of decay.

## 4.2 Basic dynamic properties of ferron

### 4.2.1 Deformed ferron

The deformation parameters,  $\epsilon_y$ , and  $\epsilon_z$  used in Eq. (4.1) do not provide a visible structural change when kept relatively minimum. By changing the parameters, it is possible to create an initially deformed ferron. To achieve that, the parameters are set to  $\epsilon_y = 0.44$ , and  $\epsilon_z = 0.64$ . Fig. 4.10 (left subfigure) shows the time-evolution of such configuration. It can be seen that the nodal shell is initially deformed as with the external potential. After the potential is turned off, it is observed that the deformed impurity eventually forms a spherically symmetric configuration, aside from losing its stability. The reason is simply an elliptic configuration has both increased surface and curvature, which results in higher energy. During its time evolution, a deformed ferron rearranges itself into a spherical form to decrease its energy.

### 4.2.2 Concentric ferrons

Studies in SFS junctions show that the pairing field may change its sign multiple times depending on the width of the ferromagnet layer [40, 85]. Since ferron is analogous to the SFS junctions, a similar effect is expected. To examine this effect, a wider Gaussian potential is applied. In Fig. 4.10 (right subfigure), it is visible that after the removal

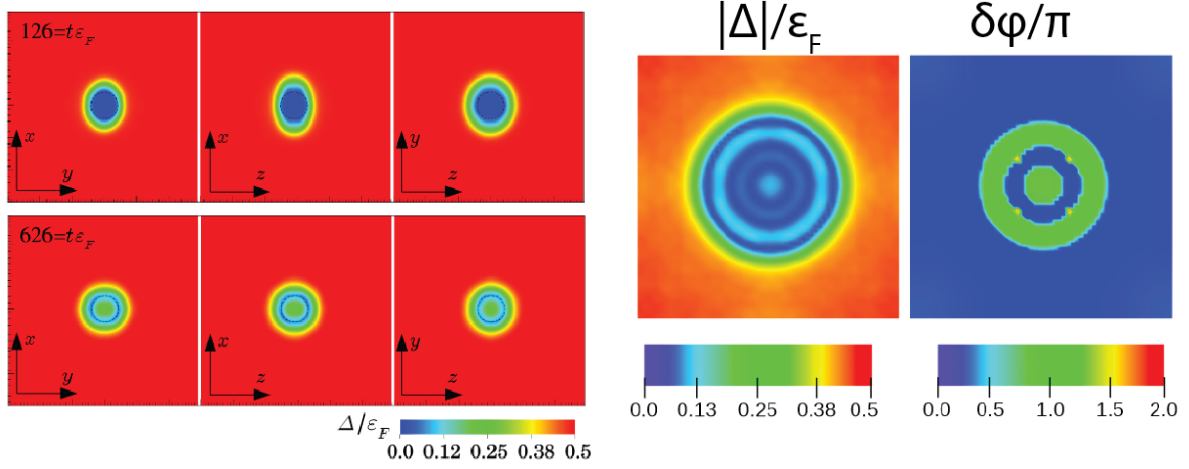


FIGURE 4.10: **Left subfigure:** Two snapshots on dynamic creation of a deformed ferron. The box size is  $L = 47.12\zeta$ . The amplitude of the Gaussian potential is  $A_0 = 2\varepsilon_F$  with the width of  $\sigma = 4.71\zeta$ . The spherical shape is deformed by the parameters  $\varepsilon_y = 0.44$ , and  $\varepsilon_z = 0.64$  used in Eq. (4.1). The top and bottom rows show the cross sections of the pairing field along three perpendicular planes. The top row shows the configuration just before the external potential is turned off. The bottom row shows the initially deformed impurity rearranges itself to a spherical form. The black dashes are guide to the eye. **Right subfigure:** Snapshot of the attempt on creating concentric ferrons. The images are taken at  $t\varepsilon_F = 392$  which is approximately  $220t\varepsilon_F$  after the potential is turned off. The box size is  $L = 50.26\zeta$ . The amplitude the width of the potential are  $A_0 = 3.5\varepsilon_F$  and  $\sigma = 11.78\zeta$  respectively. Both figures are taken from Ref. [46].

of the external potential, the pairing field changes its sign multiple times. However, as discussed above, the process of inducing such a large ferron, with respect to the box size, generates phonon excitations that interact with the impurity. The box size considered is  $L = 50.26\zeta$  and the width of the potential is  $\sigma = 11.78\zeta$ . In order to study the dynamic creation of concentric ferrons in detail, a much larger box is needed.

### 4.2.3 Collision of two ferrons

It is possible to create a moving ferron by dragging the potential along a selected axis. To drag the polarizing potential, Eq. (4.1) is modified in the following way:

$$V_s(\mathbf{r}, t) = \lambda_s A(t) \exp \left[ -\frac{(x_0 + v_{\text{drag}}t)^2 + y^2 + z^2}{2\sigma^2} \right], \quad (4.8)$$

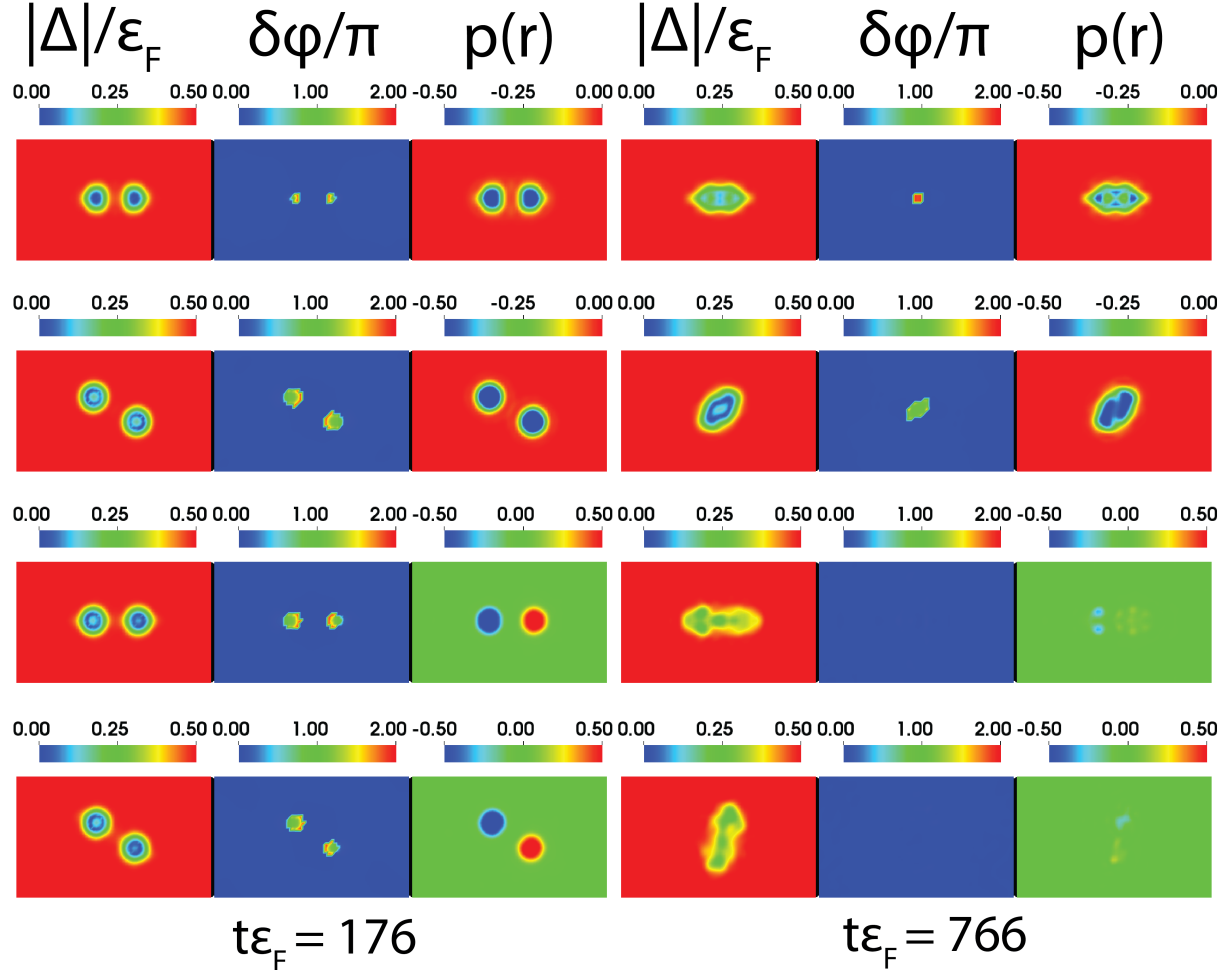


FIGURE 4.11: Four scenarios of ferron collision. In all cases, the box size is approximately  $50 \times 31 \times 31 \zeta^3$ . The width of the polarizing potentials is  $\sigma = 3.14 \zeta$  with the amplitude  $A_0 = 2\varepsilon_F$ . The external potentials move towards each other with the velocity  $v = 0.45v_F$ . The potentials are completely removed at  $t\varepsilon_F = 150$ . On left-hand side the configurations right after the potentials are removed are presented. On the right-hand side the configurations at  $t\varepsilon_F = 766$  can be seen. The first row shows the head-on collision of two identical ferrons. The second row shows the peripheral collision of identical ferrons. The third row consists head-on collision of ferrons of opposite polarization. Finally the fourth row shows the peripheral collision of ferrons of opposite polarization.

where  $v_{\text{drag}}$  sets the velocity that the potential is dragged. After the external potential is removed from the system, the ferron continues its motion with a slower velocity which drags the potential. This drop in the velocity is due to the removal of the external potential.

In Fig. 4.11 four different scenarios for ferron collision are presented: 1) Head-on collision of identical ferrons. 2) Peripheral collision of identical ferrons. 3) Head-on collision of ferrons of opposite polarization. 4) Peripheral collision of ferrons of opposite polarization. The robust structure of the ferron can be seen from the collisions of identical ferrons. In both cases, nodal shells fuse and create a bigger, single ferron. This new configuration is initially deformed. However, from the above studies, one may expect that the deformed ferron eventually will rearrange itself into a spherical shape. This process is technically difficult to capture since the superfluid background is highly excited after the creation and dragging of two ferrons.

It is also possible to examine the collision of two oppositely polarized ferrons. In such a scenario, Fig. 4.11 shows the ferrons annihilate each other. It can be seen that the superfluid gas has almost returned to its initially spin-balanced uniform configuration, and the nodal shells are destroyed.

## 4.3 Robustness of the phenomenon

### 4.3.1 TDASLDA vs TDBdG

The creation and the stability of the ferron are related only to the pairing field and the spin imbalance. It is not a trademark of a particular framework. The study of time-dependent creation of ferron has been done within the TDASLDA framework, which has been tested numerous times for spin-polarized UFG [79, 86, 87]. To show that the creation of the ferron does not depend on a particular method, a comparison with the TDBdG approach has been made. To induce the nodal shell, the same method as above (Eq. (4.1)) has been used. It is confirmed that a ferron can be created within the TDBdG approach (see Fig. 4.12). The only difference between the two methods comes from the amplitude of the external potential. The maximum strength for the external potential that is typically used in the TDASLDA approach,  $A_0 = 2\varepsilon_F$ , creates stronger phonon excitations in the TDBdG approach. This eventually leads to an unstable configuration. Therefore, to obtain a stable configuration, the maximum amplitude of the external

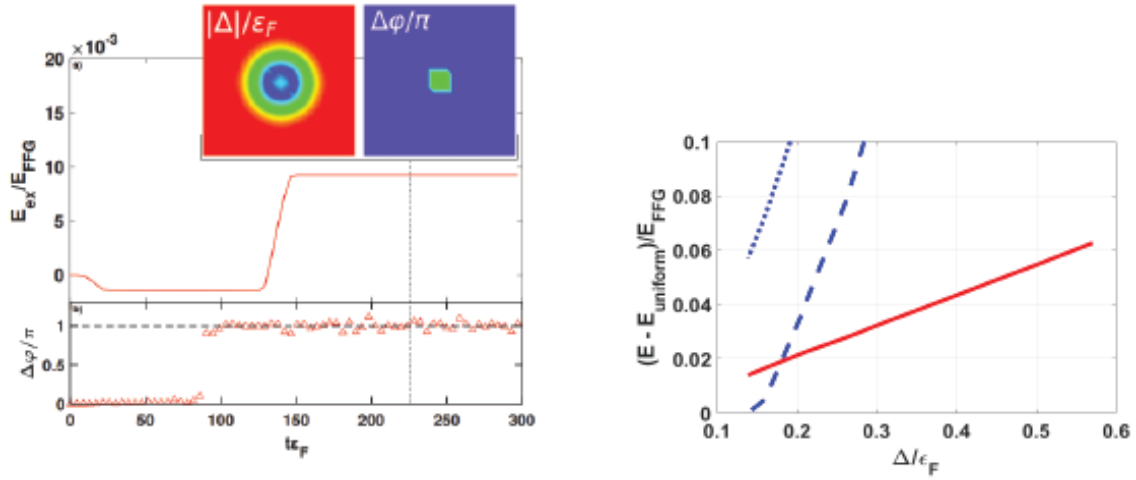


FIGURE 4.12: **Left subfigure:** The ferrons existence and stability under the BdG approach is shown. The box size is  $L = 31.42\zeta$ . The maximum strength of the potential is  $A_0 = 1.5\epsilon_F$  and the width of the Gaussian potential is  $\sigma = 4.71\zeta$ . The potential is applied from the beginning until  $t\epsilon_F = 150$ . The total excitation energy ( $E_{ex} = E(t) - E(0)$ ) and the phase difference between the bulk and the core  $\delta\varphi/\pi$  are shown as functions of time. The inset shows the internal structure at the time indicated by the dashed line,  $t\epsilon_F \approx 225$ . **Right subfigure:** In 1D calculations the energy cost to keep two nodal lines stable in a polarized system are shown by the red solid line. The dashed lines indicate the pairing energy for the same polarized configuration. The dotted lines show the pairing energy for uniform configuration. Both figures are taken from Ref. [46].

potential is lowered to  $A_0 = 1.5\epsilon_F$ . Besides technical matters, the choice of functional does not affect the ferron's stability.

### 4.3.2 UFG vs BCS

The crucial element to create a ferron is the pair-breaking process. The Chandrasekhar–Clogston limit sets a maximum chemical potential difference between spin components, where the superfluidity still persists [39]:

$$\tilde{\mu} = \frac{(\mu_{\uparrow} - \mu_{\downarrow})}{2} = \frac{\Delta_0}{\sqrt{2}}, \quad (4.9)$$

where  $\Delta_0$  is the strength of the pairing field in an unpolarized case. Higher values of the chemical potential difference result in a first-order phase transition from a superfluid to a normal phase. Eq. (4.9) implies that the maximum polarization that can

be induced in a system is related to the strength of the pairing field. Since the unitary regime has the strongest pairing among Cooper pairs, according to Eq. (4.9) one may induce high values of chemical potential difference, therefore, spin-polarization without destroying the superfluidity.

However, the creation of ferron is not limited to the UFG regime. Fig. 4.12 shows that as the system goes from strong coupling to weak coupling regime, the energy cost to induce ferron scales linearly,  $E_{\text{ferron}} \sim |\Delta|$ . On the other hand, the condensation energy scales as  $E_{\text{cond.}} \sim |\Delta|^2$  which is overcome by the energy to induce ferron in the weak coupling regime.

Moreover, a weaker pairing means a larger coherence length. Since the minimum size of the ferron is on the order of several coherence lengths, studies in the deep-BCS regime would require larger simulation boxes. This effect sets a technical limit on 3D time-dependent studies. In conclusion, a strong coupling regime is found to be more robust to create ferrons.



# Chapter 5

## The internal structure of the ferron

### 5.1 Andreev states inside the ferron

The ferron consists of particles of the same spin occupying the Andreev states inside a nodal region where the superfluid pairing field changes its sign. The Andreev states in a superconductor–normal–superconductor junction are described by Eq. (2.82). It is possible to extend the formula for the spin–imbalanced case, i.e.,  $\mu_\uparrow \neq \mu_\downarrow$ :

$$\frac{E_{\pm,n}}{|\Delta|} \frac{d}{2\xi} - 2 \arccos \frac{E_{\pm,n}}{|\Delta|} + \delta\varphi = 2\pi n, \quad (5.1)$$

where  $E_{\pm,n} = E_n \pm \frac{\delta\mu}{2}$ ,  $\delta\mu = \mu_\uparrow - \mu_\downarrow$ , and  $d$  is the distance which the particle travels inside the normal part, from one superconductor boundary to the other. In a 2D ultracold Fermi gas, the nodal region has the shape of a circular ring (see Fig. 5.1). As it can be seen at Fig. 5.1 (right subfigure), the Andreev reflection inside the ferron should be considered in two different regions, since the phase difference  $\delta\varphi$  may be either  $\pi$  or 0. Therefore, Eq. (5.1) should be considered separately in those regions:

$$\frac{E_{\pm,n}}{|\Delta|} \frac{d_0}{2\xi} - 2 \arccos \frac{E_{\pm,n}}{|\Delta|} = 2\pi n, \quad (5.2)$$

$$\frac{E_{\pm,n}}{|\Delta|} \frac{d_\pi}{2\xi} - 2 \arccos \frac{E_{\pm,n}}{|\Delta|} = \pi(2n - 1), \quad (5.3)$$

where,  $d_\pi$  denotes the trajectory length where  $\delta\varphi = \pi$  and  $d_0$  denotes the trajectory length where  $\delta\varphi = 0$ :

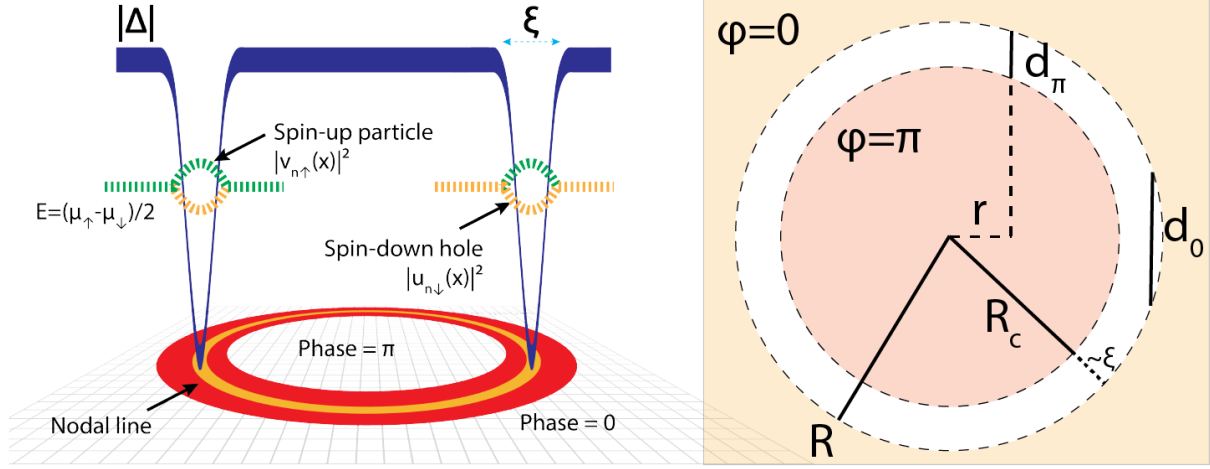


FIGURE 5.1: **Right subfigure:** A 2D schematic of ferron. The Andreev states are localized at the vicinity of the nodal line (red area), where the phase of the pairing field shifts by  $\pi$ . The image is taken from Ref. [88]. **Left subfigure:** A 2D schematic demonstrating two different semi-classical trajectories for particles occupying Andreev states.

$$d_0 = 2\sqrt{R^2 - r^2}, \quad (5.4)$$

$$d_\pi = \sqrt{R^2 - r^2} - \sqrt{R_c^2 - r^2}. \quad (5.5)$$

Here  $R_c$  is the radius which the phase is shifted by  $\pi$ ,  $R$  is the total radius of the ferron, and  $r$  is the radial distance of the trajectory. It is instructive to associate each trajectory with angular momenta:

$$\mathbf{L} = \mathbf{r} \times \mathbf{p}, \quad (5.6)$$

where  $\mathbf{p}$  is the momentum. Hence, the angular momentum, which is perpendicular to the plane where the ferron resides, can be expressed as:

$$L_z = \hbar k_F r. \quad (5.7)$$

Here, we assume the quasiparticle momenta are on the order of Fermi momentum as a result of the Andreev approximation. Consequently, the trajectory lengths in Eq. (5.4) can be rewritten in terms of angular momenta:

$$\begin{aligned}\frac{d_0}{4\zeta} &= \frac{R}{2\zeta} \sqrt{1 - \frac{L_z^2(r)}{L_{\max}^2}}, \\ \frac{d_\pi}{4\zeta} &= \frac{R\sqrt{1 - \frac{L_z^2(r)}{L_{\max}^2}} - R_c\sqrt{1 - \frac{L_z^2(r)}{L_c^2}}}{4\zeta},\end{aligned}\quad (5.8)$$

where  $L_{\max} = k_F R$ , and  $L_c = k_F R_c$ . Hence, it is possible to rewrite Eq. (5.1) explicitly for these two regions:

$$x_n \alpha_0 - \arccos x_n = \pi n, \quad (5.9)$$

$$x_n \alpha_\pi - \arccos x_n = \pi \left( n - \frac{1}{2} \right), \quad (5.10)$$

where  $x_n = E_{\pm,n}/|\Delta|$ ,  $\alpha_\pi = d_\pi/4\zeta$ , and  $\alpha_0 = d_0/4\zeta$  are introduced to simplify the equations to a dimensionless manner. At first inspection, it can be seen that for the former equation, the solutions come in pairs of  $x_n = -x_{-n-1}$  and for the latter one  $x_n = -x_{-n}$  (where  $n \geq 0$ ).

Fig. 5.2 (left subfigure) shows the solutions of Eq. (5.9) for various  $n$  values. This region, where  $\delta\varphi = 0$ , admits angular momenta,  $L_z$ , ranging from  $L_c$ , to  $L_{\max}$ . Therefore, the dimensionless parameter  $\alpha_0$  has values from 0 to  $\sqrt{R/2\zeta}$  (see inset of Fig. 5.2). The limit,  $\alpha_0 = 0$  is the high-energy limit where the length of the junction is negligible. In this limit, Eq. (5.9) yields to a trivial result:  $E_{\pm,n} = |\Delta|$ . The low energy limit, where  $E_{\pm,n} \ll |\Delta|$ , corresponds to the case where  $\alpha_0 \gg 1$ . This, implies the large ferron limit, where  $R \gg \zeta$ . In this limit, the inverse trigonometric function in Eq. (5.9) can be written as  $\arccos x \approx \pi/2 - x$ . Therefore, the Andreev levels are quantized as:

$$\frac{E_{\pm,n}}{|\Delta|} = \frac{\pi}{1 + \alpha_0(L_z)} \left( n + \frac{1}{2} \right). \quad (5.11)$$

The lowest energy solution in the case of a large ferron,  $R_c \gg \zeta$ ,  $\alpha_0 \approx \sqrt{R/2\zeta}$ , and for  $n = 0$ , can be found as:

$$\frac{E_\pm}{|\Delta|} = \frac{\pi/2}{1 + \sqrt{\frac{R}{2\zeta}}}. \quad (5.12)$$

The region where  $\delta\varphi = \pi$  spans a larger area than the previous region. Namely, the

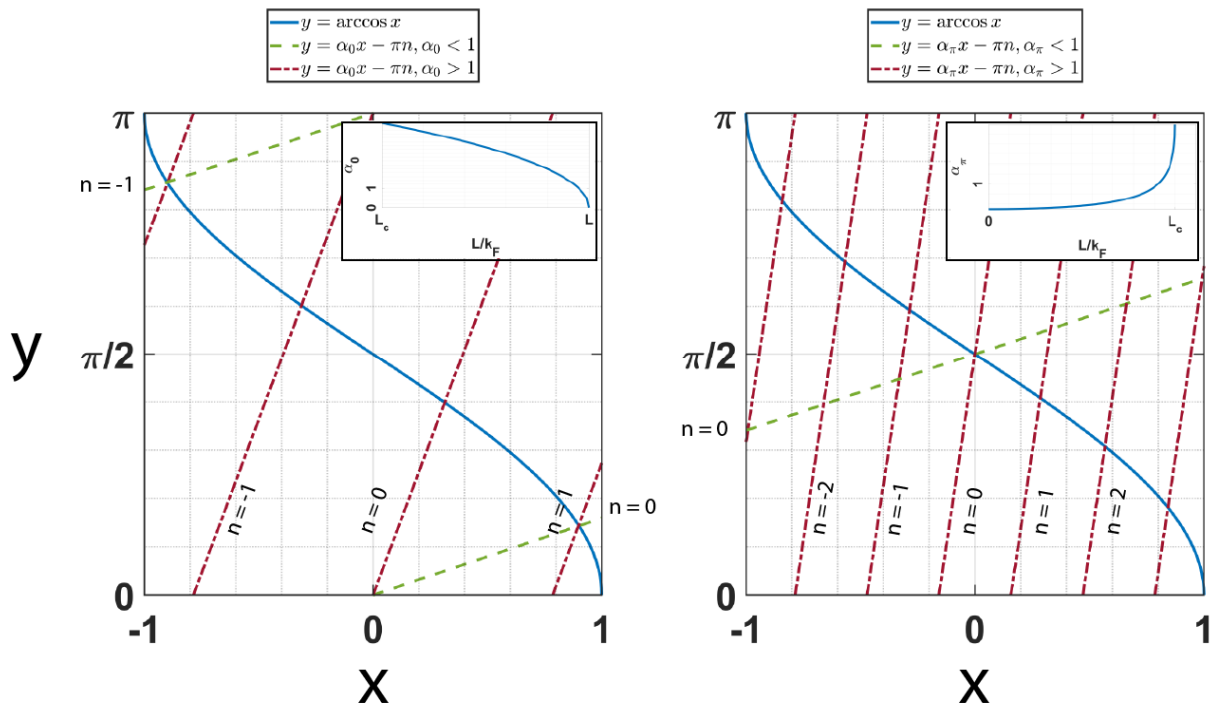


FIGURE 5.2: The solutions for Eq. (5.9) (left subfigure) and Eq. (5.10) (right subfigure). It can be seen that there always exist a solution for both equations. Insets in both figures shows the behavior of the dimensionless parameter,  $\alpha$  as a function of the angular momentum,  $L$ .

angular momentum here ranges from 0 to  $L_c$ . As a result, this region harbors the majority of the Andreev states. In this region, quantization of Andreev states is described by Eq. (5.10). It can be seen that Eq. (5.10) always admits solutions for  $x = 0$ , no matter the angular momentum is (see Fig. 5.2, right subfigure). Therefore, the Andreev states formed within the region where  $\delta\varphi = \pi$  have energies equal to Fermi energy,  $E_n = \varepsilon_F$ . Moreover, in the case where  $\alpha_\pi = \pi/2$ , and  $n = \pm 1$ , the region involves the high energy states where  $E(n = \pm 1) = |\Delta|$ . Fig. 5.2 shows that in the case of  $\alpha_\pi \gg 1$ , there are numerous low energy solutions for Eq. (5.10). By making the approximation,  $\arccos x \approx \pi/2 - x$ , the energy of the Andreev states can be expressed as:

$$\frac{E_\pm}{|\Delta|} = \frac{\pi}{1 + \alpha_\pi(L_z)} n. \quad (5.13)$$

However, as can be seen from the inset of Fig. 5.2,  $\alpha_\pi > 1$  case is valid only at the limiting angular momenta. Therefore, we can conclude that the majority of Andreev states inside the  $\delta\varphi = \pi$  region have energies on the order of the Fermi energy.

## 5.2 The size of the ferron

In the previous chapter, ferron's dynamical creation and stability were verified by means of 3D time-dependent numerical calculations. To study its internal structure and characteristics, we focus on 2D static solutions which can be generalized to the 3D case.

In static calculations, there is no way to break the Cooper pairs, which is a crucial process for the dynamic creation of the ferron. Different from the dynamic case, in the static case, the global polarization,  $P = \frac{N_\uparrow - N_\downarrow}{N_\uparrow + N_\downarrow}$  is non-zero. The nodal circle that hosts the unpaired particles is imprinted inside the simulation box by hand. The phase difference  $\pi$  is achieved by forcing the pairing field to have the following form:

$$\Delta(\mathbf{r}) = \begin{cases} -\Delta, & r < R_1, \\ \Delta, & R_2 < r. \end{cases} \quad (5.14)$$

Above procedure creates a nodal line in between  $R_1$  and  $R_2$ . Consequently, the unpaired particles occupy the Andreev states inside this nodal line. The static solutions are obtained by minimizing the quantity:

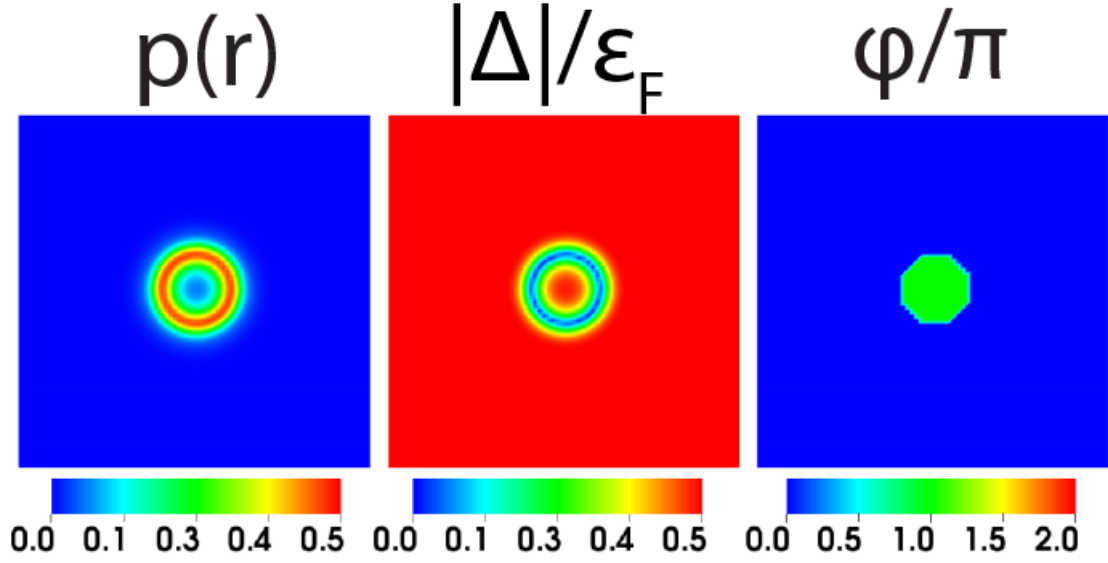


FIGURE 5.3: The ground state configuration of the ferron. From left to right, the local polarization, the strength of the pairing field, and the phase of the pairing field are shown. The figure is taken from Ref. [88].

$$\langle \Omega \rangle = \left\langle H - \sum_{\sigma=\{\uparrow,\downarrow\}} \mu_{\sigma} N_{\sigma} \right\rangle. \quad (5.15)$$

The condition in Eq. (5.14) is only applied for a couple of iterations during the minimization. Once the unpaired particles settle on the nodal line, the condition is not needed anymore. Therefore, after a couple of iterations, it is turned off.

The ground state configuration of a 2D ferron is shown in Fig. 5.3. It can be seen that the strength of the pairing field is completely recovered in the center. This was not typical in a time-dependent scenario since there are always scattering events due to excited phonons. As a result of the healing in the pairing field, the polarization in the center of the nodal circle vanishes.

To investigate the relationship between the ferron's size and spin-imbalance, a series of calculations with different global polarizations have been made. Using the imprinting method given in Eq. (5.14), the system settles to a nodal radius in between  $R_1 = 3k_F^{-1}$  and  $R_2 = 25k_F^{-1}$ . As shown above, the number of Andreev states inside the ferron is governed by the object's size. The increase in the spin-imbalance creates the necessity for more Andreev states to be occupied. Therefore, an increase in the spin-imbalance causes an expansion in the size of the ferron.

In panel a) of Fig. 5.4, it can be seen that for a small ferron, the pairing is not able

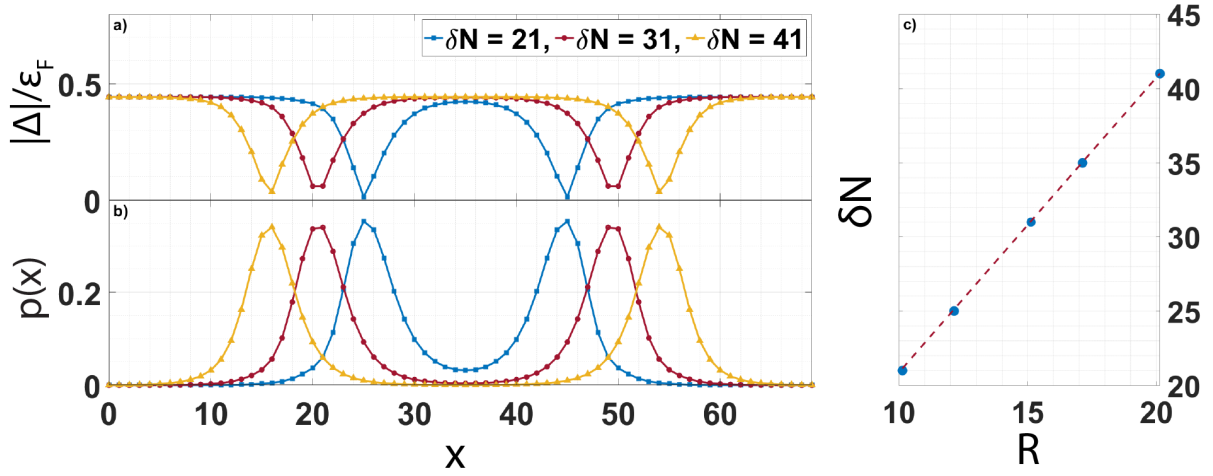


FIGURE 5.4: A 1D cross-section of the simulation box. Panel a) and b) show the local polarization and magnitude of the pairing field for different global polarization values. Panel c) shows the radius of the nodal circle for different global polarization values. The blue dots are the radii extracted from the system. The dashed red line shows the linear equation,  $2k_F R + 1$  where  $R = R_c + \xi$ .

to recover itself to its full strength, which causes non-zero polarization in the center. Panel b) of the same figure shows that there are no unpaired particles in bulk. In the case of a large ferron, all unpaired particles occupy the vicinity of the nodal circle. Panel c) of Fig. 5.4 shows that there is a linear relationship between the number of the unpaired particles and the radius of the nodal circle.

Panel c) of Fig. 5.4 compares the radius ( $R$ ) obtained from numerical calculations to simple analytic estimation. The angular momentum states inside the ferron obtain values from  $-k_F R$  to  $k_F R$ . These states can be labeled by the magnetic quantum number,  $m$ , which they possess due to the quantization of the angular momentum. The magnetic quantum numbers are defined as:

$$m = \frac{\langle L_z \rangle}{\int d^2r |v(\mathbf{r})|^2}. \quad (5.16)$$

During the Andreev scattering, the particle which is reflected as a hole conserves its angular momentum. This would not be the case in a regular reflection where a particle-hole conversion has no place. The magnetic quantum number,  $m$ , is a "good quantum number" which is conserved during the retroreflection. Therefore, it can be used to label the Andreev states inside the ferron.

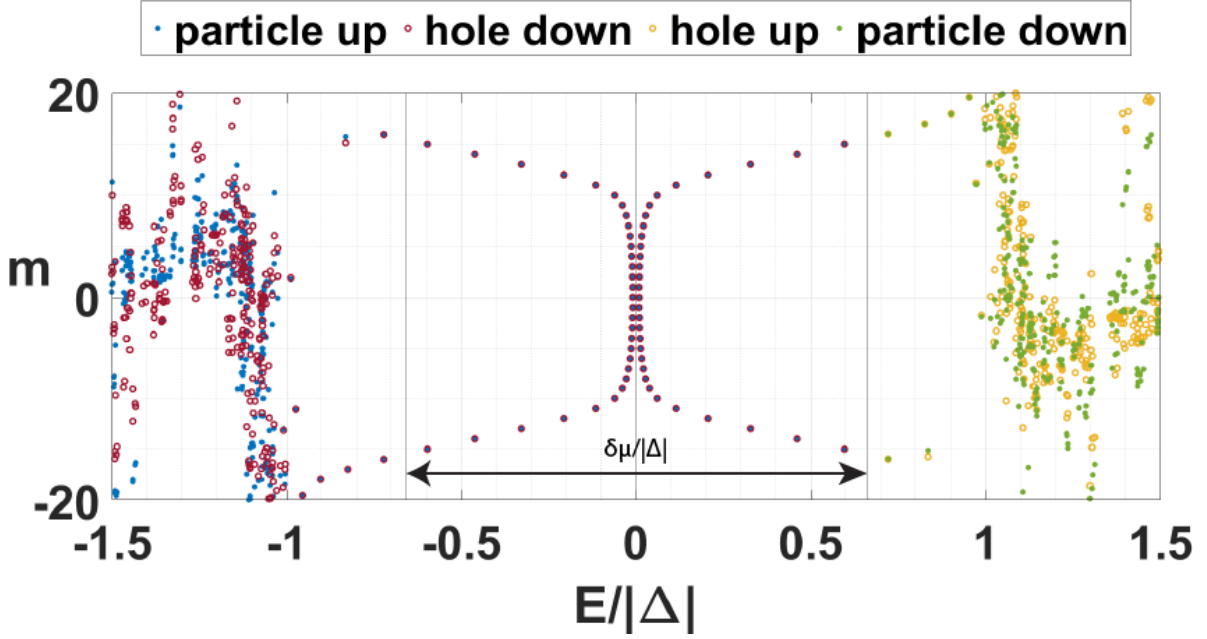


FIGURE 5.5: The angular momentum states inside the ferron ( $m$ ). The energy is shifted by  $\delta\mu/(2|\Delta|)$ . The vertical lines show the values of  $-\delta\mu/(2|\Delta|)$  and  $\delta\mu/(2|\Delta|)$ . The box size is  $70k_F^{-1} \times 70k_F^{-1}$ . The spin-imbalance is  $\delta N = 31$ . The strength of the pairing field is  $|\Delta|/\varepsilon_F \approx 0.44$ .

The magnetic quantum number obtains integer values from  $-k_F R$  to  $k_F R$ . In the 2D case, the number of angular momentum states is  $2k_F R + 1$ . Because of the symmetry of BdG equations, there is another branch of states for negative energies. In the spin-imbanced case, this symmetry is shifted by  $\delta\mu/2$  (see Fig. 5.5). This second branch adds another contribution of  $2k_F R + 1$  to the number of states. However, the occupation of Andreev states is  $|u_\uparrow|^2 = |v_\downarrow|^2 = 1/2$  (see Eq. (2.85)). Therefore, each angular momentum state is occupied by roughly half of a particle, meaning that the radius of a 2D ferron scales with the number of excess particles in a linear fashion:

$$\delta N = 2k_F R + 1 = 2L_{\max} + 1. \quad (5.17)$$

Fig. 5.4 compares the radius obtained by numerical solution of BdG equations and the analytical estimation made by Andreev approximation. It can be seen that the slope of the data agrees with the analytical estimations.

In 3D case, the relation in Eq. (5.17) becomes quadratic since each angular momentum eigenstate comes with a degeneracy of  $2l + 1$ :

$$\delta N = \sum_{L_z=0}^{L_{\max}} (2L_z + 1) = (L_{\max} + 1)^2. \quad (5.18)$$

### 5.3 Semi-classical analysis of ferron

In numerical calculations, the angular momentum states inside the ferron are degenerate. To lift the degeneracy, a small perturbation is implemented to the system after the self-consistent solution is obtained. It is done by adding the additional term,  $\omega \hat{L}_z$  to the single-particle part of the BdG Hamiltonian:  $h_{\uparrow\downarrow}(\mathbf{r}) = -\frac{1}{2}\nabla^2 - \tilde{\mu}_{\uparrow\downarrow} - i\omega\mathbf{r} \times \nabla$ . Here,  $\omega$  stands for the radial frequency and is typically set to  $\omega \approx 0.01\varepsilon_F$ . Fig. 5.5 shows the solutions of BdG Hamiltonian. Their magnetic quantum numbers label the energy levels. The energies are shifted by  $\delta\mu/2$ . Therefore, the eigenvalues are symmetrical around  $E = 0$ . The continuum states, occupied by the Cooper pairs, are where  $|E| \geq |\Delta|$ . It can be seen that for energies below  $\delta\mu/2$ , the solutions correspond to  $(u_{\downarrow} \ v_{\uparrow})^T$  eigenstates. For energies above  $\delta\mu/2$ , the solutions correspond to  $(u_{\uparrow} \ v_{\downarrow})^T$  eigenstates.

To verify the agreement between numerical calculations and semi-classical approximation (the solutions of Eq. (5.9) and Eq. (5.10)), ferrons of different sizes ranging from  $R = 10k_F^{-1}$  to  $20k_F^{-1}$  are investigated. Therefore, according to Eq. (5.17) the smallest ferron is obtained by the global spin-imbalance  $\delta N = 21$  and the largest one with  $\delta N = 41$ . The upper subfigure of Fig. 5.6 shows that the agreement between the numerical results and semi-classical approximation is the best in the limit of the large ferron. As a solution of Eq. (5.10), low angular momentum states have energies  $E = 0$ . However, in the case of the small ferron, there is a discrepancy between Andreev approximation and BdG results. This discrepancy can be attributed to a tunneling effect through the ferron interior, where the radius of the ferron is comparable to the coherence length. The effect of the tunneling can be examined in a similar way to the Andreev problem examined in Chapter 2. Instead of considering three regions where the phase is shifted only once, to reveal the tunneling effect, five regions must be considered where the phase is spatially shifted by  $\pi$  twice. Hence, it returns to its original value. A schematic of the problem can be seen in Fig. 5.7. The wave function in the regions 1 and 5 have the following form (see Eq. (2.74) and Eq. (2.75)):

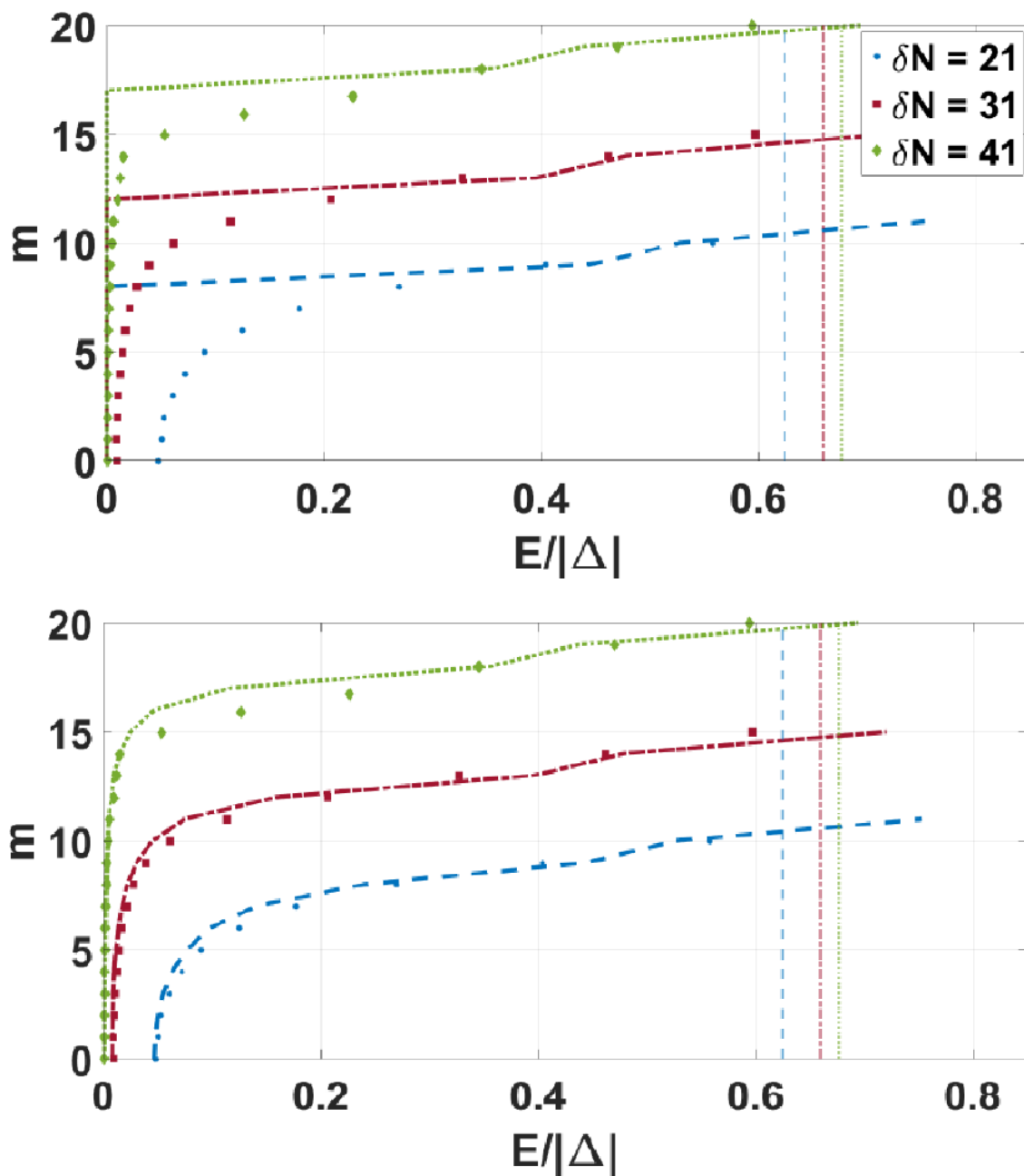


FIGURE 5.6: The positive branch of angular momenta and energies are shown for different sizes of ferron. The dotted values represent the solutions obtained from numerical calculations. The dashed lines show the analytical estimations obtained from the Andreev approximation. The vertical lines show the values of corresponding chemical potentials. The system settings are the same as Fig. 5.5. **Upper subfigure:** The analytical solutions show discrepancy for small ferron sizes. **Lower subfigure:** The discrepancy is treated by considering the tunneling events through the ferron interior.

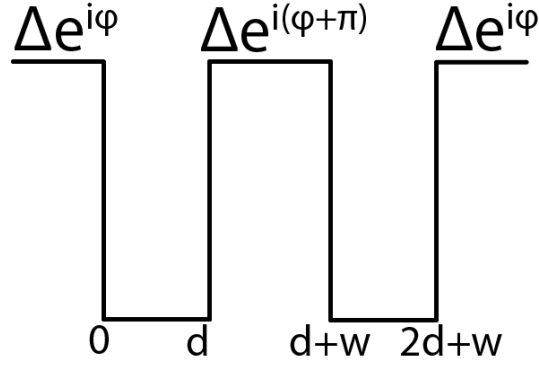


FIGURE 5.7: A schematic of potential wells.  $d$  is the length of the junction where the magnitude of the pairing field drops to zero.  $w$  is the width of the ferron interior where the phase of the pairing field is shifted by  $\pi$ .

$$\Psi_1(x) = \begin{pmatrix} u_1 e^{px} \\ v_1 e^{px} \end{pmatrix}, \quad (5.19)$$

$$\Psi_5(x) = \begin{pmatrix} u_5 e^{-px} \\ v_5 e^{-px} \end{pmatrix}, \quad (5.20)$$

where  $p = \frac{\sqrt{|\Delta|^2 - E^2}}{k_F}$  (see Eq. (2.72)). Eq. (2.70) shows that above equation can be written as the following:

$$\Psi_1(x) = \begin{pmatrix} u_1 e^{px} \\ u_1 e^{px+i\theta} \end{pmatrix}, \quad (5.21)$$

$$\Psi_5(x) = \begin{pmatrix} u_5 e^{-px} \\ v_5 e^{-px-i\theta} \end{pmatrix}, \quad (5.22)$$

where  $\cos \theta = E/|\Delta|$ , and we drop  $e^{ik_F x}$  term for simplicity. The regions 2 and 4 have the same form as Eq. (2.73):

$$\Psi_{2,4}(x) = \begin{pmatrix} u_{2,4} e^{i\frac{E}{k_F} x} \\ v_{2,4} e^{-i\frac{E}{k_F} x} \end{pmatrix}. \quad (5.23)$$

Finally, the region 3 has the form:

$$\Psi_3(x) = \begin{pmatrix} u_{3a}e^{px} + u_{3b}e^{-px} \\ -u_{3a}e^{px+i\theta} - u_{3b}e^{-px-i\theta} \end{pmatrix}. \quad (5.24)$$

Here, it should be noted that in region 3 the phase of the pairing field is shifted by  $\pi$ . The wave functions must be continuous at the boundaries, therefore comparing the regions 1 and 2:

$$\begin{aligned} u_1 &= u_2, \\ v_1 &= v_2 = u_1 e^{i\theta}. \end{aligned} \quad (5.25)$$

Comparing regions 2 and 3:

$$\begin{aligned} u_2 e^{i\frac{E}{k_F}d} &= u_{3a}e^{pd} + u_{3b}e^{-pd}, \\ v_2 e^{i\frac{E}{k_F}d} &= -u_{3a}e^{pd+i\theta} - u_{3b}e^{-pd-i\theta}. \end{aligned} \quad (5.26)$$

Above equations can be re-written using Eq. (5.25):

$$\begin{aligned} u_1 &= u_{3a}e^{pd-i\frac{E}{k_F}d} + u_{3b}e^{-pd-i\frac{E}{k_F}d}, \\ u_1 &= -u_{3a}e^{pd+i\frac{E}{k_F}d} - u_{3b}e^{-pd+i\left(\frac{E}{k_F}d-2\theta\right)}, \end{aligned} \quad (5.27)$$

which yields to:

$$u_{3a} = -u_{3b}e^{-2pd-i\theta} \frac{\cos\left(\frac{E}{k_F}d - \theta\right)}{\cos\left(\frac{E}{k_F}d\right)}. \quad (5.28)$$

Comparing regions 3 and 4 gives:

$$\begin{aligned} u_4 e^{i\frac{E}{k_F}d(d+w)} &= u_{3a}e^{p(d+w)} + u_{3b}e^{-p(d+w)}, \\ v_4 e^{i\frac{E}{k_F}d(d+w)} &= -u_{3a}e^{p(d+w)+i\theta} - u_{3b}e^{-p(d+w)-i\theta}, \end{aligned} \quad (5.29)$$

and the regions 4 and 5:

$$\begin{aligned} u_5 e^{-p(2d+w)} &= u_4 e^{i \frac{E}{k_F} (2d+w)}, \\ u_5 e^{-p(2d+w)-i\theta} &= v_4 e^{-i \frac{E}{k_F} (2d+w)}. \end{aligned} \quad (5.30)$$

After re-writing above equations using Eq. (5.29):

$$u_{3a} = -u_{3b} e^{-2p(d+w)-i\theta} \frac{\cos\left(\frac{E}{k_F} d\right)}{\cos\left(\frac{E}{k_F} d - \theta\right)}. \quad (5.31)$$

Comparing above equation with Eq. (5.28):

$$\begin{aligned} e^{-2pw} &= \frac{\cos^2\left(\frac{E}{k_F} d - \theta\right)}{\cos^2\left(\frac{E}{k_F} d\right)}, \\ e^{-2pw} &= \left(\frac{E}{|\Delta|}\right)^2 + \frac{2E}{|\Delta|} \sqrt{1 - \left(\frac{E}{|\Delta|}\right)^2} \tan\left(\frac{E}{k_F} d\right) \\ &+ \left(1 - \left(\frac{E}{|\Delta|}\right)^2\right) \tan^2\left(\frac{E}{k_F} d\right). \end{aligned} \quad (5.32)$$

For low energies, where  $E/\Delta \ll 1$ , above equation can be approximated to:

$$\frac{E}{|\Delta|} \approx e^{-\frac{|\Delta|w}{k_F}} \frac{1}{\frac{|\Delta|d}{k_F} + 1} = e^{-\frac{w}{2\xi}} \frac{1}{\frac{d}{2\xi} + 1}. \quad (5.33)$$

Above equation shows that the tunnelling events contribute to Eq. (5.13) with an exponential factor which is non-negligible for small ferrons. As it is shown in Fig. 5.4, a small ferron is accompanied with a lower pairing strength inside the ferron. Hence, Eq. (5.33) can be modified for the case  $|\Delta_{\text{in}}| \neq |\Delta_{\text{out}}|$  as:

$$\frac{E}{|\Delta|} \approx e^{-\frac{|\Delta_{\text{in}}|^2 w}{|\Delta_{\text{out}}| k_F}} \frac{1}{\frac{|\Delta_{\text{out}}| d}{k_F} + 1}, \quad (5.34)$$

where  $\Delta_{\text{in}}$  is the magnitude of the pairing field inside the nodal circle and  $\Delta_{\text{out}}$  is the magnitude of the pairing field in the bulk of the system. The effect of above correction term is visible on the lower subfigure of Fig. 5.6. It can be seen that the correction term is effective for the case of small ferron. Thus, we can conclude that the Andreev

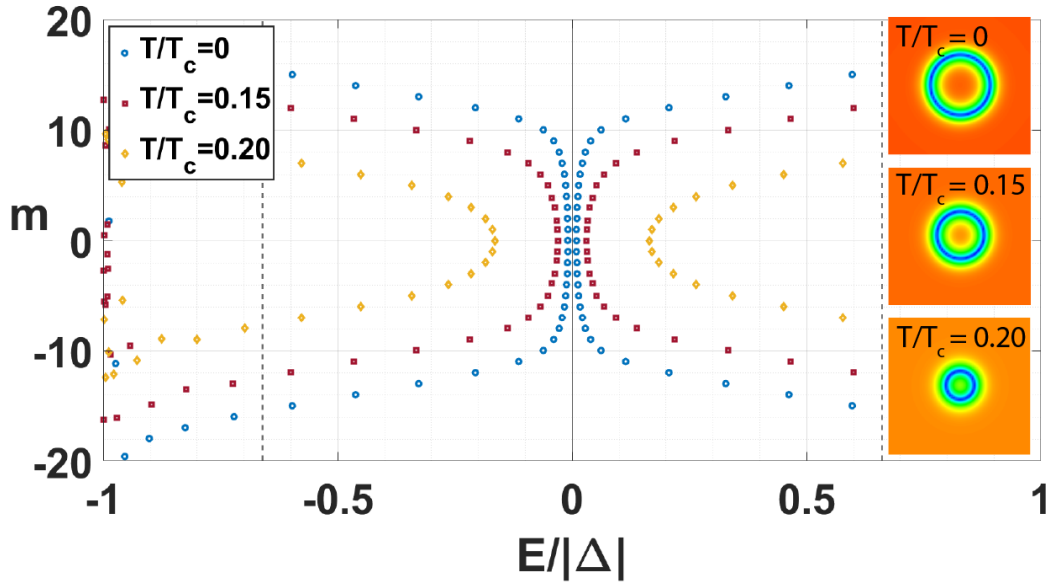


FIGURE 5.8: The effect of the finite temperature in 2D static calculations. As the temperature increases, the ferron gets smaller. Eventually, the nodal structure is destroyed. Insets show the structure of the pairing field with a color code same as Fig. 5.3. The spin-imbalance is  $\delta N = 31$ .

approximation is a valid analytic tool to examine the states inside the ferron. It gives good agreement with the numerical results obtained by BdG equations, not only qualitatively but also quantitatively.

## 5.4 Ferron at finite temperature

As shown in Eq. (2.55), the finite temperature is only included in the calculation of densities for numerical convenience; to smoothen the particle distribution. So far, the value of the finite temperature has been  $T = 10^{-5}T_c$ ; therefore, it was negligible. The value of the critical temperature,  $T_c$ , has been calculated using the well-known BCS result,  $|\Delta(T = 0)|/T_c \approx 1.76$  (Eq. (2.51)). To check the effect of finite temperature on ferron, a series of calculations with different temperatures has been performed. In particular, initially, a ferron with a given size at  $T = 10^{-5}T_c$  has been generated by minimizing the expression in Eq. (5.15). In the following, the temperature is increased by  $0.01T_c$ , and the energy is minimized again. This procedure repeated until the ferron is destroyed by thermal excitations.

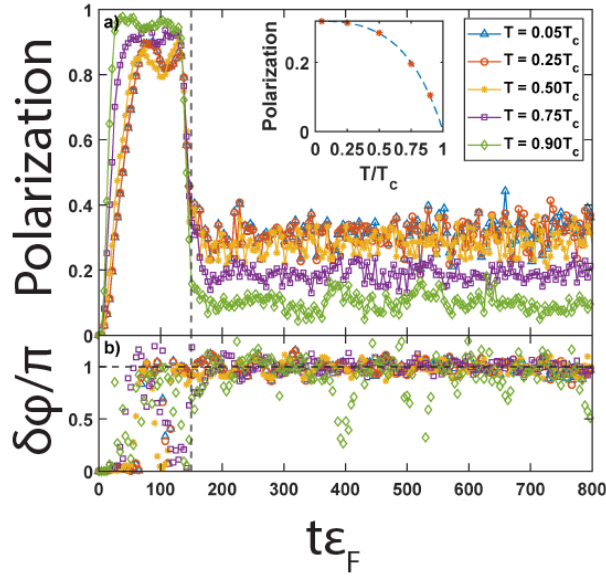


FIGURE 5.9: The 3D dynamic creation of ferron under finite temperature. Panel a) shows the time evolution of local polarization in the center of the object. Panel b) shows the pairing phase difference. The box size is  $L \approx 41$ . The amplitude of the potential was fixed at  $A_0 = 2\varepsilon_F$ . The width of the spin polarizing potential is  $\sigma = 4.71\zeta$ . The vertical dashed line shows the time where the external potential is turned off. The horizontal dashed line is a guide to the eye pointing to the value of  $\delta\varphi = \pi$ . Inset shows the time-averaged polarization in the center of ferron for various temperatures. The dashed blue line is a guide to the eye.

Fig. 5.8 shows that as the temperature increases, the size of the ferron slightly shrinks. This is due to the pairing field's response to the finite temperature (see Eq. (2.43)). As the ferron's size shrinks, it can be seen that the unpaired particles occupying relatively high angular momentum states are expelled since those states do not exist anymore. For high temperatures such as  $T/T_c = 0.20$ , the Andreev states move away from the  $E = 0$  line as a result of tunneling through a narrow ferron interior. When the temperature has reached a particular value, such a small nodal circle becomes unstable and destroyed. Therefore, larger ferrons may endure higher temperatures. For example, in the case of a larger ferron, where  $\delta N = 31$ , the nodal circle is destroyed at  $T/T_c \approx 0.21$ , while in the case of a smaller ferron, where  $\delta N = 21$ , the ferron is no more at  $T/T_c \approx 0.16$ .

It is also possible to dynamically create a ferron at finite temperature. The procedure is essentially the same as in the previous chapter, i.e., using the time-dependent

spin-selective potential. The results obtained within the ASLDA framework are presented in Fig. 5.9. It can be seen that the time-dependent calculations provide stable ferrons up to temperatures near the critical temperature. The time-dependent calculations involve applying an external potential that drives the system further from equilibrium since it excites phonon modes interacting with the droplet. Increasing the temperature in the system to values that are compatible with  $T_c$  drives the system out of equilibrium. ASLDA framework does not involve few-body scattering processes that can efficiently equilibrate the system back to thermal equilibrium. Therefore, the results presented in Fig. 5.9 are valid only for a short time after the external potential is turned off. For a long time evolution, the current ASLDA framework is insufficient to make conclusions.

## Chapter 6

# Dynamic properties of the ferron

### 6.1 The critical velocity of the ferron

As shown in Chapter 4, it is possible to dynamically create a moving ferron by dragging the external potential as in Eq. (4.8). According to the formula, the external potential moves with the velocity,  $v_{\text{drag}}$ . After the external potential is turned off, the resulting ferron moves with the velocity  $v_{\text{final}}$ , which is lower than  $v_{\text{drag}}$ . By tracking the center of the polarized sphere, it is possible to draw the trajectory of the ferron as a function of time. Fig. 6.1 (upper subfigure) shows the extraction of  $v_{\text{drag}}$  and  $v_{\text{final}}$ .

As the potential is dragged faster, the resulting velocity increases with it. It might seem kind of obvious at first: Fig. 6.1 (lower subfigure) shows that for relatively low velocities, the relation between  $v_{\text{drag}}$  and  $v_{\text{final}}$  is linear. However, it can be seen that as  $v_{\text{drag}}$  increases,  $v_{\text{final}}$  eventually reaches a critical value beyond which ferron can not be accelerated further. If  $v_{\text{drag}}$  is increased even more, it is observed that the ferron is destroyed during its movement. There are two effects responsible for this: When the final velocity gets closer to the critical value, the ferron undergoes deformation and finally ceases to exist. Additionally, during the acceleration of the ferron, the external potential excites phonons in the system. These phonons scatter inside the simulation box and interact with the ferron. While for low dragging velocities, ferron is stable against these perturbations, for high velocities, the strength of the perturbation increases with the number of excited phonons. Eventually, the ferron loses its stability. This effect hastens the destruction of the ferron.

Fig. 6.1 also shows that a larger ferron admits higher critical velocity (see the caption). In order to study the critical velocity in detail, we turn to 2D static calculations similar to the previous chapter. In static calculations, a uniform superflow with the wave-vector  $\mathbf{q}$  can be imposed to the system by setting the pairing field as:

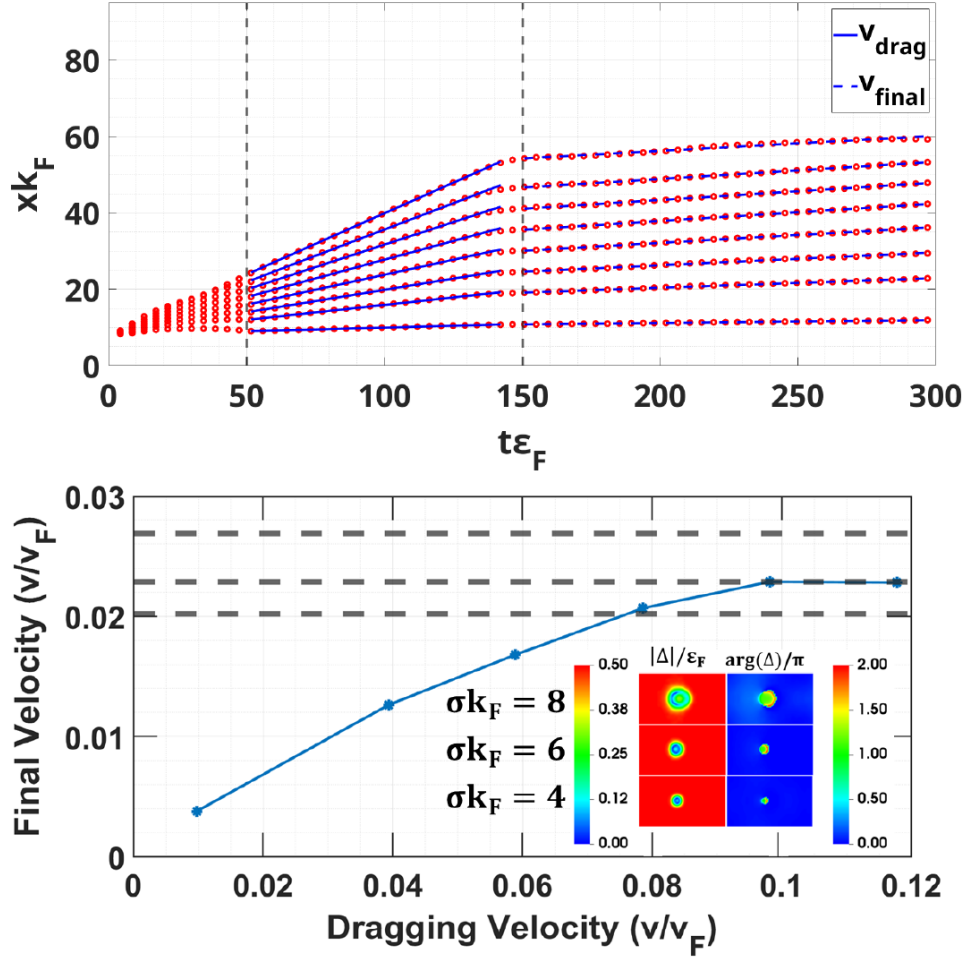


FIGURE 6.1: **Upper subfigure:** The position of the moving ferron inside a box corresponding to lattice size  $68 \times 40 \times 40$  which corresponds to  $53\zeta \times 31\zeta \times 31\zeta$ . The width of the polarizing potential is  $\sigma k_F = 6$  and its amplitude is  $A_0 = 2\varepsilon_F$ . The potential is switched on at  $t\varepsilon_F = 50$  and completely removed at  $t\varepsilon_F = 150$ . Different data sets correspond to different dragging velocities. **Lower subfigure:** Velocity of the ferron in the final state as a function of the dragging velocity. The time-dependent spin-selective potential is dragged along the  $x$ -axis during its application. The horizontal dashed lines shows the "plateau" of the final velocity for various sizes of ferrons corresponding to:  $\sigma k_F = 8$ ,  $\sigma k_F = 6$ ,  $\sigma k_F = 4$  from top to bottom, where  $\sigma$  is the width of the Gaussian potential. Inset shows the absolute value of the pairing field in the left column, while in the right column, the phase of the pairing field is shown. The images are taken after the external potential is turned off while the ferron is moving. All three configurations correspond to  $v_{\text{drag}}/v_F = 0.06$ . The figure is taken from Ref. [89].

$$\Delta(\mathbf{r}) \rightarrow \Delta(\mathbf{r})e^{2i\mathbf{q}\cdot\mathbf{r}} = g_{\text{eff}} \sum_n v_{n,\uparrow}^*(\mathbf{r})u_{n,\downarrow}(\mathbf{r}). \quad (6.1)$$

Therefore the BdG Hamiltonian with the presence of superflow is expressed as:

$$\begin{pmatrix} -\frac{\nabla^2}{2} - \mu_{\uparrow\downarrow} & \pm\Delta(\mathbf{r})e^{2i\mathbf{q}\cdot\mathbf{r}} \\ \pm\Delta(\mathbf{r})e^{-2i\mathbf{q}\cdot\mathbf{r}} & \frac{\nabla^2}{2} + \mu_{\uparrow\downarrow} \end{pmatrix} \begin{pmatrix} u_{n,\uparrow\downarrow}(\mathbf{r}) \\ v_{n,\uparrow\downarrow}(\mathbf{r}) \end{pmatrix} = E_n \begin{pmatrix} u_{n,\uparrow\downarrow}(\mathbf{r}) \\ v_{n,\uparrow\downarrow}(\mathbf{r}) \end{pmatrix}. \quad (6.2)$$

It is possible to change the reference frame using the following transformation:

$$\begin{aligned} u_{n,\uparrow\downarrow}(\mathbf{r}) &= \tilde{u}_{n,\uparrow\downarrow}(\mathbf{r})e^{i\mathbf{q}\cdot\mathbf{r}}, \\ v_{n,\uparrow\downarrow}(\mathbf{r}) &= \tilde{v}_{n,\uparrow\downarrow}(\mathbf{r})e^{-i\mathbf{q}\cdot\mathbf{r}}. \end{aligned} \quad (6.3)$$

Eq. (6.2) can be written in terms of new coherence factors  $\tilde{u}$  and  $\tilde{v}$ :

$$\begin{pmatrix} -\frac{(\nabla+i\mathbf{q})^2}{2} - \mu_{\uparrow\downarrow} & \pm\Delta(\mathbf{r}) \\ \pm\Delta(\mathbf{r}) & \frac{(\nabla+i\mathbf{q})^2}{2} + \mu_{\uparrow\downarrow} \end{pmatrix} \begin{pmatrix} \tilde{u}_{n,\uparrow\downarrow}(\mathbf{r}) \\ \tilde{v}_{n,\uparrow\downarrow}(\mathbf{r}) \end{pmatrix} = E_n \begin{pmatrix} \tilde{u}_{n,\uparrow\downarrow}(\mathbf{r}) \\ \tilde{v}_{n,\uparrow\downarrow}(\mathbf{r}) \end{pmatrix}. \quad (6.4)$$

In the presence of both superflow and the ferron, Eq. (6.2) describes a standing ferron in an environment of superflow. On the other hand, the pairing field does not oscillate in Eq. (6.4); therefore, there is no superflow. But, the single-particle part involves a velocity term which corresponds to a ferron moving with a velocity  $\mathbf{q}$  over a standing superfluid background.

The particle currents are defined as:

$$\mathbf{j}_{\uparrow\downarrow}(\mathbf{r}) = \frac{1}{2i} \sum_n \left[ v_{n,\uparrow\downarrow}(\mathbf{r}) \nabla v_{n,\uparrow\downarrow}^*(\mathbf{r}) - v_{n,\uparrow\downarrow}^*(\mathbf{r}) \nabla v_{n,\uparrow\downarrow}(\mathbf{r}) \right], \quad (6.5)$$

and the difference between currents corresponding to wavefunctions  $\{u, v\}$  and  $\{\tilde{u}, \tilde{v}\}$ :

$$\mathbf{j}_{\uparrow\downarrow}(\mathbf{r}) - \tilde{\mathbf{j}}_{\uparrow\downarrow}(\mathbf{r}) = \mathbf{q}\rho_{\uparrow\downarrow}(\mathbf{r}), \quad (6.6)$$

where  $\rho_{\uparrow\downarrow}(\mathbf{r}) = \sum_n |v_{n,\uparrow\downarrow}(\mathbf{r})|^2$  is the particle density. Eq. (6.6) shows that two reference frames move with respect to each other with the velocity  $\mathbf{q}$ . Therefore, it is possible to create a moving ferron solution by setting a superflow in the system.

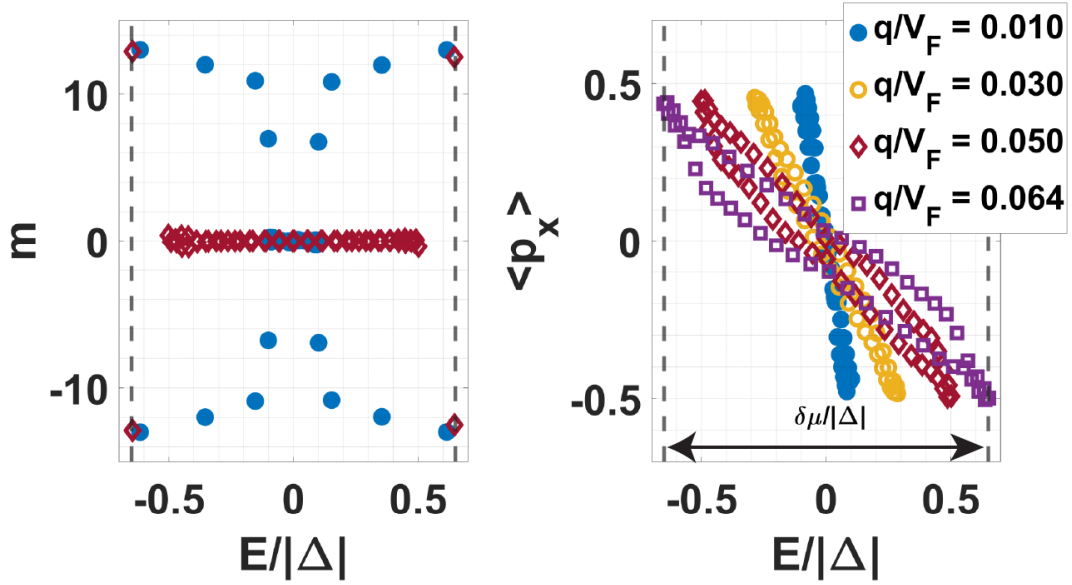


FIGURE 6.2: Structure of the spectrum of Andreev states exposed to different strengths of superflow. **Left subfigure:** Magnetic quantum numbers  $m$  corresponding to Andreev states are shown for two velocities of the superflow:  $q/v_F = 0.01$  (filled circles) and  $q/v_F = 0.05$  (empty diamonds), where  $v_F$  denotes Fermi velocity. **Right subfigure:** The expectation value of the momentum operator component, parallel to the direction of the superflow is shown for Andreev states. The quasiparticle energies have been shifted by  $\frac{1}{2}\delta\mu$  and therefore the plots on both subfigures possess symmetry with respect to  $E = 0$ . The shifted energy values corresponding to  $\pm\frac{1}{2}\delta\mu$  have been denoted by vertical dashed lines. The spin imbalance corresponds to  $\delta N = 31$  ( $R \approx 6.2\zeta$ ) and the strength of the pairing field  $|\Delta|/\varepsilon_F = 0.44$ . The figure is taken from Ref. [89].

The phase difference in the pairing fields between the bulk and the ferron interior is altered in the presence of superflow. It does not have the fixed value  $\delta\varphi = \pi$  as in the standing case. In the case of the moving ferron, the phase difference between the ferron interior and the bulk depends on the orientation of the particle trajectory and the direction of the superflow:  $\delta\varphi(\mathbf{r}) = \pi \pm 2\mathbf{q} \cdot \mathbf{r}$ . Therefore, two extremum values for the phase difference are:  $\delta\varphi_{\pm} = \pi \pm 2qd$ . Solving the Andreev equation (Eq. (5.1)) for this two cases under the low-energy assumption ( $E \ll |\Delta|$ ) gives:

$$\begin{aligned} E_+ &= \frac{\delta\mu}{2} \pm \frac{qk_F}{\frac{\xi}{d} + \frac{1}{4}}, \\ E_- &= -\frac{\delta\mu}{2} \pm \frac{qk_F}{\frac{\xi}{d} + \frac{1}{4}}. \end{aligned} \quad (6.7)$$

The above equations show that the energies  $E_{\pm}$  undergoes an additional split which scales the velocity of the superflow. The Andreev states forming the ferron obtain a non-zero expectation value of the linear momentum operator,  $\langle p_x \rangle$  as a result of the superflow. Fig. 6.2 shows that the states with low angular momentum are affected first. As the velocity increases, the states with higher angular momentum start to obtain a non-zero  $\langle p_x \rangle$  and contribute to the splitting in Eq. (6.7). Eventually, the width of the split reaches  $\delta\mu$ , meaning that the lowest energy Andreev state has zero energy with a non-zero  $\langle p_x \rangle$ . This leads to the instability and decay of the ferron. Fig. 6.2 (right subfigure) shows the split of the states with non-zero  $\langle p_x \rangle$ . Additionally, Fig. 6.3 shows that dependence of the slope of the split,  $s = \left(\frac{\xi}{d} + \frac{1}{4}\right)^{-1}$  to the size of the ferron is negligible. Therefore, the critical velocity,  $v_{\text{crit}}$ , is dictated by the maximum width of the split in Eq. (6.7) which is  $\delta\mu$ . In the previous chapter, it has been shown that there is a linear relationship between the size of the ferron and the spin-imbalance. A larger spin-imbalance means a larger difference in chemical potentials. So, the value of the critical velocity would be higher for a larger ferron in agreement with Fig. 6.1.

Another parameter that affects the critical velocity is the magnitude of the pairing field. For a given size of ferron, a lower pairing strength means a larger coherence length, which brings the tunneling effect discussed in the previous chapter. As shown in Fig. 5.6, the tunneling through the ferron interior removes the degeneracy at  $E = 0$ , hence creates a shift in the spectrum of states. Because of this shift, the split caused by finite  $q$  is enhanced. For a weakly paired system, the split width reaches  $\delta\mu$  for smaller values of  $q$  compared to a system with stronger pairing. Fig. 6.4 addresses the

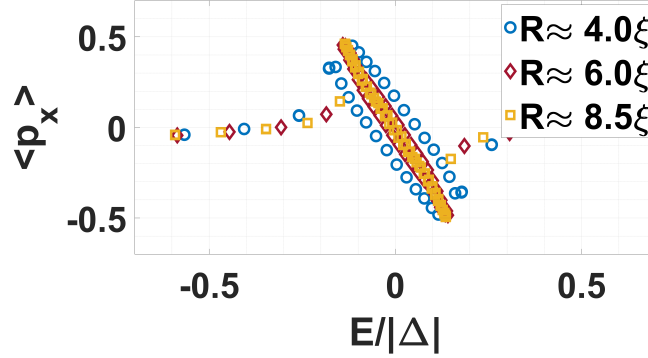


FIGURE 6.3: The expectation value of the momentum operator for different sizes of the ferron. All three sizes are subjected to the superflow  $q = 0.03v_F$ . The figure is taken from [89].

dependence of critical velocity both on the size of the ferron and the pairing strength. As it can be seen, a large ferron in a strong pairing regime admits the highest critical velocity. The deviations are attributed to the deformation of the ferron for velocities close to the critical velocity (see inset of Fig. 6.4).

### The ferron in the vicinity of vortex

The study of the critical velocity of ferron answers the possibility of a vortex–ferron coexistence. The time–dependent 3D simulations with the presence of a vortex are conducted at the unitary limit with the lattice size of  $80 \times 80 \times 32$ , which corresponds to  $62\tilde{\xi} \times 62\tilde{\xi} \times 25\tilde{\xi}$  with  $k_F \approx 1$ . A straight vortex line along  $z$ –direction is obtained by imposing on the static solution the following structure of the pairing field:  $\Delta(x, y) = |\Delta(x, y)|e^{i \tan^{-1}(y/x)}$ . Next, the ferron is generated dynamically by applying the spin selective potential (Eq. (4.8)), with  $v_{\text{drag}} = 0$  and  $x_0$  controls distance of the ferron from the vortex core. Since the currents generated by a vortex decrease linearly further from its center [59], the ferron should be placed carefully. A closer position of the ferron to a vortex brings the destruction of the ferron. Fig. 6.5 shows a dynamically generated ferron of radius  $rk_F = 6$  in the distance  $dk_F = 24$  from the core. At the point where the ferron is closest to the vortex, the induced velocity  $v = \frac{\hbar}{2mr} \approx 0.028v_F$  is higher than the critical velocity for this case  $v_{\text{crit}} \approx 0.024v_F$  (see Fig. 6.1). Consequently, the snapshots reveal stages of ferron decay. Since the critical velocity increases with the ferron size at first glance, one may attempt to increase the size of the ferron instead of moving it away. However, the currents generated by the vortex are not uniform in the

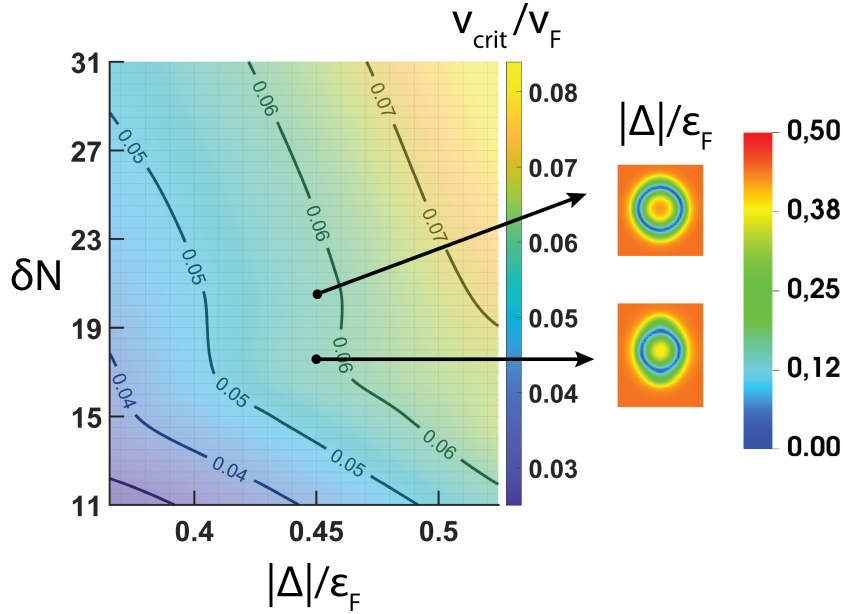


FIGURE 6.4: The ferron critical velocity as a function of the magnitude of the pairing field  $|\Delta|/\epsilon_F$  and the spin imbalance  $\delta N$ . Inset shows an example of two different sizes of ferron having the same critical velocity where the smaller ferron is deformed. The figure is taken from Ref. [89].

radial direction. Therefore, for a larger ferron, the effect caused by the non-uniformity of the superflow becomes more crucial.

## 6.2 Effective mass of the ferron

Examination of the ferron under superflow provokes the study of its inertia. The effective mass of the ferron helps quantify the force that needs to be acted on to accelerate or stop it. Therefore, it is a necessary step to create a model involving many ferrons.

In Eq. (6.4) a transformation from the standing reference frame to a frame moving with the superflow velocity  $q$  is defined. According to this moving reference frame, in the case of a uniform system, where there is no impurity, such as the ferron, the particle current would be zero. However, with the presence of the standing impurity, the currents are generated as superflow's response to the mass of the impurity:

$$M_{\text{eff}} = \lim_{q \rightarrow 0} \mathcal{R}(\mathbf{q}) = \lim_{q \rightarrow 0} \frac{|\int d^3r (\mathbf{j}_\uparrow + \mathbf{j}_\downarrow)|}{|\mathbf{q}|}. \quad (6.8)$$

The effective mass is composed of two terms:

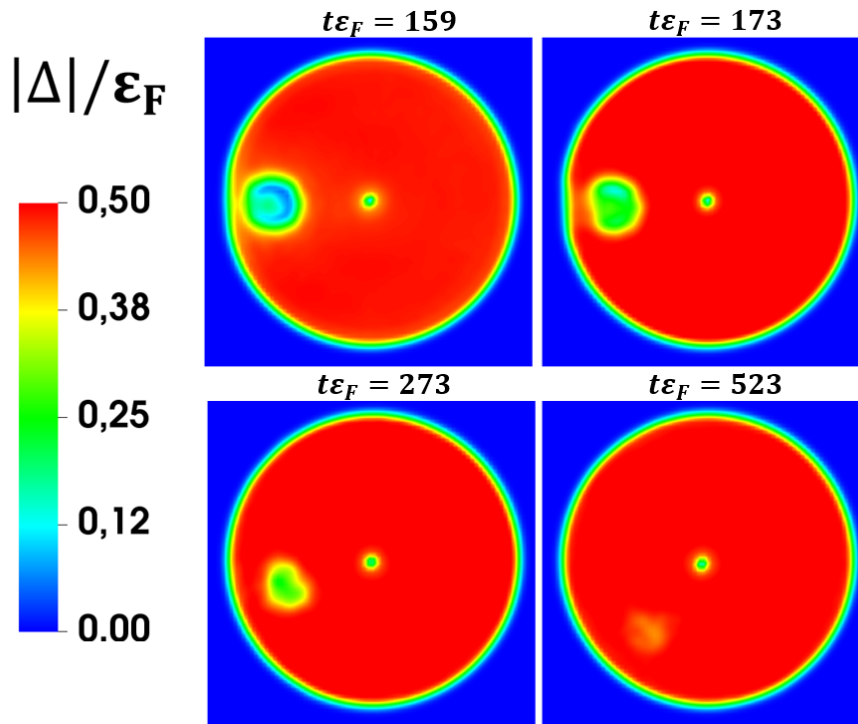


FIGURE 6.5: Snapshots showing the attempt to create a stable ferron solution in the presence of the vortex. The time-dependent potential to generate the ferron is turned off at  $t\epsilon_F = 150$ . The vortex, with the core located in the center, creates currents rotating counter-clockwise. It is visible that ferron is destroyed because of these currents. The polarization inside the ferron is pushed to the boundary of the system. The figure is taken from Ref. [89].

$$M_{\text{eff}} = M_{\text{pol}} + \delta M. \quad (6.9)$$

Here, the term  $M_{\text{pol}}$  represents the contribution coming from the unpaired particles constituting the ferron,  $M_{\text{pol}} = \delta N$ . By recalling the results in the previous chapter (Eq. (5.17)), one may conclude that the contribution coming from the spin-imbalanced particles to the effective mass scales with the radius of the ferron,  $M_{\text{pol}} \propto R$  in 2D, and  $M_{\text{pol}} \propto R^2$  in 3D.

The term  $\delta M$  represents the modification of the superfluid environment due to the presence of the impurity. In order to study this term, we turn to irrotational hydrodynamics:

$$\nabla \times \mathbf{v}_s = 0, \quad (6.10)$$

where  $\mathbf{v}_s$  is the average velocity of the superflow. Since the rotation of a gradient is zero,  $\nabla \times (\nabla \cdot \Phi) = 0$ , the velocity vector can be expressed as the following scalar potential:

$$\mathbf{v}_s = \nabla \Phi. \quad (6.11)$$

The general continuity equation which enforces the particle conservation is:

$$\frac{\partial n_s}{\partial t} + \nabla \cdot \mathbf{J}_s = 0, \quad (6.12)$$

where  $n_s$  is the condensate particle density and  $\mathbf{J}_s = n_s \mathbf{v}_s$  is defined as the supercurrent. Since, the density does not change with time,  $\frac{\partial n_s}{\partial t} = 0$ , Eq. (6.12) yields to:

$$\nabla \cdot \mathbf{v}_s = 0. \quad (6.13)$$

Combining above equation with Eq. (6.11) gives the Laplace equation for irrotational flow:

$$\nabla^2 \Phi = 0. \quad (6.14)$$

In the case of a circular impurity with a radius  $R$  immersed in a superfluid environment, the flow is divided into two parts:

$$\Phi(\mathbf{r}) = \begin{cases} \Phi_{\text{in}}(\mathbf{r}), & r < R, \\ \Phi_{\text{out}}(\mathbf{r}), & R < r, \end{cases} \quad (6.15)$$

where

$$\lim_{r \rightarrow \infty} \Phi_{\text{out}}(\mathbf{r}) = 0. \quad (6.16)$$

Therefore, for  $r < R$  we look for solutions in 2D polar coordinates, in the form of  $\Phi_{\text{in}}(\mathbf{r}) = Ar \cos \theta$ , and for  $R < r$  we look for solutions in the form of  $\Phi_{\text{out}}(\mathbf{r}) = B \cos \theta / r$ , with the following boundary conditions:

$$\begin{aligned} \Phi_{\text{in}}(R) &= \Phi_{\text{out}}(R), \\ (n_{\text{in}} - n_{\text{out}}) \mathbf{v} \cdot \mathbf{n} &= n_{\text{in}} \frac{\partial \Phi}{\partial r} \Big|_{r=R} - n_{\text{out}} \frac{\partial \Phi}{\partial r} \Big|_{r=R}, \end{aligned} \quad (6.17)$$

where  $\mathbf{n}$  is the unit vector normal to the boundary. Using the boundary conditions, the solutions of Eq. (6.14) are:

$$\Phi_{\text{in}}(\mathbf{r}) = \left( \frac{n_{\text{in}} - n_{\text{out}}}{n_{\text{in}} + n_{\text{out}}} \right) \mathbf{v} \cdot \mathbf{r}, \quad (6.18)$$

$$\Phi_{\text{out}}(\mathbf{r}) = \left( \frac{n_{\text{in}} - n_{\text{out}}}{n_{\text{in}} + n_{\text{out}}} \right) \frac{R^2}{r^2} \mathbf{v} \cdot \mathbf{r}. \quad (6.19)$$

Therefore, the energy stored in the superflow is:

$$\begin{aligned} E &= \frac{1}{2} \left[ \int_{r < R} n_{\text{in}} (\nabla \Phi_{\text{in}}(\mathbf{r}))^2 d^2 \mathbf{r} + \int_{r > R} n_{\text{out}} (\nabla \Phi_{\text{out}}(\mathbf{r}))^2 d^2 \mathbf{r} \right], \\ E &= \frac{1}{2} \pi R^2 \frac{(n_{\text{in}} - n_{\text{out}})^2}{n_{\text{in}} + n_{\text{out}}} v^2. \end{aligned} \quad (6.20)$$

Above equation describes the energy caused by the modification of the superfluid background. Therefore, the contribution to the effective mass coming from this modification is:

$$\delta M = \pi R^2 \frac{(n_{\text{in}} - n_{\text{out}})^2}{n_{\text{in}} + n_{\text{out}}}. \quad (6.21)$$

It can be seen that the above term scales with the area of the impurity and it is equal to zero when  $n_{\text{in}} = n_{\text{out}}$ . As the ferron's size gets larger, ( $R \gg \xi$ ), the densities inside and outside of the impurity becomes similar ( $|n_{\text{in}} - n_{\text{out}}| \rightarrow 0$ ). This means, in the case of a large ferron, the modification of the superfluid background is suppressed and  $M_{\text{pol}}$  term dominates the  $\delta M$  term:  $M_{\text{eff}} \approx M_{\text{pol}}$ . However, in the case of a small

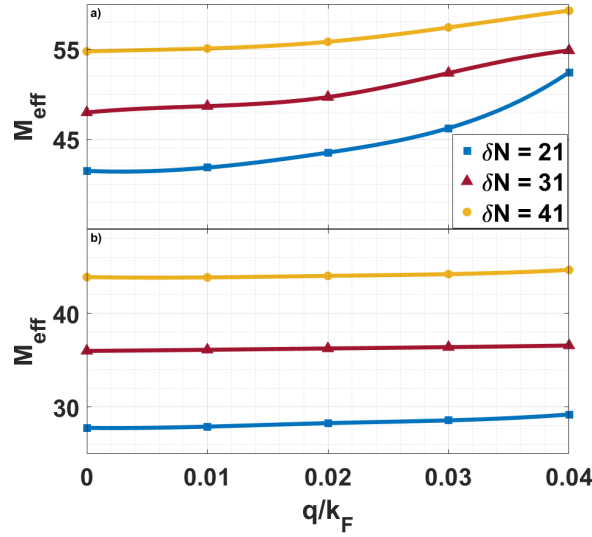


FIGURE 6.6: The response function in Eq. (6.8) as a function of the superflow velocity  $q$ . Symbols correspond to numerical calculations. Lines are obtained as a result of interpolation. The value of effective mass is extracted in the limit of  $q \rightarrow 0$  and denoted by symbols. The results for two values of the pairing field are shown:  $\Delta/\varepsilon_F = 0.365$  (panel a) and for  $\Delta/\varepsilon_F = 0.552$  (panel b). The lattice size is  $(70k_F^{-1})^2$  where  $k_F \approx 1$ . The figure is taken from Ref. [89].

ferron, the modification term  $\delta M$  becomes important since it scales with the area of the impurity, whereas the  $M_{\text{pol}}$  term scales with the circumference. In 3D systems, these arguments stay valid. Only, this time the  $M_{\text{pol}}$  term scales with the surface instead of circumference and  $\delta M$  scales with the volume instead of the surface.

An additional effect would be the strength of the pairing field. For a given size of the ferron, the density difference  $|n_{\text{in}} - n_{\text{out}}|$  is larger for a ferron surrounded by a weaker pairing field. This is a result of the tunneling effect discussed previously; in the weak pairing regime, the tunneling effect is more pronounced. Therefore, for a large ferron in the strong pairing regime, the  $\delta M$  term may become negligible. However, for the same ferron, but generated in the weak pairing regime,  $\delta M$  becomes crucial in order to estimate its effective mass.

In order to study the effective mass quantitatively, the BdG Hamiltonian in Eq. (6.4) is solved numerically for various pairing strengths  $|\Delta|/\varepsilon_F$  ranging from 0.36 to 0.55. A series of superflow corresponding to the velocity of  $q/v_F = 0.01, 0.02, 0.03$  and  $0.04$  are introduced and the response function is obtained by using Eq. (6.8). Finally, the results corresponding to different  $q$  values are extrapolated to the  $q \rightarrow 0$  limit using cubic Hermite interpolation. In Fig. 6.6 two examples for different pairing strengths

are presented. As shown in the above section, a ferron in a system with weaker pairing strength has lower critical velocity. Consequently, in panel a) of Fig. 6.6 the response function shows a stronger dependence on  $q$  than in the strong pairing limit shown in panel b). This is due to the fact that in the former case, the critical velocity is lower, and the shape of ferron is affected already at relatively small  $q$  values. The calculations have been performed in a box with lattice size  $70k_F^{-1} \times 70k_F^{-1}$  where  $k_{F\uparrow\downarrow} \approx 1$ . The stability of the results are tested with respect to the size of the box by evaluating effective mass in a box with lattice size  $100^2$  and found an agreement with accuracy better than 1%.

Fig. 6.7 (left subfigure) shows the effective mass for different sizes of the ferron under different pairing regimes. It can be seen that the above argument on the modification of the superfluid environment in the case of a small ferron or weak pairing is proved to be important. For the case of a large ferron in the strong coupling regime the effective mass is almost equal to the spin-imbalance,  $M_{\text{eff}} \approx M_{\text{pol}}$ . However, the ferron becomes heavier towards the weak coupling regime.

Fig. 6.7 (right subfigure) shows the comparison of two energies obtained by utilizing the calculated  $E_f(q) = \frac{1}{2}M_{\text{eff}}q^2$  and the excitation energy of the system caused by the velocity field,  $E_{\text{ex}}(q) = E(q) - E(0)$ . The latter energy values are calculated by the integration of the BdG functional (see Eq. (2.59)). It can be seen that two energies  $E_f(q)$  and  $E_{\text{ex}}(q)$  are almost the same for low velocities. For high velocities, the ferron which is immersed in the weaker pairing regime gets close to its critical velocity therefore a discrepancy appears.

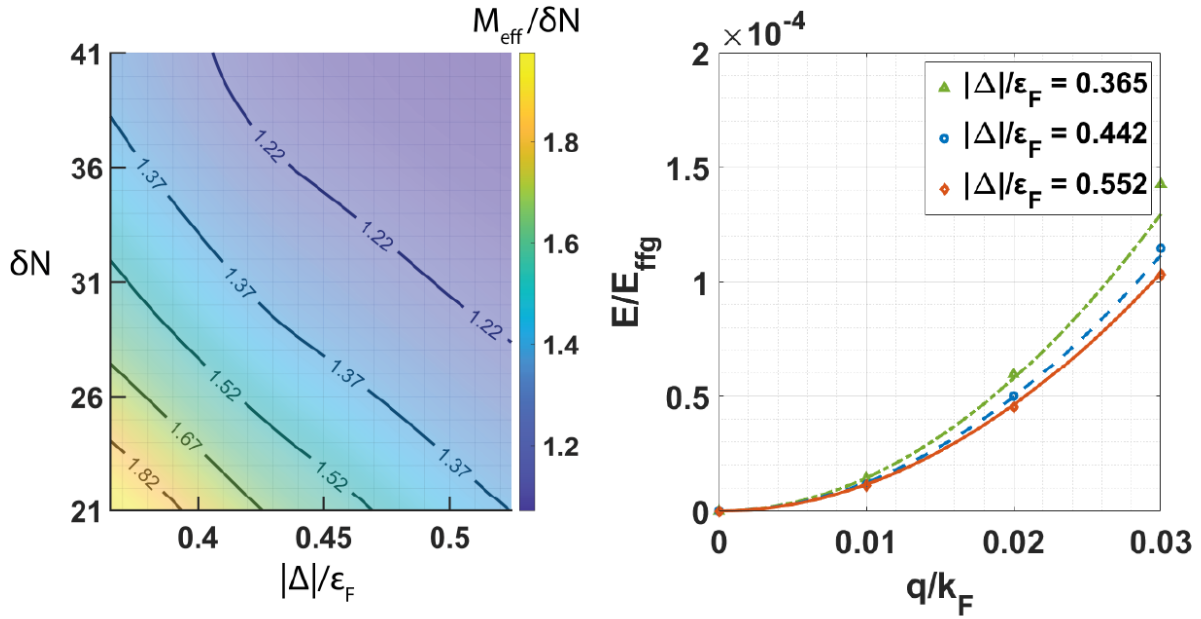


FIGURE 6.7: **Left subfigure:** The effective mass  $M_{\text{eff}}$  as a function of the magnitude of the pairing field  $|\Delta|/\epsilon_F$  and the spin imbalance  $\delta$ . In all cases the total number of particles in the simulation box is  $N = N_{\uparrow} + N_{\downarrow} = 770$  and the Fermi momentum  $k_F = \sqrt{2\epsilon_F} \approx 1$ . The values of  $\delta N = 21, 41$  correspond to the ferron radii  $R \approx 4.0\zeta$  and  $R \approx 8.3\zeta$ , respectively, where  $\zeta = \frac{1}{k_F} \frac{\epsilon_F}{|\Delta|}$ . **Right subfigure:** The excitation energy of the system  $E_{\text{ex}}(q)$  as a function of velocity  $q$  obtained in BdG calculations (lines). The kinetic energy of the ferron  $E_f(q)$  obtained using the extracted effective mass (points). Both energies are shown in units of non-interacting Fermi gas  $E_{\text{ffg}}$ . The spin-imbalance in the system is  $\delta N = 41$ . The lattice size is  $(70k_F^{-1})^2$  where  $k_F \approx 1$ . The figure is taken from Ref. [89].



## Chapter 7

# Conclusions and outlook

In this thesis, a novel type of meta-stable excitation mode in the ultracold Fermi gas is studied. The droplet can be created dynamically by locally breaking the Cooper pairs with a spin-selective external potential. The local mismatch in the Fermi levels causes spatial modulation in the pairing field and creates a nodal region where the pairing is effectively suppressed while changing its sign. This nodal circle contains the Andreev levels. The nodal region is stabilized by the unpaired majority particles and by the pairing field in both ends of the nodal region, acting as an effective potential barrier. It is shown that when the external potential is turned off, the structure is stable throughout the time interval that can be reliably observed within the numerical scheme.

The creation and stability of the ferron are studied as a function of the lattice size, size, strength, and adiabaticity of the external potential. It can be seen from the above results that as long as the pairing field locally changes its sign and the superfluid environment is unharmed, there is no mechanism for the ferron decay within the mean-field description.

It is demonstrated that in the case of an asymmetric external potential, the ferron slowly reshapes into a symmetric structure once the external potential is turned off. It is also possible to create concentric ferrons when the spin-polarization is large enough. However, this process could be rather violent and may create phonon excitations which in principle may affect the stability of the droplet. Different scenarios of ferron collisions show that these structures are robust to collisions. They merge if they are made of the same spin component and annihilate each other in the case of opposite spins.

To test the soundness of the results, different numerical frameworks and different coupling regimes are considered. It is shown that the ferron creation is not a trademark of a particular density functional. Although, in principle, it is possible to obtain the ferron as long as the pairing persists in the system, for a weak-coupling regime, the

external potential may destroy the superfluidity. Therefore, the unitary regime offers a more stable environment to study ferron.

The inner structure of the ferron is composed of Andreev bound states where the unpaired particles localized in sub-gap energies without being expelled from the superfluid. By inspection of these states, the size of the ferron can be related to the total number of particles it has. Moreover, the mechanism behind its critical velocity can be understood from the inspection of the Andreev bound states. Namely, as the ferron moves faster, more states obtain a non-zero linear momentum, eventually resulting in instability. The critical velocity depends on the chemical potential difference between the spin components and the strength of the background pairing field. The critical velocity is confirmed in time-dependent simulations. It is impossible to accelerate the ferron beyond a certain velocity. Moreover, the ferron is studied in the vicinity of a vortex core. Although technically it is possible to have a ferron and a vortex in the same system, they should be placed far away from each other. Otherwise, the superflow created by the vortex exceeds the critical velocity and destroys the ferron.

The effective mass of the ferron is studied to describe the motion of the ferron. The effective mass has two contributions. The main contribution is the object's size, but there turned out to be a correction coming from the modification of the surrounding superfluid environment, which is suppressed in the large ferron or a strong coupling limit. However, it becomes noticeable for small ferrons or weak coupling regimes where the tunneling across the ferron becomes effective.

The finite temperature studies show that there is a limit to the temperature in which the ferron may exist. As the temperature increases, the pairing field rearranges itself, resulting in a smaller nodal region and expulsion of some of the unpaired particles. At a certain temperature, the ferron reaches a size which the tunneling effects across the ferron interior causes its destruction. This temperature lies lower than the critical temperature for the appearance of the pairing field. However, it is showed that if the size of the ferron is large enough, it would be experimentally possible to create such an environment where it can be obtained.

The ferron can be considered as a Larkin–Ovchinnikov droplet because of the structure of the pairing field it is associated with. Additionally, because of the same reasoning, a moving ferron may correspond to a Fulde–Ferrel droplet. Since the FFLO phase is unconfirmed, the ferron may offer an easier experimental procedure and a strong implication of this much-anticipated phase. Hence, an important future focus would be studying realistic scenarios of ferron creation, paving the way for its realization.

Moreover, the fate of the ferron, after the supercurrents destroy it, is also left as an open question and may lead to other novel exotic configurations. Finally, scenarios that involve many ferrons and their dynamics can be studied based on the outcomes of this thesis.



# Bibliography

- (1) H. K. Onnes, *Commun. Phys. Lab. Univ. Leiden*, 1911, **12**, 120.
- (2) W. Meissner and R. Ochsenfeld, *Naturwissenschaften*, Nov. 1933, **21**, 787–788.
- (3) P. Kapitza, *Nature*, Jan. 1938, **141**, 74–74.
- (4) Bose, *Zeitschrift für Physik*, Dec. 1924, **26**, 178–181.
- (5) A. Einstein, in, Aug. 2006, vol. 23, pp. 245–257.
- (6) M. H. Anderson, J. R. Ensher, M. R. Matthews, C. E. Wieman and E. A. Cornell, *Science*, 1995, **269**, 198–201.
- (7) K. B. Davis, M. .-O. Mewes, M. R. Andrews, N. J. van Druten, D. S. Durfee, D. M. Kurn and W. Ketterle, *Phys. Rev. Lett.*, Nov. 1995, **75**, 3969–3973.
- (8) D. D. Osheroff, R. C. Richardson and D. M. Lee, *Phys. Rev. Lett.*, Apr. 1972, **28**, 885–888.
- (9) D. D. Osheroff, W. J. Gully, R. C. Richardson and D. M. Lee, *Phys. Rev. Lett.*, Oct. 1972, **29**, 920–923.
- (10) L. Landau, *Phys. Rev.*, Aug. 1941, **60**, 356–358.
- (11) J. Bardeen, L. N. Cooper and J. R. Schrieffer, *Phys. Rev.*, Dec. 1957, **108**, 1175–1204.
- (12) C. Chin, R. Grimm, P. Julienne and E. Tiesinga, *Reviews of Modern Physics*, Apr. 2010, **82**, 1225–1286.
- (13) D. M. Eagles, *Phys. Rev.*, Oct. 1969, **186**, 456–463.
- (14) A. J. Leggett, in *Lecture Notes in Physics*, Berlin Springer Verlag, ed. A. Pękaliski and J. A. Przystawa, 1980, vol. 115, p. 13.
- (15) P. Nozieres and S. Schmitt-Rink, *J. Low Temp. Phys.*, 1985, **59**, 195.
- (16) M. Randeria, *Nature Physics*, Aug. 2010, **6**, 561–562.
- (17) G. Bertsch, *Recent Progress in Many-Body Theories: Proceedings of the Tenth International Conference*, English, ed. R. Bishop, K. Gernoth, N. Walet and Y. Xian, World Scientific Publishing Co. Pte. Ltd, Singapore, 2000.

- 
- (18) S. Gandolfi, A. Gezerlis and J. Carlson, *Annual Review of Nuclear and Particle Science*, Oct. 2015, **65**, 303–328.
- (19) J. Carlson and S. Reddy, *Physical Review Letters*, Aug. 2005, **95**, DOI: 10.1103/physrevlett.95.060401.
- (20) J. Carlson, S.-Y. Chang, V. R. Pandharipande and K. E. Schmidt, *Phys. Rev. Lett.*, July 2003, **91**, 050401.
- (21) P. Magierski, G. Wlazłowski, A. Bulgac and J. E. Drut, *Phys. Rev. Lett.*, Nov. 2009, **103**, 210403.
- (22) B. S. Chandrasekhar, *Applied Physics Letters*, 1962, **1**, 7–8.
- (23) A. M. Clogston, *Phys. Rev. Lett.*, Sept. 1962, **9**, 266–267.
- (24) K. Gubbels and H. Stoof, *Physics Reports*, 2013, **525**, Imbalanced Fermi Gases at Unitarity, 255–313.
- (25) G. Sarma, *Journal of Physics and Chemistry of Solids*, 1963, **24**, 1029–1032.
- (26) I. Shovkovy and M. Huang, *Physics Letters B*, July 2003, **564**, 205–211.
- (27) S.-T. Wu and S. Yip, *Phys. Rev. A*, May 2003, **67**, 053603.
- (28) K. B. Gubbels, M. W. J. Romans and H. T. C. Stoof, *Phys. Rev. Lett.*, Nov. 2006, **97**, 210402.
- (29) W. V. Liu and F. Wilczek, *Physical Review Letters*, Jan. 2003, **90**, DOI: 10.1103/physrevlett.90.047002.
- (30) M. M. Parish, F. M. Marchetti, A. Lamacraft and B. D. Simons, *Physical Review Letters*, Apr. 2007, **98**, DOI: 10.1103/physrevlett.98.160402.
- (31) M. M. Forbes, E. Gubankova, W. V. Liu and F. Wilczek, *Physical Review Letters*, Jan. 2005, **94**, DOI: 10.1103/physrevlett.94.017001.
- (32) H. Hu, X.-J. Liu and P. D. Drummond, *Phys. Rev. Lett.*, Feb. 2007, **98**, 060406.
- (33) D. Inotani, S. Yasui, T. Mizushima and M. Nitta, *Phys. Rev. A*, May 2021, **103**, 053308.
- (34) P. Magierski, G. Wlazłowski, A. Makowski and K. Kobuszewski, *Spin-polarized vortices with reversed circulation*, 2020.
- (35) L. Radzihovsky, *Phys. Rev. A*, Aug. 2011, **84**, 023611.
- (36) A. Bulgac and M. M. Forbes, *Phys. Rev. Lett.*, Nov. 2008, **101**, 215301.

- 
- (37) P. Fulde and R. A. Ferrell, *Phys. Rev.*, Aug. 1964, **135**, A550–A563.
- (38) A. I. Larkin and Y. N. Ovchinnikov, *Zh. Eksperim. i Teor. Fiz.*, Sept. 1964, **47**.
- (39) J. J. Kinnunen, J. E. Baarsma, J.-P. Martikainen and P. Törmä, *Reports on Progress in Physics*, Feb. 2018, **81**, 046401.
- (40) A. I. Buzdin, *Rev. Mod. Phys.*, Sept. 2005, **77**, 935–976.
- (41) F. Chevy and C. Mora, *Reports on Progress in Physics*, Oct. 2010, **73**, 112401.
- (42) D. T. Son and M. A. Stephanov, *Phys. Rev. A*, July 2006, **74**, 013614.
- (43) A. Bulgac, M. M. Forbes and A. Schwenk, *Phys. Rev. Lett.*, July 2006, **97**, 020402.
- (44) C.-H. Pao, S.-T. Wu and S.-K. Yip, *Physical Review B*, Apr. 2006, **73**, DOI: 10.1103/physrevb.73.132506.
- (45) P. F. Bedaque, H. Caldas and G. Rupak, *Physical Review Letters*, Dec. 2003, **91**, DOI: 10.1103/physrevlett.91.247002.
- (46) P. Magierski, B. Tüzemen and G. Wlazłowski, *Physical Review A*, Sept. 2019, **100**, DOI: 10.1103/physreva.100.033613.
- (47) M. Barkman, A. Samoilenka, T. Winyard and E. Babaev, *Phys. Rev. Research*, Nov. 2020, **2**, 043282.
- (48) C. J. Pethick and H. Smith, *Bose–Einstein Condensation in Dilute Gases*, Cambridge University Press, 2nd edn., 2008.
- (49) P. D. Lett, W. D. Phillips, S. L. Rolston, C. E. Tanner, R. N. Watts and C. I. Westbrook, *J. Opt. Soc. Am. B*, Nov. 1989, **6**, 2084–2107.
- (50) B. DeMarco and D. S. Jin, *Science*, 1999, **285**, 1703–1706.
- (51) C. A. Regal, M. Greiner and D. S. Jin, *Phys. Rev. Lett.*, Jan. 2004, **92**, 040403.
- (52) C. Chin, M. Bartenstein, A. Altmeyer, S. Riedl, S. Jochim, J. H. Denschlag and R. Grimm, *Science*, 2004, **305**, 1128–1130.
- (53) M. W. Zwierlein, J. R. Abo-Shaer, A. Schirotzek, C. H. Schunck and W. Ketterle, *Nature*, June 2005, **435**, 1047–1051.
- (54) T. Köhler, K. Góral and P. S. Julienne, *Rev. Mod. Phys.*, Dec. 2006, **78**, 1311–1361.
- (55) H. Fröhlich, *Phys. Rev.*, Sept. 1950, **79**, 845–856.
- (56) L. N. Cooper, *Phys. Rev.*, Nov. 1956, **104**, 1189–1190.
- (57) P. G. de Gennes, *Superconductivity of Metals and Alloys*, Benjamin, 1966.

- 
- (58) J. F. Annett, *Superconductivity, superfluids and condensates*, Oxford Univ. Press, Oxford, 2004.
- (59) A. Leggett, *Quantum Liquids: Bose condensation and Cooper pairing in condensed-matter systems*, English (US), Oxford University Press, United Kingdom, Jan. 2008, vol. 9780198526438.
- (60) P. Ring and P. Schuck, *The Nuclear Many-Body Problems*, Jan. 1980, vol. 103.
- (61) D. Thouless, *Nuclear Physics*, 1960, **21**, 225–232.
- (62) M. Tinkham, *Introduction to Superconductivity: Second Edition (Dover Books on Physics) (Vol i)*, Dover Publications, 2nd edn., June 2004.
- (63) H. Ibach and H. Lüth, *Solid-State Physics*, June 2009, pp. 1–19.
- (64) I. Giaever and K. Megerle, *Phys. Rev.*, May 1961, **122**, 1101–1111.
- (65) P. Magierski, G. Wlazłowski and A. Bulgac, *Phys. Rev. Lett.*, Sept. 2011, **107**, 145304.
- (66) J. E. Drut, T. A. Lähde, G. Wlazłowski and P. Magierski, *Phys. Rev. A*, May 2012, **85**, 051601.
- (67) G. Wlazłowski, P. Magierski, A. Bulgac and K. J. Roche, *Phys. Rev. A*, July 2013, **88**, 013639.
- (68) A. Bulgac, M. N. Forbes and P. Magierski, in *The BCS–BEC Crossover and the Unitary Fermi Gas*, Springer Berlin Heidelberg, 2102.
- (69) P. Hohenberg and W. Kohn, *Phys. Rev.*, Nov. 1964, **136**, B864–B871.
- (70) W. Kohn and L. J. Sham, *Phys. Rev.*, Nov. 1965, **140**, A1133–A1138.
- (71) L. N. Oliveira, E. K. U. Gross and W. Kohn, *Phys. Rev. Lett.*, June 1988, **60**, 2430–2433.
- (72) O. .-.-J. Wacker, R. Kümmel and E. K. U. Gross, *Phys. Rev. Lett.*, Nov. 1994, **73**, 2915–2918.
- (73) S. Kurth, M. Marques, M. Lüders and E. K. U. Gross, *Phys. Rev. Lett.*, Sept. 1999, **83**, 2628–2631.
- (74) A. Bulgac and Y. Yu, *Phys. Rev. Lett.*, Jan. 2002, **88**, 042504.
- (75) A. Bulgac, *Physical Review C*, Aug. 2001, **65**, DOI: 10.1103/PhysRevC.65.051305.
- (76) Y. Yu and A. Bulgac, *Phys. Rev. Lett.*, June 2003, **90**, 222501.
- (77) A. Bulgac, *Physical Review A*, Oct. 2007, **76**, DOI: 10.1103/physreva.76.040502.

- 
- (78) A. Bulgac, *Annual Review of Nuclear and Particle Science*, Oct. 2013, **63**, 97–121.
- (79) G. Wlazłowski, K. Sekizawa, M. Marchwiany and P. Magierski, *Phys. Rev. Lett.*, June 2018, **120**, 253002.
- (80) P. Magierski, *Frontiers in Nuclear and Particle Physics: Volume 2*, June 2019, 57–71.
- (81) J. W. Rohlf, *Modern Physics from A to Z*, John Wiley and Sons, New York, 1994.
- (82) E. Runge and E. K. U. Gross, *Phys. Rev. Lett.*, Mar. 1984, **52**, 997–1000.
- (83) *W-SLDA Toolkit webpage*, <https://wslida.fizyka.pw.edu.pl>.
- (84) V. W.-z. Yu, J. Moussa, P. Kus, A. Marek, P. Messmer, M. Yoon, H. Lederer and V. Blum, *Computer Physics Communications*, 2021, **262**, 107808.
- (85) K. Halterman and O. T. Valls, *Phys. Rev. B*, Jan. 2004, **69**, 014517.
- (86) A. Bulgac, Y.-L. Luo, P. Magierski, K. J. Roche and Y. Yu, *Science*, 2011, **332**, 1288–1291.
- (87) A. Bulgac, M. M. Forbes, M. M. Kelley, K. J. Roche and G. Wlazłowski, *Phys. Rev. Lett.*, Jan. 2014, **112**, 025301.
- (88) B. Tüzemen, P. Kukliński, P. Magierski and G. Wlazłowski, *Acta Physica Polonica B*, 2020, **51**, 595.
- (89) P. Magierski, B. Tüzemen and G. Wlazłowski, *Phys. Rev. A*, Sept. 2021, **104**, 033304.